AFRL-VS-TR-1999-1522
E.R.P., No. 1220

The Midcourse Space Experiment Point Source Catalog Version 1.2 Explanatory Guide

M.P. Egan
S.D. Price
M.M. Moshir
M. Cohen
E. Tedesco
T.L. Murdock
A. Zweil
S. Burdick
N. Bonito
G.M. Gugliotti
J. Duszlak

17 June 1999

Approved for Public Release; Distribution Unlimited

AIR FORCE RESEARCH LABORATORY
Space Vehicles Directorate
29 Randolph Rd
AIR FORCE MATERIEL COMMAND
Hanscom AFB, MA 01731-3010

" This technical report has been reviewed and is approved for publication."

MICHAEL P. EGAN
Author

STEPHAN D. PRICE, Chief
Background Characterization Branch

DAVID A. HARDY, Chief
Battlespace Environment Division

REPORT DOCUMENTATION PAGE

Form Approved
OMB No. 0704-0188

1. AGENCY USE ONLY *(Leave blank)*

2. REPORT DATE
17 June 1999

3. REPORT TYPE AND DATES COVERED
Scientific, Interim

4. TITLE AND SUBTITLE
The Midcourse Space Experiment Point Source Catalog Version 1.2 Explanatory Guide

5. FUNDING NUMBERS
PR 1010
TA BS
WU 01

6. AUTHOR(S)
Egan, M.P., Price, S.D., Moshir, M.M.*, Cohen, M.#, Tedesco, E.*, Murdock, T.L.##, Zweil, A.##, Burdick, S.##, Bonito, N.***, Gugliotti, G.M.***, Duszlak, J.***

7. PERFORMING ORGANIZATION NAME(S) AND ADDRESS(ES)
Air Force Research Laboratory/VSBC
29 Randolph Rd
Hanscom AFB, MA 01731-3010

8. PERFORMING ORGANIZATION REPORT NUMBER
AFRL-VS-TR-1999-1522

9. SPONSORING/MONITORING AGENCY NAME(S) AND ADDRESS(ES)
Ballistic Missile Defense Organization

10. SPONSORING/MONITORING AGENCY REPORT NUMBER

11. SUPPLEMENTARY NOTES
*Infrared Processing and Analysis Center
#Vanguard Research, Inc., and University of California, Berkeley, CA
** Terrasystems, INc., ## Frontier Technologies, Inc., ***RADEX, Inc., (Continued)

12a. DISTRIBUTION / AVAILABILITY STATEMENT
Approved for Public Release; distribution unlimited.

12b. DISTRIBUTION CODE

13. ABSTRACT *(Maximum 200 words)*

This Explanatory Guide to the MSX Point Source Catalog briefly describes the instrumentation and the experiments, which emphasized the areas that IRAS did not survey, and the Galactic Plane. A detailed discussion of the calibration and data processing follows. This guide then describes the catalog contents and presents analyses of the the reliability of the quoted fluxes and positions, and the completeness and reliability of the catalog as a whole.

14. SUBJECT TERMS
Infrared astronomy Point sources

15. NUMBER OF PAGES

16. PRICE CODE

17. SECURITY CLASSIFICATION OF REPORT	18. SECURITY CLASSIFICATION OF THIS PAGE	19. SECURITY CLASSIFICATION OF ABSTRACT	20. LIMITATION OF ABSTRACT
UNCLASSIFIED	UNCLASSIFIED	UNCLASSIFIED	UNL

Contents

List of Figures

List of Tables

1 Introduction

The Midcourse Space Experiment (MSX) was a multi-discipline experiment sponsored by the Ballistic Missile Defense Organization. It was designed to characterize the phenomenologies pertinent to midcourse target detection, acquisition and track. There were eight Principal Investigator (PI) teams: three addressing different aspects of target detection and phenomenology; two addressing technology issues related to the conduct of a space-based infrared experiment; one team observing the earth and its atmosphere in the infrared and another observing it in the ultraviolet and visible; the eighth PI team was responsible for infrared and ultraviolet astronomy measurements. Mill *et al.* (1994) give an overview of the mission, its objectives, and the instruments on the satellite.

The principal objective of the MSX astronomy experiments was to complete the census of the mid-infrared sky. Experiments were designed to cover the regions either missed by the US/Netherlands/UK Infrared Astronomy Satellite (IRAS) and the Cosmic Background Explorer/Diffuse Infrared Background Experiment (COBE/DIRBE) or where the sensitivity of IRAS was degraded by confusion noise arising in regions of high source densities or structured extended emission. The zodiacal foreground was sampled from the pole to the plane and from the anti-solar direction to within 22° of the sun. Another experiment surveyed the areas missed by IRAS or covered by only a single IRAS HCON. All the areas labeled as confused in the IRAS data products were surveyed, including the entire Galactic plane.

The Midcourse Space Experiment Point Source Catalog Version 1.2 lists the sources detected in the MSX Infrared Galactic Plane Survey and the Survey of Areas Missed by IRAS (See Price *et al.*, 1998, for details on the MSX astronomy experiments). The source extraction software automatically extracts all point sources with signal-to-noise ratio >3 from the Celestial Background data. The MSX survey experiments use redundant scans of an area to increase completeness and reliability, in much the same way that the IRAS survey required multiple HCON confirmation of sources.

In this Explanatory Guide to the MSX Point Source Catalog, we briefly describe the instrumentation and the experiments, followed by a detailed discussion of the calibration and data processing. Finally, we describe the catalog contents and present analyses of the reliability of the quoted fluxes and positions, and the completeness and reliability of the catalog as a whole.

2 The SPIRIT III Instrument

The infrared instrument on MSX, designated SPIRIT III for historical regions, is a 35 cm clear aperture off-axis telescope with five line-scanned, infrared, focal plane arrays and an aperture shared interferometer. The effective aperture of the radiometer was reduced to about 33 cm by a Lyot stop that reduced the off-axis radiation from the Earth for the atmospheric measurements. The entire system was cooled by a single solid H_2 cryostat. The Si:As BiB arrays had eight columns of detectors, each consisting of 192 rows of 18.3″ square pixels. Half the columns in each array were offset from the other half by 0.5 pixel, providing Nyquist sampling in the cross scan direction. The sensor system parameters are presented in Table 1.

To reduce the telemetry rate, only half the columns were active as indicated in the table; at least one column was active on either side of the stagger. Band B was divided in half in cross-scan by two different filters centered on the 4.3 μm atmospheric CO_2 band. This blocked about 10% of the pixels under the filter mask, otherwise less than 3% of the focal plane detectors were non-responsive or rejected for various reasons.

The choice of filters was influenced by the infrared spectral character of the Earth's atmosphere. Bands B and D are centered on the 4.2 and 15 μm CO_2 atmospheric features, respectively; the others are window regions, at least in the upper atmosphere. Band A is the most sensitive and covers a spectral region not previously surveyed extensively. Band C is a narrower analog of the 12 μm filter used on other major space based infrared astronomy survey experiments, IRAS Band 1 and COBE/DIRBE Band 5. Band E is a good analog of the COBE/DIRBE Band 6, the latter commonly compared with the IRAS 25 μm band. The source function for the isophotal wavelength, bandwidth and the zero magnitude flux is the Kurucz model for α Lyr taken from Cohen et al. (1992). The detailed relative spectral response (RSR) for each band is given in Appendix A of this document.

The SPIRIT III instrument was extensively calibrated both on the ground and on-orbit. The ground calibration measured the entire throughput of the instrument by means of a specially constructed, cryogenically cooled, vacuum chamber to which the telescope was attached. The chamber used a variety of standard sources, all of which are directly traceable to National Institute for Standards and Technology (NIST) references. The 10% duty cycle of the SPIRIT III instrument and the wide range of environments and backgrounds to which the telescope was subjected meant that the operating conditions of the instrument were dynamic. The focal plane also warmed up as the hydrogen in the cryostat evaporated which resulted in increasing dark current and dark current noise with time. The ground calibration determined the relative variation with temperature of all significant parameters, such as response, linearity, dark current and flat fielding. The results of extensive on-orbit calibration experiments were used to adjust the initial response parameters and to reduce the photometric uncertainties. The on-orbit references included stellar standards as well as five reference spheres released at various times during the mission. The uncertainties quoted in Table 1 are on the absolute value of the photometry. These are conservative by astronomical standards which usually quote precision, or repeatability of the flux measurement. The MSX precision is 2-3% in all spectral bands.

The sensitivity range entries in Table 1 are estimates from the beginning and end of the mission. With a spring launch, almost all of the highest priority measurement objectives were obtained in the first half of the mission. This includes the Galactic plane survey of quadrants I and IV, which contain the highest source densities and the majority of extended, diffuse emission. The quoted accuracies for photometry are for the calibration constants used with the penultimate version of the processing software.

3 The MSX Celestial Background Surveys

The spatial resolution (18.3″) and high sensitivity (0.1 Jy at 8.3 μm) at a rapid scan rate (up to 0.125 sq. deg/sec) made SPIRIT III on MSX an ideal survey instrument. Figure 1 shows the areas covered by the various MSX experiments on an Aitoff equal area plot in Galactic coordinates. The nearly circular, off-center

Table 1: SPIRIT III Spectral Bands

Band	No active cols.	Isophotal $\lambda(\mu m)$	50% peak intensity	Isophotal BW (μm)	Zero mag flux (Jy)	Abs. Photom. Accuracy	Survey Sens. (Jy)	Effective FOV Ω_{EFOV} ($\times 10^{-9}$ sr)
A	8	8.28	6.8-10.8	3.36	58.49	5%	0.1 - 0.2	10.6
B_1	2	4.29	4.22-4.36	0.104	194.6	9%	10-30	14.0
B_2	2	4.35	4.24-4.45	0.179	188.8	9%	6-18	14.0
C	4	12.13	11.1-13.2	1.72	26.51	3%	1.1-3.1	11.7
D	4	14.65	13.5-15.9	2.23	18.29	4%	0.9-2	11.3
E	2	21.34	18.2-25.1	6.24	8.80	6%	2-6	12.6

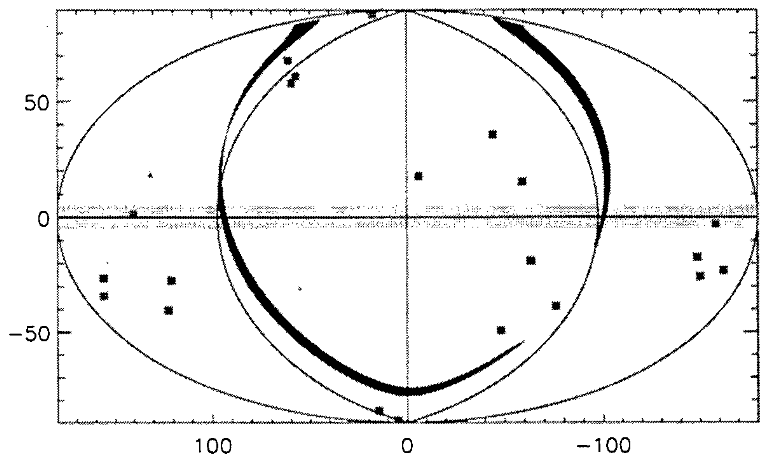

Figure 1: MSX Survey coverage in Galactic coordinates.

strips highlight the 4% of the sky IRAS did not survey. The 10° wide horizontal band across the center of the plot is the MSX survey of the Galactic Plane. According to the IRAS Explanatory Supplement, the high source densities and structured background over ± 100° longitude were sources of clutter noise which degraded the IRAS sensitivity. MSX also mapped those regions away from the plane that IRAS labeled as confused. These patches at various places in the sky are isolated regions of complex extended emission or high source density: molecular clouds, H II regions, and various galaxies such as the Large and Small Magellanic Clouds. The survey measurements were made with long scans designed to quickly cover the designated area. The nominal scan rate was 0.125° per sec (2.85 samples/dwell) and length of the scans varied between 122° for the shorter scans in areas missed by the IRAS experiment, to 182° for the Galactic plane survey.

3.1 The Galactic Plane Survey

Confusion degraded the IRAS sensitivity when the source density exceeded ~40/sq. deg. The MSX pixels are ~35 times smaller than the IRAS mid-infrared detectors. This, and the better Band A inherent sensitivity, enabled MSX to probe far deeper into the Galactic Plane than IRAS. MSX surveyed the Galactic plane to ± 5° latitude. Individual scans were along constant Galactic latitude at a nominal rate of 0.125°/ sec. The scan rate was reduced to 0.1°/ sec the last two months of the mission to partially compensate for higher dark current noise. Adjacent scans in a single survey were offset by ~0.45°, resulting in single coverage in each of the B bands and redundant coverage in the other bands. A second survey, with scans offset by 0.2° from the first, covered the Galactic plane to ± 3° latitude and the area between 300° to 120° longitude out to ± 4.5° latitude. Twenty-three 1° × 3° raster scan observations at selected locations in the Galactic plane provide even deeper probes of Galactic structure and validation of the reliability and completeness of the Galactic plane survey.

The MSX survey observations were median filtered to remove the background and pattern noise from dark current error. The low frequency component of the median filter was saved into the diffuse background file. The filtered (background subtracted) data were cross-correlated with the mean Point Response Function (PRF) in each band. Potential sources have been extracted using a signal-to-noise criterion. The flux and position of the potential source was quantified by a chi-square simultaneous fit of flux and position using the position dependent PRF. The position dependence of the PRF accounted for the slight variation in PRF shape over the focal plane array in cross-scan. The variances used in the chi-square fit are sums of the squares of the calculated noise and the Poisson photon noise. Multi-band observations are combined, then redundant observations from overlapping scans are found and a geometric mean of the flux is calculated (variability being noted). Band merging is done first as the local relative positions are much more accurate than those from overlapping scans.

Version 1.2 of the MSX Galactic plane survey catalog contains 323,052 sources (three times as many as IRAS in the same region). The sensitivity estimates in Table 1 are based on differential source density vs. flux plots for the extracted sources. Since the response over the pixels in an array is quite uniform (pixels with response >5% from the mean were rejected) such an estimate reflects the limit of completeness. The redundancy in the overlapping scans is used to establish reliability. The second set of redundant scans was executed approximately two months after the first, time enough for many of the variable stars to manifest their time dependent brightness. The variability is noted in the source list.

3.2 Areas Missed by IRAS

Approximately 4% of the sky is missing from the IRAS catalogs, because these areas were either never surveyed, or surveyed only once before the cryogen aboard IRAS was depleted. To complete the whole sky catalog of mid-IR sources, the MSX satellite surveyed the two coverage gaps between ecliptic longitudes of 157.5° - 165° (referred to as Gap 1) and 338° and 344.7° (Gap 2). As in the Galactic plane survey, the nominal scan rate was $0.125°/s$. For scans later in the mission, the scan rate was slowed to $0.0625°/s$ in order to recover some of the sensitivity lost by the warming of the focal plane. Interleaved short (122° or 130°) and long (157° or 161°) scans were performed, using cone and clock angle scans to reproduce IRAS-like coverage patterns. The scans were interleaved such that a minimum of three redundant passes over each area were made. The IRAS gap portion of the MSX PSC Version 1.2 contains 6,260 sources.

4 Data Processing and Calibration

The diversity of MSX experimental objectives required a wide range of observing conditions, from looking at deep space to observing the Earth's limb and hard Earth. SPIRIT III had two operating modes and several gain states to accommodate the range of backgrounds and imaging rates. One mode used an internal scan mirror to rapidly sweep out a $1° \times 1.5°$ or $1° \times 3°$ field at a high data rate (25Mbps). The more sensitive mirror fixed mode used on the Celestial Background experiments had the spacecraft move to survey the area of interest. The integration times are longer in this mode and the data rate is correspondingly lower (5 Mbps). The instrument also had three gain states for the mirror scan mode and four gains in the mirror fixed mode. All the Celestial Background experiments were taken in the mirror fixed mode and a large majority used the highest gain.

The MSX program assigned the responsibility for generating calibrated data to the sensor manufacturer, Space Dynamics Laboratory (SDL) of the Utah State University (USU), to assure that the entire operating range of the sensor was calibrated and that the various PI teams obtained the same calibrated results. SDL not only had the responsibility for calibrating the instrument and characterizing the on-orbit performance but also for creating the software, called CONVERT, that converted the telemetry data stream into scientific units. CONVERT was supplied to the Data Analysis Centers (DACs) that supported each PI team. The PI teams were required to use this software to obtain program "certified" results. The PI teams created the automated processing that processed the CONVERT output into analyzable products.

The Data Certification and Technology Team (DCATT), with Dr. Thomas Murdock as PI, was given the responsibility of validating the calibration process and to beta test and certify the software. Dr. Ray Russell was the DCATT team member who provided direct oversight of the SDL effort. The ground and on-orbit calibration and performance characterization experiments were planned and analyzed by the SDL Performance Assessment Team (PAT). The PAT consisted of SDL engineers, Dr. Ray Russell and Dr. Russell Walker, a MSX Celestial Background Team co-Investigator with expertise in calibrating space-based infrared astronomy experiments.

4.1 MSX Data Pipeline and CONVERT Processing

The data flow from the telemetry downlink to analysis is shown in Figure 2. The various data levels used by the MSX program are:

- Level 0 - the downlinked data stream,
- Level 1 - time ordered telemetry data and data products,
- Level 2 - calibrated raw data,
- Level 3 - reduced data suitable for analysis, for example, source lists and images, and
- Level 4 - analyzed science results, e.g., the MSX PSC.

4.1.1 Level 0 - Raw Telemetry Data

Raw telemetry data from an experimental observation, called a Data Collection Event (DCE), were downlinked to the Mission Control Center (MCC) located at the Applied Physics Laboratory (APL) of the Johns Hopkins University (JHU) during satellite passes over the ground station in Columbia, Maryland. The Level 0 data are the analog tapes exactly as downlinked and recorded at the ground station.

4.1.2 Level 1 and 1A Telemetry Data

The Mission Processing Center (MPC) at JHU/APL received the Level 0 analog tapes from the MCC. The MPC converted the Level 0 data into computer-compatible format - the Level 1 data. These data were permanently archived, but not distributed. Level 1A data are computer-compatible raw data that have been time-ordered for each DCE and separated by MSX instruments. The Level 1A data were sent concurrently to the SPIRIT III Data Processing Center (DPC) at the Utah State University/Space Dynamics Laboratory (USU/SDL) and to the AFRL/VSB Data Analysis Center (DAC). The Level 1A data have also been permanently archived.

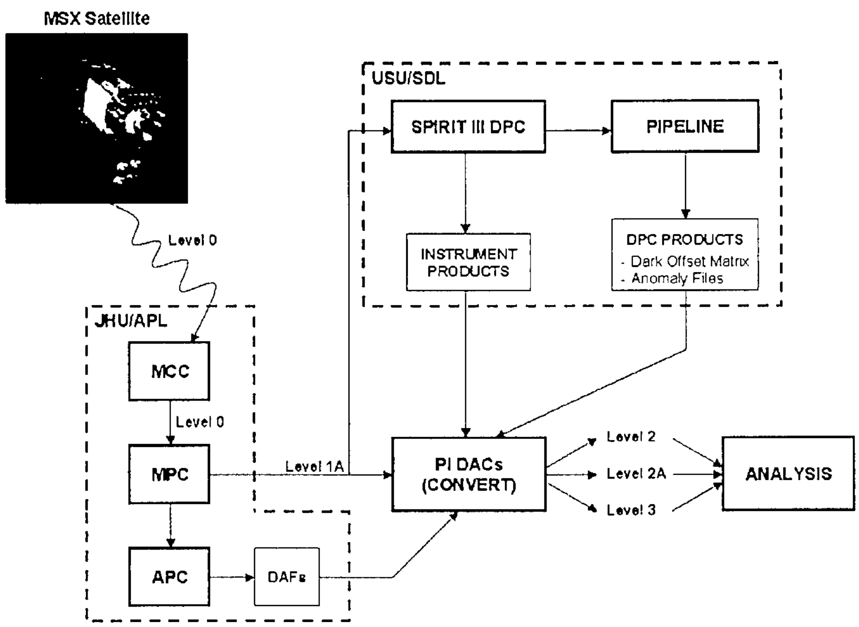

Figure 2: Schematic diagram of MSX dataflow from spacecraft to end-user.

Table 2: MSX DPC Products

DPC Products (DCE Unique)		Anomaly Files and Bounds
		Dark Offset File
Radiometer Instrument Products (General Calibration Constants)		Scan Mirror Transfer Function (SMTF) and Distortion Mapping
		Radiance and Irradiance Responsivity
	Corrections	Linearity
		Array Responsivity Trend
		FOR Uniformity
		Integration Mode Normalization
		Detector Responsivity Trend
		Non-Uniformity
		Backup Dark Offset
		Responsivity Temperature
		Point Source Extraction Amplitude over Field of Regard
		Autocollimator Coefficients
		Minor Frames to Skip after Turnaround and Mode Change
		Field Stop Positioning
		Coalignment
		Scan Mirror Velocity Functions
		Point Response Function (PRF)
		Dead Pixel Mask
		Readout Time

4.1.3 Data Processing Center (DPC) at SDL

The SPIRIT III DPC Pipeline at USU/SDL provided DPC Products, which are necessary to convert Level 1A data into Level 2 data. There are two types of DPC Products: performance information for each DCE, such as the dark offsets and sensor anomalies, and calibration files. The DPC files and their contents are listed in Table 2. These products essentially define the calibration of the infrared instrument for each DCE.

The DPC Pipeline software strips out housekeeping information and the dark current and stimulator flash data from the Level 1A tapes. The Pipeline flags anomalies such as "glitches" and saturated pixels and determines the dark offset matrices for the DCE. It also calculates the first four standard statistical parameters (mean, standard deviation, skew and kurtosis) for each pixel in ~33 second blocks, called a "scene". Any data taken when the sensor was outside of the "operational envelope" of certified sensor parameters is flagged in the Radiometer Anomaly file. The anomaly default in the CONVERT process (see below) is replacement of the datum with not-a-number (NaN). This was required for the Level 2 output to be validated as DCATT_CERTIFIED.

Radiometer Instrument Product files were issued by the sensor vendor in conjunction with the CONVERT software, which converts Level 1A into Level 2 data. These products are described in more detail in Section 4.2.

4.1.4 Definitive Attitude Files

The required absolute pointing knowledge from the spacecraft was ~1.9″. The APL Attitude Processing Center (APC) generated the pointing time history for each DCE and issued it as a Definitive Attitude File

(DAF). The APC combines attitude history from the spacecraft gyroscopes with updates from the star camera and pointing offsets of the boresight of each instrument from the spacecraft optical fiducial. The Mission Processing Center sends the DAFs to SDL and the AFRL/VSB DAC. The spacecraft ephemerides are passed along as part of the DAF files. The software known as Pointing CONVERT converts DAF quaternion data to Earth Centered Inertial (ECI) coordinates and corrects the inertial pointing for annual and spacecraft aberration.

4.1.5 The CONVERT Process

The Radiometer Standard CONVERT processed the data through Equation (1) to obtain Level 2 data.

$$r_{c,d,t} = B\left[\frac{G_{i,a}}{R_d T_a F_a N_{i,d}} L_{i,a}(r - D_{i,d,t})\right] \tag{1}$$

where

$r_{c,d,t} \equiv$ correct response in counts (Level 2 data) for detector (d) at time (t)
$B[\ ] \equiv$ bad pixel operation
$G_{i,a} \equiv$ integration mode normalization for integration mode (i) and array (a)
$F_a \equiv$ focal plane distortion correction for array (a)
$N_{i,d} \equiv$ non-uniformity correction for integration mode (i) and detector(d)
$L_{i,a} \equiv$ linearity correction function for integration mode(i) and array(a)
$r \equiv$ response in counts (Level 1A data)
$D_{i,d,t} \equiv$ dark offset counts for integration mode (i), detector (d) at time (t)
$T_a \equiv$ responsivity temperature correction for array (a)
$R_d \equiv$ responsivity trending correction for detector (d).

The DPC products and the Radiometer Instrument Products (RIPs) provide the information for correcting each pixel to a linear response on the same scale. The Level 2 output is digitized at a quarter of the level of the input. Canonical CONVERT applies Equation (2) to obtain radiance (W cm^{-2} sr^{-1} pixel^{-1}) and applies the focal plane distortion map to locate the pixels in focal plane coordinates. The Celestial Background Automated processing tapped into Canonical CONVERT at this point for its input data.

$$L_{d,t} = \frac{1}{R_{L,a}} r_{c,d,t} \tag{2}$$

where

$L_{d,t} \equiv$ measured radiance in W cm^{-2} sr^{-1} for detector (d) at time (t)
$R_{L,a} \equiv$ peak radiance responsivity in counts/(W cm^{-2} sr^{-1}) for array (a)
$r_{c,d,t} \equiv$ correct response in counts (Level 2 data) for detector (d) at time (t).

Canonical CONVERT could further process the data by applying Pointing CONVERT to output position tagged radiance for each pixel or use these data to create an image from 2400 minor frames. This translates into a $1^\circ \times 4.167^\circ$ image (a scene) at the survey scan rate. Running the Radiometer Canonical Process through to completion would extract point sources from the images and calculate their irradiances in units of W cm^{-2} (in-band irradiance). This software looked for maxima in the image, then used a "cookie cutter" to extract the source, *i.e.* excising a small block of data centered on the source. A background is determined from an annulus centered on the source and subtracted. The total source radiance is the sum of the pixel values and the irradiance is then calculated by means of Equation (3)

$$E_a = \frac{\Omega_{EFOV}}{R_{L,a}(1-S)} P[r_c, PRF_a] \tag{3}$$

where

$$\begin{aligned}
E_a &\equiv \text{ measured irradiance in W cm}^{-2} \text{ for array } (a) \\
\Omega_{EFOV} &\equiv \text{ effective field of view solid angle in steradians} \\
S &\equiv \text{ out-of-field-of-view scatter coefficient} \\
P[\quad] &\equiv \text{ point source extraction operation} \\
r_c &\equiv \text{ correct response in counts (Level 2 data)} \\
R_{L,a} &\equiv \text{ peak radiance responsivity in counts/(W cm}^{-2} \text{ sr}^{-1}\text{) for array } (a) \\
PRF_a &\equiv \text{ point response function for array } (a).
\end{aligned}$$

This procedure works well on reasonably bright isolated sources in regions where the background is flat, precisely the requirements for the MSX calibration stars. Canonical CONVERT was used by the SPIRIT IIII Performance Assessment Team to obtain irradiances of the calibration stars measured during the on-orbit calibration DCEs.

The Celestial Backgrounds automated processing used a much more sophisticated extraction routine. Consequently, the irradiances derived by the two extraction processes must closely agree for the SPIRIT III ground and on-orbit calibration pedigree to apply to the MSX PSC. The agreement was confirmed by a comparison of the irradiances extracted on the stellar standards using the Canonical Process and the Celestial Backgrounds source extractor. These data were from another Celestial Background experiment designed to use MSX to establish a set of secondary absolute stellar standards.

The Level 2 data precursors for this version of the MSX Point Source Catalog were produced using CONVERT 5, the penultimate version of the CONVERT software. The final release, CONVERT 6, is an upgrade to the final software to process the interferometer observations. There were no significant changes to processing the radiometer data.

4.2 Calibration and Radiometer Instrument Products

The Radiometer Instrument Products (RIPs), such as the (focal plane array temperature-dependent) system responsivities and the position dependent point response functions, are listed in Table 2. These quantities are the variables in Equation (1), except for DCE-unique terms such as the dark offsets and the bad pixel flags. The RIPs are calibration products that apply to all DCEs and were released episodically by SDL as the calibration was improved. Thus several RIPs were issued for each version of CONVERT. The SPIRIT III Performance Assessment Team was responsible for determining the calibration and sensor performance parameters.

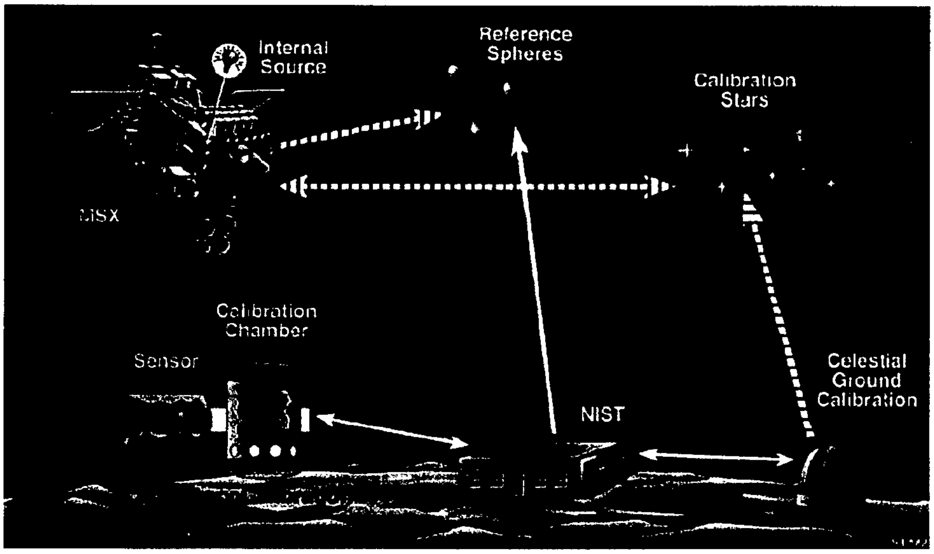

Figure 3: SPIRIT III calibration.

4.2.1 Calibration Methodology

SPIRIT III was calibrated by three different methods: on the ground using a cooled vacuum chamber constructed for that purpose; on-orbit using stellar standards; and with calibrated reference spheres released by the spacecraft periodically during the mission. Each method provides unique information on the sensor radiometric parameters but with sufficient overlap to cross-tie the different calibrations. A conceptual depiction of this process is shown in Figure 3. NIST validated the blackbody sources used in the ground calibration and the emissivity of the reference spheres. Reference to the ground-based absolute calibration of the standard stars is also shown. The *SPIRIT III Integrated Ground and On-orbit Calibration Report in Support of Convert 5.0* (SDL/USU 1998) describes the SDL calibration and trending procedures and results. This, and related documentation, can be found at **http://www.arnold.af.mil/amsc/**.

On the ground, the SPIRIT III instrument was attached to the Multifunctional Infrared Calibrator (MIC2), a cryogenically cooled vacuum chamber built by SDL, through vacuum, thermal and radiation shielded interfaces. The four calibration sources in the MIC2 are: a collimated source; a Jones source; an extended source; and a scatter source. The collimator filled the aperture of the telescope with flux from quasi-point and small extended sources collimated by means of a folded Gregorian telescope. The Jones source is a small area near-field source partially filling the entrance aperture of the telescope that floods the focal plane. The extended source is a temperature controlled, highly emissive plate large enough to completely fill the entrance aperture. Inserting a scatter plate into the optical path provides a full aperture, full-field low throughput source.

The ground calibration probes the entire system throughput in a fashion that is difficult or impossible to do on-orbit. The relative system spectral responses for the SPIRIT III infrared filter bands (see Appendix A) are an example of calibration that can only be done from the ground. The photon noise and the non-linear response of the detectors at high flux are more accurately and efficiently characterized with stable sources on the ground. Stable, flat extended sources with accurately known radiance to calibrate the radiance

Table 3: SPIRIT III Primary Calibration Stars

STAR	B_1(W cm^{-2})	B_2(W cm^{-2})	A (W cm^{-2})	C (W cm^{-2})	D (W cm^{-2})	E (W cm^{-2})
α Boo	5.63×10^{-15}	8.83×10^{-15}	1.45×10^{-14}	1.70×10^{-15}	1.04×10^{-15}	6.50×10^{-16}
α Lyr	3.31×10^{-16}	5.38×10^{-16}	8.20×10^{-16}	9.25×10^{-17}	5.69×10^{-17}	3.54×10^{-17}
α Tau	4.68×10^{-15}	7.39×10^{-15}	1.31×10^{-14}	1.57×10^{-15}	9.54×10^{-16}	6.03×10^{-16}
α CMa	1.16×10^{-15}	1.88×10^{-15}	2.84×10^{-15}	3.19×10^{-16}	1.96×10^{-16}	1.21×10^{-16}
β Peg	2.81×10^{-15}	4.49×10^{-15}	7.52×10^{-15}	9.17×10^{-16}	5.72×10^{-16}	3.57×10^{-16}
β Gem	9.98×10^{-16}	1.60×10^{-15}	2.50×10^{-15}	2.87×10^{-16}	1.79×10^{-16}	1.10×10^{-16}

responsivity of the system are rare in the celestial or Earth backgrounds.

The second leg of the calibration triad are standard stars, the fundamental references used for infrared astronomy. The stars are a true point source to the system and the calibration against them corrects the ground calibration systematic errors arising from the fact that the pinhole used with the collimator only approximates a true point source.

Similarly, the position dependent Point Response Functions (PRFs) can only be determined from the (calibration) stars. The MSX calibration stars are listed in Table 3 along with the absolute irradiances in each of the spectral bands. Five dedicated experiments used these stars to calibrate the instrument and to monitor the point source response as a function of scan rate and gain step during the mission. The five experiments measured:

- The radiometric calibration of every pixel in the mirror scan mode and all gain states by slowly moving a calibration star in cross-scan as the mirror swept the star across the focal plane arrays.
- The radiometric calibration of every pixel in the mirror fixed mode and all gain states by slowly moving a calibration star down each column in the focal plane arrays.
- The time and focal plane temperature dependence of the instrument response by relatively frequent, short observations in mirror scan mode that repeatedly swept a calibration star over the same subset of pixels in each spectral band.
- The same subset of pixels in each array in the mirror fixed mode in each of the four gain modes to calibrate the gain steps.
- The dependence of response on scan rate.

All of the primary calibration stars are bright (the faintest is α Lyr) and have infrared spectral energy distributions that decrease steeply with wavelength. Further, they only span a factor of $\sim$20 in irradiance. This meant that these sources were at the top end of the dynamic range in Band A but that α Lyr was barely detectable in Band E for the calibration experiments. The reference spheres provide an independent calibration that exercises the full dynamic range of the instrument.

The three emissive reference spheres were designed and constructed to be absolute calibrators for the SPIRIT III instrument. They were as close to being blackbodies as possible and had carefully measured thermal properties that permitted an accurate calculation of their temperature. The spectral emissivity of a "sister" sphere was measured at NIST. Since the spheres were a limited resource, the first one was not ejected until two months into the mission, time enough for the initial SPIRIT III calibration and pointing alignment to be completed. The encounter geometries for the experiments using the remaining spheres were tailored not only to explore the full dynamic range of SPIRIT III but also to include standard stars in the sensor field of regard. This provides a cross-tie between the calibration using the stars and that derived from the reference spheres.

The spheres provide an independent calibration of the absolute peak irradiance responsivity of the instrument in each of the mid-infrared spectral bands. While the calibration against the standard stars easily meets the program requirement of 5% absolute accuracy in each band, it does not meet the more stringent requirement on the band-to-band ratio. The reference sphere data provide the most accurate measure of the band-to-band ratio. The DCATT team expects to finish the final calibration, which includes the results of the reference sphere experiments, by the fall of 1999. Version 2 of the MSX PSC will be produced using RIP files based on the final calibration.

4.2.2 Certification of Level 2 Data

The DCATT certification process is based on the premise that measurements by SPIRIT III on known sources can be used to predict the performance of the instrument in observing any source. For example, it is assumed that the trending (dependence of parameters on focal plane array temperature and time) calibration DCEs, which repeatedly sampled a small subset of pixels throughout the mission, applies to other pixels at arbitrary times. To assess the calibration accuracy under this assumption, SDL used only the calibration observations of α Boo to transfer the ground calibration to in-flight performance. The calibration observations of the other five calibration stars and the reference spheres were used by the DCATT to validate the SDL processing and to determine the absolute photometric accuracy.

The DCATT analysts created a histogram of the number of observations at a given irradiance from the repeated observations of the calibration stars. The first four moments of the distribution in irradiance and position (mean, variance, skew and kurtosis) were calculated. The mean value was taken as the irradiance and the measurement error was calculated as the square root of the variance if the skew and kurtosis are within acceptable limits.

The final DCATT certified accuracy of the sensor was defined as follows. The quantity b defines the bias between the truth value and the mean of the measured distribution, σ_t is the uncertainty in the truth value, and σ_m is the standard deviation of the measured distribution. These quantities are depicted in Figure 4. An additional uncertainty, σ_u, the estimated unprobed uncertainties associated with the performance of the instrument, may apply under operational conditions not quantified with calibration and/or trending measurements. The DCATT certified accuracy is the root sum square of the these quantities expressed in percentages:

$$\sigma_A = \sqrt{b^2 + \sigma_t^2 + \sigma_m^2 + \sigma_u^2}. \tag{4}$$

As the calibration process continued through the mission, the unknown uncertainties were removed. In the final certification, σ_u was eliminated in the irradiance calibration.

The DCATT team analyzed the observations of the primary calibration stars listed in Table 3 and the five emissive reference spheres. The statistical parameters obtained from these observations were used in setting the certified accuracy. Burdick and Morris (1997) calculated the absolute irradiance of the standard stars in Table 3 from the "composite spectra" of Cohen et al. (1999 and references therein). The SDL PAT used only α Boo for the on-orbit calibration of the SPIRIT III instrument. The DCATT analysis of the observations of the remaining stars in the table provides an independent assessment of the accuracy of the calibration.

The observations were processed through CONVERT to create an ASCII archive containing only the data needed for certification. The DCATT analysis software consists of tools that display the data in the

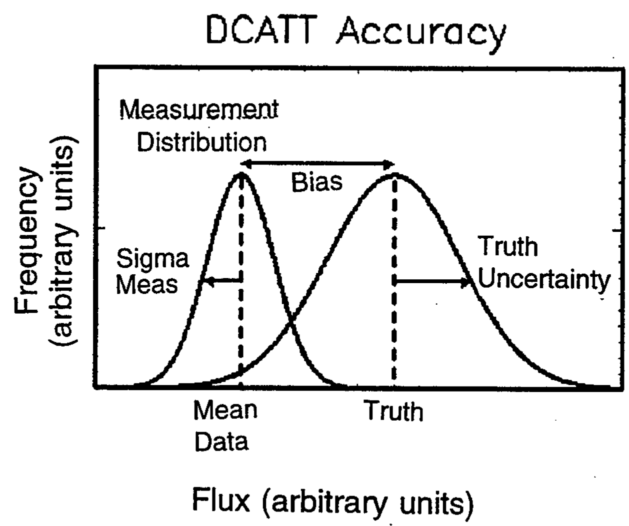

Figure 4: A representation of bias and uncertainties used in Equation (4).

Table 4: DCATT Certified Irradiance Accuracy Values from CONVERT 5.0 ($T_{fpa} < 13.0$ K)

Band	Certification Analysis Results: Bias (%)	Certification Analysis Results: 1σ Precision	Truth Uncertainty (%)	Total Irradiance Accuracy (%)
A	2	3	2	5
B_1	4	3	8	9
B_2	3	3	8	9
C	1	2	2	3
D	2	2	3	4
E	4	2	4	6

ASCII point source files and routines that calculate the mean and moments of the radiance, irradiance and goniometry along with their observed distributions.

Table 4 lists the DCATT certified values for the accuracy of the band averaged (over all pixels) point source irradiances using CONVERT 5, the version used to create the MSX PSC. The columns in the table show the relative contributions of the uncertainties in bias, precision (repeatability) and "truth" to the overall accuracy. The DCATT analyses eliminated the unprobed uncertainties in the irradiance.

4.3 Celestial Automated Process

The Celestial Backgrounds automated processing software operates on Level 2A MSX data. At this stage, the data has been passed through the USU/SDL CONVERT software, which converts counts per pixel to engineering units of W cm^{-2} sr^{-1} per pixel. The data from each pixel in each array are also time ordered. Upon reading the Level 2A data, the Celestial Automated Process runs the USU/SDL Pointing CONVERT software, which assigns each pixel a spatial position. The CONVERT software divides the data set into individual scenes of $192\times2400\times N$ pixels, where N is the number of active columns in the band. The source extractor works on one of these scenes at a time.

4.3.1 Source Extraction Algorithm

Initially we need to remove background trends from the data and compute the noise variance of the data for point source extraction. Because there is pixel-to-pixel variation in detector noise and in background level, we first apply a pseudo-median filter to the time-series data from each detector, i. The result is a smooth, low frequency, background output file and another data-stream containing the point sources and high frequency noise. The low frequency data contain any offset in the base pixel detector value and flux due to low frequency background from extended emission. The high frequency data have a mean of approximately zero, and are used to compute the noise variance, σ_i^2, for each detector.

After background removal, the high frequency data are assembled in ordered focal plane coordinates, forming a 2-D data array. At each grid point, the data are conlvolved with a matched filter, an idealized PRF. Matched filtering is a standard tool in communications theory and increases the visiblity of data that looks like the filter. Typically a gain of 1.7 in signal-to-noise is realized. The convolved data are thresholded to find positions of candidate point sources. A Levenberg-Marquardt fitting procedure is applied to the candidate point sources, simultaneously determining the point source position (x, y) and radiance. The procedure also calculates a χ^2 goodness of fit measure, and returns a formal covariance matrix which we use as estimates of the errors in the three parameters.

Data Filtering The dark current modeling and non-uniformity corrections (flat-fielding) done by CONVERT leave variations in the offset levels of each detector. Each detector also has its own associated noise variance, which must be known for the point source parameter fitting. Additionally, it is necessary to remove any extended background emission in the area of a point source in order to determine the source radiance. The median filter is a general technique used to suppress noise in images. For one-dimensional data, the filter is a sliding window covering an odd number of data points. The center pixel in the window is replaced by the median of the data points in the window. This filter will remove impulse functions less than one-half of the window width. This filter will not affect discrete step functions in data or ramp functions. The median filter is therefore tunable to filter out point sources and high frequency noise in the MSX data, leaving behind the low-frequency background.

Computation of the median is expensive however, growing exponentially with the window size. We therefore examined the pseudo-median filter, first described by Pratt et al. (1984). While retaining many of the properties of the median filter, the pseudo-median is computationally simple. For a window of length L, the pseudo-median is defined as (Pratt 1991)

$$PMED\{S_L\} = (1/2)MAXIMIN\{S_L\} + (1/2)MINIMAX\{S_L\} \tag{5}$$

where $\{S_L\}$ is the sequence of elements $s_1, s_2, ..., s_L$, and

$$\begin{gathered} MAXIMIN\{S_L\} = \\ MAX\{[MIN(s_1, ...s_M)], [MIN(s_2, ...s_{M+1})], ..., [MIN(s_{L-M+1}, ...s_L)]\} \\ MINIMAX\{S_L\} = \\ MIN\{[MAX(s_1, ...s_M)], [MAX(s_2, ...s_{M+1})], ..., [MAX(s_{L-M+1}, ...s_L)]\}. \end{gathered} \tag{6}$$

In the above equation, $M = (L+1)/2$. The MAXIMIN sequence always results in a number which is less than or equal to the median of the sequnce, while the MINIMAX operator returns a value greater than or equal to the median. Averaging the results tends to cancels out biases. In an analysis of sequences of $M = 5$ (Pratt 1991), the 120 possible arrangements of elements yield 8 cases where the pseudo-median is equal to the median, and the pseudo-median is never one of the extrema of the sequence. In most cases, the pseudo-median is the average of the two data values on either side of the median. Pratt also briefly discusses the cascade operators

$$MAXIMIN\{MINIMAX\{S_L\}\} \tag{7}$$

and

$$MINIMAX\{MAXIMIN\{S_L\}\}. \tag{8}$$

The examples for the above filters are salt and pepper impulse noise in images. The MINIMAX operator removes dark (pepper) noise, while the MAXIMIN removes the bright (salt) impulse noise, and the PMED filter attenuates both noise types. The cascade operators above also filter out both noise types, and, according to the examples shown in Pratt, preserve the background (image) edge information better than either the pseudomedian or median filters. However, like the MINIMAX and MAXIMIN filters, each of the cascade filters shown above is biased above or below the median. Therefore we have developed a "cascade average" filter

$$C_{AVE}\{S_L\} = \left(\frac{1}{2}\right) MAXIMIN\{MINIMAX\{S_L\}\} + \left(\frac{1}{2}\right) MINIMAX\{MAXIMIN\{S_L\}\} \tag{9}$$

which approximates the median of the data and preserves the edge information in the background. Examination of the MSX image data shows that the background can be highly structured, especially in the Galactic plane. For accurate flux estimation of point sources in these regions it is critical that the background removal be correct.

For our purposes the size of a point source as seen by a single detector is a function of the scan rate. For the astronomy experiments on MSX, these rates range from $0.125°/s$ to $0.02°/s$ (2181 $\mu rad/s$ to 349 $\mu rad/s$). At detector read-out rates of 72 Hz, the data are oversampled in the scan direction, taking one sample every 30.3 to 4.85 μrad (2.85 and 17.82 samples per 89 μrad pixel).

The width of a sampled point source (in microradians) will be equal to the detector size, δ, plus the angular size of the point source on the focal plane. In the ideal case, the diffraction limited size of a point source would be the diameter of the Airy disk and the total angular extent of the sampled point source is therefore

$$\alpha = \delta + 2 \times \frac{1.22\lambda}{d} \tag{10}$$

where λ is the longest wavelength covered by the passband, and d is the diameter of the telescope primary mirror, which for SPIRIT III is 33 cm. For real systems, the point source size is determined by a convolution of the pixel response and the band averaged (in λ) Airy function, and is larger than the ideal case. In fact, calibration data from USU/SDL indicates that the PRFs of the SPIRIT III telescope are larger than the diffraction limited cases. In Band A, the diameter (to the 1% contour) of a point source is about 180 μrad, or two detectors. Band E is slightly larger, with a diameter of about 210 μrad. Recalling that the window size (in data samples) of our filter depends on the number of samples in a point source, we determine that the pulse size, N, should be the size of a point source in sample space:

$$N = \frac{\alpha}{r} \tag{11}$$

where r is the sample rate in radians per sample. The filter window size size can then be set as $L = 2N + 1$, rounding N up to an integer value. One obvious consequence is that the filter window size will be band dependent, since α is set by the longest wavelength in the bandpass in question. The method will break down in regions of high source density such that there are sources within N samples of each other.

Faint source estimation The IRAS Faint Source Survey (FSS) Explanatory Supplement (Moshir et al. 1992) noted that windowed filters will underestimate the flux of faint sources due to biasing of the background estimate by a source in the window. While true for sources of any strength, it is a larger percentage effect for faint sources, resulting in increasing underestimation of source flux as the signal-to-noise ratio (SNR) decreases. The FSS processing adopted a modified median filter, which excluded the central 5 out of 23 points, to avoid this problem.

To examine the potential severity of this problem for the cascade average filter we ran Monte Carlo simulations of data sets at various SNR levels, comparing results from the cascade average filter and a modified median filter as used by the IRAS FSS. In addition to providing good estimates of the background in the region of point sources, we use the data filtering results to compute detector noise estimates and as the input to the diffuse background file. It is therefore important that the filter preserve the character of the extended background and of the noise spectrum.

The simulations have demonstrated that the cascade average filter provides a superior result to the modified median filter especially in confused regions and over extended emission. We find that at the source position, the background estimates from the cascade average and modified median filters are essentially the same. The behavior off the point source is quite different however. Even as the modified median de-weights the source for the "on" position, it assumes increased weight for the background estimate of the off-source position. The estimate of the background made by the modified median filter near a point source is overestimated by about 13% in the SNR 1.5 case. This translates into the appearance of "holes" around a point source in the filtered data. These holes are apparent in Figure III.A.6 of the IRAS Faint Source Survey Explanatory Supplement, and are a severe problem in regions where point sources are closely spaced. The cascade average filter is not affected as severely in the off-source positions (<1% in the SNR 1.5 case), and does not dig the large holes produced by median filter methods. It is therefore a better filter to use in regions of high source density, such as the Galactic plane.

Another area in which the cascade average filter is superior to median filtering methods is in its behavior over extended emission regions. As noted in the IRAS FSS Explanatory Supplement (Section III.A.5) the modified median filter will produce negative side-lobes into structures larger than the scale of point sources. The cascade average filter is designed to preserve the shape of extended sources. In the Galactic plane, where the majority of the MSX data has been taken, extended emission abounds. For both point source identification and diffuse background determination it is imperative that we retain high fidelity to the extended emission. The cascade average filter accomplishes this goal.

Identifying Point Source Candidates After filtering the data, removing the background and estimating system noise, potential point sources are identified in the scene. First, a two-dimensional matched filter is centered on each point in the (384 cross-scan $\times$ 2400 in-scan) scene. A subset of the data in a window surrounding the point is convolved with the matched filter. The data window is an ellipse in data pixel space, where the cross-scan extent is $R/dx + 2$ pixels, and $R/dy + 2$ pixels in-scan. The radius R is defined in a control file for each band, and is the expected source extent in pixels. The quantities dx and dy are the pixel sampling distances in fractions of pixels. For the long scans at 0.125 deg/s, we used $10 \times M_a$ pixels in-scan (where M_a is the number of active columns in band a), and 5 pixels cross-scan for each column. For Band A, this is a total of 400 pixels in the window. For slow scans, this can be as high as 2100 pixels. Communications theory shows that to maximize the SNR, a matched filter should have the same functional form as the signal being sought. In our case, this would mean using the measured PRF as matched filter. The PRF exists as a tabulated quantity on a fixed grid. At every point where it is to be evaluated, a bilinear interpolation must be performed. For a given scene, this could be as many as $2100 \times 384 \times 2400$ instances. Since this step is used only to identify potential point source locations in the data and not to estimate parameters, we simplify the matched filter process by using a cubic B-spline for the PRF. The noise in the matched filtered scene is then estimated, and the scene thresholded above this level. A given point source may produce a number of data points above the threshold. These are examined to find the local maximum, which is reported as the initial guess at a point source position.

Parameter Estimation For each source in band a we estimate the source radiance, R_a, and position $(\xi, \eta)_a$ simultaneously using a χ^2 minimization technique. We model the data using the position dependent

PRF, H_a. The PRF of each band was measured on-orbit as part of the spacecraft calibration at the top, middle, and bottom of each focal plane. The measured PRF, H', was normalized to a peak value of unity, such that the effective field of view of the PRF is given by

$$\Omega_{EFOV} = \Delta x \Delta y \sum_{k=1}^{M} H_k' \tag{12}$$

where Δx and Δy are the grid sample spacings (in radians) and the PRF is sampled at M points. For the point source extraction software, the measured PRF is renormalized so that

$$H_k = \frac{H_k'}{\sum_{k=1}^{M} H_k'} \tag{13}$$

or

$$\sum_{k=1}^{M} H_k = 1 \tag{14}$$

which volume normalizes the PRF.

We can model a datum on array (band) a at a given point i in the Effective-Field-of-View (EFOV) window as (ignoring the noise contribution)

$$d_{a,i} = R_a H_a(x_i - \xi, y_i - \eta). \tag{15}$$

For a single point source then, we determine the radiance and position by minimizing χ^2, which is given by

$$\chi^2 = \sum_{i=1}^{N} \left[\frac{\rho_{a,i} - d_{a,i}}{\sigma_{a,i}} \right]^2 . \tag{16}$$

In Equation (16), $\rho_{a,i}$ and $\sigma_{a,i}$ are the measured data and associated standard deviation at detector i of band a. N is the number of data points in the data window as described in the above subsection. If we also take the possibility of blended sources into account, the quantity minimized is

$$\chi^2 = \sum_{i=1}^{N} \left[\frac{\rho_{a,i} - \sum_{k=1}^{K} R_{k,a} H_a(x_i - \xi_k, y_i - \eta_k)}{\sigma_{a,i}} \right]^2 \tag{17}$$

where K is the number of point sources in the data window. We use the Levenberg-Marquardt technique, adapted from the code described by Press et al. (1992). The technique performs a simultaneous fit of the three parameters, as well as providing a formal covariance matrix.

In the above procedure, the data, $\rho_{x,i}$ is reported in radiance units of $W\ cm^{-2}\ sr^{-1}$. The solution to the χ^2 minimization reports the radiance in a single PRF data element centered on a point source of radiance R_a (since the PRF has been volume normalized). To determine the irradiance, we must multiply this result by the effective field of view of a PRF data element, ω_{EFOV}.

The PRF is sampled on a regular grid where $\Delta x = \Delta y = 4.1667 \times 10^{-6}$ radians. For a staring sensor, with a volume normalized PRF, we define the effective field of view of the PRF element as

$$\omega_{EFOV}(staring) = \iint H d\Omega = \sum_{k=1}^{M} H_k \Delta x \Delta y = \Delta x \Delta y \sum_{k=1}^{M} H_k = \Delta x \Delta y. \tag{18}$$

When the sensor is used in scan mode, the coverage of additional area during the pixel dwell time must be taken into account. For a PRF that defines a perfectly circular field of view while staring, the scan mode field of view is an ellipse. Consider a perfectly circular PRF of radius R radians, taking data at a scan rate of ν radians per second over a dwell time of Δt seconds for each data sample, and scanning in the y direction. While the cross-scan axis is still $2R$, the in-scan axis is now $2R+ \nu\Delta t$. The effective field of view of the system is now $\pi R^2(1 + \frac{\nu\Delta t}{2R})$ steradians.

In the case of the MSX data, we know the instantaneous scan rate from the Definitive Attitude File, and the dwell time as a function of gain mode. For the scan mode calculation, we derive an effective PRF radius, R_{EFF}, based on the assumption that the PRF is circular with an effective area of Ω_{EFOV} steradians. The effective field of view for our PRF data element is therefore

$$\omega_{EFOV} = \Delta x \Delta y \left[1 + \frac{\nu\Delta t}{2R_{EFF}}\right] = \left[1 + \frac{\nu\Delta t}{2R_{EFF}}\right] \times 1.736 \times 10^{-11} \text{ steradians.} \tag{19}$$

Noise estimation The parameter fit requires that each data point have an associated noise value, by which the value is weighted. We have used a two component noise model, made up of detector noise and Poisson noise where

$$\sigma^2(i,t) = \sigma^2_{\text{detector}}(i) + \sigma^2_{\text{photon}}(i,t) \tag{20}$$

for a given detector, i, at readout frame time t.

The detector noise is computed from the 2400 values of the high frequency component of the filtered data for each detector in the focal plane array. Point sources have been removed from the data to prevent biasing the variance estimate to higher values. The Poisson noise component is a statistical consequence of the fact that the detectors are photon counters. The SPIRIT III instrument team at USU/SDL modeled the system noise as the root sum of the variance in detector noise and the variance of the Poisson distribution equal to the mean. The standard deviation of the photon noise is

$$\sigma_{\text{photon}} = A\sqrt{r} \tag{21}$$

where A is the photon noise coefficient, and r the offset and linearity corrected response in counts. As part of the ground calibration procedure at SDL, detector noise and the photon noise coefficient were determined for each SPIRIT III array and integration mode. These values, from Table 2.42 of the "*SPIRIT III Infrared Sensor Ground Calibration Report in Support of CONVERT 3.0*" are used in the point source extractor to determine $\sigma^2_{\text{photon}}(i,t)$.

4.3.2 Merging Multiple Observations

The MSX survey experiments were designed for redundant observations. All but about 20% of the Galactic plane was surveyed four times while the coverage is much higher in portions of the IRAS gaps. The confirming observations were used to reject spurious sources and combined to improve parameter estimation.

Band Merge Unlike IRAS, which treated the observations in each band as an independent survey, the data from different colors from a single DCE were merged before searching for confirming observations. The focal plane arrays in MSX Bands A, D and E were accurately superimposed as were the B and C arrays with dichroic filters. The relative position error for sources detected in the different bands was very small, less than 1″, and much more accurate than the absolute position error for a single scan, ~4″.

The band merge program uses associated sorts to quickly localize a comparison list to the neighborhood of the selected source. The sources are sorted in order of decreasing SNR, and the highest SNR source is the seed. After it has been band merged, the source with the next highest SNR becomes the seed and so forth.

Boresight Pointing Refinement The Definitive Attitude Files (DAFs) supplied with the Level 1A data typically had absolute pointing errors of 45″ (even larger on occasion). A User Rotation Matrix in Pointing CONVERT, with defaults of zero, permits a time dependent set of coordinate transformations to correct the pointing. The Boresight Pointing Refinement (BPR) program calculated a least squares poynomial fit to the differences of the positions predicted by the DAF for the astrometric stars detected in Band A in a DCE and their astrometric positions. Only Band A extractions were used in the pointing updates as this band was ~10 times more sensitive than the others. BPR transforms the polynomial fit into the time dependent correction for the User Rotation Matrix for a given DCE.

Sources extracted from a DCE are associated with those in the MSX Infrared Astrometric Catalog Verion 4.2.1. Egan & Price (1996) created this catalog as a resource for improving the pointing on the MSX Celestial Background experiments. This catalog address the deficiencies in the CPIRSS catalog (Hindsley & Harrington 1994) which made CPIRSS unsuitable for updating the MSX positions. The MSX IR Astrometric Catalog contains 177,860 astrometric stars known or calculated to be brighter than 8th magnitude in Band A; 61,242 of these have infrared counterparts in the IRAS PSC and Faint Source Survey (FSC) or the Catalog of Infrared Observations (Gezari et al. 1993). BPR forms associations for all astrometric stars within 0.03° of the positions of the extracted Band A sources. A flux criterion is applied to give a single match when more than one MSX object is associated with a given astrometric star. The 0.03° association radius is the maximum error allowed by BPR as the routine does not iterate on the associations. The number of associations range from ~15 for short DCE segments to over 500 for a Galactic plane survey scan.

BPR time orders the associated extractions. Pointing CONVERT is used to transform the astrometric positions into focal plane coordinates. An iterated, weighted least square solution for the in-scan and, independently, cross-scan errors is calculated. The initial solution uses equal weights and subsequent solutions weight the values by the inverse of the deviations determined by the previous fit. The iterations continue until a minimum is found in the χ^2 value of the fit. The order of polynomial is also iterated; most solutions converge to fifth order. The weighting reduces the influence of outliers with large deviations receiving small weights. The weighted iterated solution is essential to reduce the influence of spurious matches arising from the position-only criterion. The iterations do not trim the data by Cauchy editing, for example. Actually, three in-scan solutions were derived for the top, middle and bottom third of the focal plane to look for errors induced by rotation about the instrument boresight. There was no convincing evidence that such errors existed.

Pointing CONVERT provides a pointing history from the DAF and a smoothed "corrected" time history by inverting the least squares solution. The difference is used to form the User Rotation Matrix. Pointing CONVERT generates a new pointing time history using the DAF and User Rotation Matrix; a new least squares solution is derived and the appropriate corrections are applied to the User Rotation Matrix. The procedure is iterated until the solution using the DAF and updated User Rotation Matrix converges to a specified minimum variance or a maximum number of iterations is reached.

The DAFs occasionally produced discontinuities in the motion of the boresight. These discontinuities were, at most, a couple of arc minutes and were inevitably traced to times when the five brightest stars used for the star tracker updates changed. BPR has provisions for segmenting the updates to accommodate this situation.

Scan Merge Following Band Merge, sources from overlapping scans are merged. Scan merge is a two step process. The first pass uses a positional criterion that identifies all sources within a specified distance of each other. The second pass determines which, of any, multiple associations are most likely, then calculates a weighted mean for the flux and position. Sources are also flagged for variability, confusion and if they are not point-like.

Pass 1 Merge The initial associations were made if the positional difference of the seed and candidate source, Δr, satisfies the condition:

$$\frac{\Delta r^2}{\sigma_{in}^2(seed) + \sigma_x^2(seed) + \sigma_{in}^2(candidate) + \sigma_x^2(candidate)} < 10. \quad (22)$$

In Eqn. (22), the σ_{in} and σ_x are the uncertainties in the in-scan and cross-scan positions. As for the Band Merge procedure, we use an SNR-ordered list to choose our seed sources. In this case, we have SNR ordered the Band Merged source list.

Pass 2 Merge The second pass identifies the most likely association. Specific account is taken of the aspect-dependent error ellipses and, when necessary, flux information. While the rms error in the refined positions from BPR is about 3.5″ in both in-scan and cross-scan, the magnitude and asymmetry of the error ellipse can vary from scan to scan.

The problem of determining whether two measurements from different scans are of the same source can be expressed in statistical terms as testing the hypothesis that the means of two distributions are the same. In our case, the two distributions are the samples of measurements from the seed scan and any other scan. These distributions have known variances. In general, the test condition for testing the hypothesis that the mean of two distributions is the same, where the variance of both distributions is known, is

$$\frac{x_1 - x_2}{\sqrt{\sigma_1^2/n_1 + \sigma_2^2/n_2}} \quad (23)$$

where x_1 is the mean value as determined by n_1 independent measurements from distribution 1, and likewise for distribution 2. A confidence level is used to determine if the means are the same. The mean value of the position in a given scan is calculated from the individual position data in each color in which the source was seen.

The errors for the MSX source extractions have independent in-scan and cross-scan position variances. The BPR results indicate that the error distribution in both directions is normal, so the errors have a bi-normal distribution. The criterion to accept the hypothesis that two measurements are of the same source is

$$\chi^2 = \frac{\Delta r_{in}^2}{\sigma_{in,1}^2/n_1 + \sigma_{in,2}^2/n_2} + \frac{\Delta r_x^2}{\sigma_{x,1}^2/n_1 + \sigma_{x,2}^2/n_2} < N. \quad (24)$$

We set $N = 18.4$ which in a two-dimensional bi-normal distribution is the 99.99% confidence level.

4.3.3 Determination of Catalogued Source Parameters

Once the proper scan-to-scan merges are found, the best values of the source parameters (position and irradiance) and their respective uncertainties are calculated.

Position Data For most of the survey measurements, "in-scan" corresponds to lines of constant Galactic latitude. For the IRAS gaps, the in-scan direction is along lines of nearly constant ecliptic longitude. For most sources, redundant scans have nearly co-aligned error ellipses. This only breaks down near the North Ecliptic Pole and where the ecliptic scans cross through the Galactic plane scans.

In the general case, with N detections of a source, the final Right Ascension and Declination (α, δ) are given by

$$\alpha = \frac{\sum_{i=1}^{N} w_{i,\alpha}\alpha_i}{\sum_{i=1}^{N} w_{i,\alpha}}; \qquad \delta = \frac{\sum_{i=1}^{N} w_{i,\delta}\delta_i}{\sum_{i=1}^{N} w_{i,\delta}} \tag{25}$$

where for a given scan (i) the weights are:

$$w_\alpha = \frac{1}{(\vec{\sigma}_{in}\cdot\widehat{\alpha})^2 + (\vec{\sigma}_x\cdot\widehat{\alpha})^2} = \frac{1}{\sigma_{in}^2\sin^2(\theta) + \sigma_x^2\cos^2(\theta)}, \tag{26}$$

$$w_\delta = \frac{1}{(\vec{\sigma}_{in}\cdot\widehat{\delta})^2 + (\vec{\sigma}_x\cdot\widehat{\delta})^2} = \frac{1}{\sigma_{in}^2\cos^2(\theta) + \sigma_x^2\sin^2(\theta)}. \tag{27}$$

The variable θ is the angle, measured East from North, of the in-scan axis of the error ellipse at the point in question.

The error in the reported position is determined by convolving the 2-D error ellipse, making the assumption that both the in-scan and cross-scan uncertainty distributions are gaussian. Examination of the individual scan data indicate that this is a valid assumption. The total error distribution for each individual scan is therefore a bi-normal distribution. Convolving the N uncertainty distributions for the appropriate scans therefore yields another bi-normal distribution. Consider the case of two error ellipses with parameters (θ, a, b) and (θ', p, q) where a and p are the in-scan 1σ uncertainties and the uncertainty distributions are given by

$$f = A\exp\left[-\frac{y^2}{a^2} - \frac{x^2}{b^2}\right], \qquad f' = A'\exp\left[-\frac{y^2}{p^2} - \frac{x^2}{q^2}\right]. \tag{28}$$

It can be easily shown that the resulting error ellipse has the parameters (ϕ, u, v) where

$$\frac{1}{u^2} = \frac{1}{2}\left[\frac{\cos 2\theta(\frac{1}{a^2} - \frac{1}{b^2}) + \cos 2\theta'(\frac{1}{p^2} - \frac{1}{q^2})}{\cos 2\phi} + \frac{1}{a^2} + \frac{1}{b^2} + \frac{1}{p^2} + \frac{1}{q^2}\right], \tag{29}$$

and

$$\frac{1}{v^2} = \frac{1}{a^2} + \frac{1}{b^2} + \frac{1}{p^2} + \frac{1}{q^2} - \frac{1}{u^2}. \tag{30}$$

In those cases where the scans are co-aligned, the resulting error ellipse in-scan and cross-scan axes *do* correspond to the actual in-scan/cross-scan directions. For those cases where the scans are not co-aligned, the reported axes *do not* correspond to any physical quantity, but only reflect the statistical distribution of error in the measurement.

Irradiance Data The irradiance for each band is calculated as the weighted mean of the measurements. Because the variance reported out of the covariance matrix of the fit tends to be very small for very high SNR sources, we have found that weighting the irradiance by the reduced χ^2 quantity yields a better value for the irradiance. This is based on comparison of the MSX results to Infrared Space Observatory (ISO) spectra for bright Wolf-Rayet stars (van der Hucht *et al.* 1996). This is likely to be the case because of the greater probability of high SNR sources being disrupted by bad pixels, but still being identified as point sources which fit the PRF. A high χ^2 value indicates, however, that the match to the PRF was poor. The irradiance, L, for N detections in a given band, a, is given by

$$L_a = \frac{\sum_{i=1}^{N} \frac{L_{a,i}}{\chi^2_{a,i}}}{\sum_{i=1}^{N} \frac{1}{\chi^2_{a,i}}}. \tag{31}$$

The uncertainty associated with this value is given by

$$\sigma_{L_a} = \sqrt{\frac{\sum_{i=1}^{N} \frac{\sigma^2_{a,i}}{\chi^2_{a,i}}}{\sum_{i=1}^{N} \frac{1}{\chi^2_{a,i}}} + \sigma^2_{a,DCATT}}, \tag{32}$$

where $\sigma_{a,i}$ is the uncertainty (%) associated with the extraction method in the band a, and $\sigma_{a,DCATT}$ is the uncertainty inherent in irradiance measurements from SPIRIT III band a due to calibration issues as outlined in Section 4.2.2.

We also calculate the variance of the N measurements about this weighted mean. If there is only 1 measurement in a band, this quantity is set to -99.0.

In cases where a source was not detected in a passband, we give the negative of the upper limit of the irradiance. This limit is taken to be the limiting irradiance for source detection for the most sensitive scan covering the area of the sky in question. The flux uncertainty values and measurement variance are set to -99.0 in this case.

4.3.4 Flags

As an aid to users, we have a number of flags to indicate concerns about data quality. These concerns and how they have been dealt with have been discussed above, but the flags are the only way a user of the catalog knows when a source measurement is potentially problematic. We include in this catalog four important flags for each band. One overall flux quality flag and three specific flags for variability, confusion, and measurement reliability. Each flag has a value for each band.

The overall flux quality flag, Q_a (where a denotes the band designation $A - E$), can take on values from zero to four. The meaning of the flags and the conditions under which values are assigned are shown in Table

Table 5: Flux Quality flag levels.

Value	Meaning	Conditions (Galactic plane)	Conditions (IRAS gaps)
0	Not Detected	Not detected in this band in any scan	Not detected in this band in any scan
1	Limit	# detections in band, $N \geq 1$; SNR does not meet any of below criteria	# detections in band, $N \geq 1$; SNR does not meet any of below criteria
2	Fair/Poor	$N = 1$; $\text{SNR}_{HIGH} \geq 6.0$ or $N \geq 3$; $\text{SNR}_{HIGH} < 3.0$ or $N = 2$; $\text{SNR}_{HIGH} < 4.0$; $\text{SNR}_{LOW} > 3.5$	$N = 1$; $\text{SNR}_{HIGH} \geq 6.0$ or $N \geq 4$; $\text{SNR}_{HIGH} < 3.0$ or $N = 3$; $\text{SNR}_{HIGH} < 4.0$; $\text{SNR}_{LOW} > 3.5$
3	Good	$N = 2$; $\text{SNR}_{HIGH} \geq 4.0$ or $N \geq 3$; $\text{SNR}_{HIGH} \geq 3.0$; $\text{SNR}_{LOW} < 4.0$	$N = 2$; $\text{SNR}_{HIGH} \geq 6.0$ or $N \geq 4$; $\text{SNR}_{HIGH} \geq 3.0$; $\text{SNR}_{LOW} < 4.0$
4	Excellent	$N \geq 3$; $\text{SNR}_{LOW} \geq 4.0$	$N \geq 3$; $\text{SNR}_{LOW} \geq 4.0$

5. The number of sightings required for the IRAS gap sources are increased in order to minimize spurious sources in areas where many scans overlap.

The variability flag, V_a, reflects the variance in the individual measurements against the expected uncertainty of the quoted irradiance for band a. It can be either 0 or 1 under the conditions

$$\frac{\sqrt{\frac{1}{N-1}\left[(\sum_{j=1}^{N} L_{a,j}^2) - NL_a\right]}}{\sigma_{L_a}} \leq 3; \qquad V = 0 \tag{33}$$

$$\frac{\sqrt{\frac{1}{N-1}\left[(\sum_{j=1}^{N} L_{a,j}^2) - NL_a\right]}}{\sigma_{L_a}} > 3; \qquad V = 1.$$

The actual quantity calculated in the above equation is also given in the catalog listing.

The confusion flag, C_a, can also take on values of either zero or one. Zero denotes an unconfused source, while 1 indicates that there is a potential confusion problem. Confusion in this case means that there were two (or more) sources in the band in question in at least one of the scans, which fell within the 99.99% confidence ellipse described above, **or** there were at least two sources in a given scan and band within a radius of 1.5 detector pixels (27″) of the seed source.

The final flag in the catalog is a measurement reliability flag, R_a, based on how well the source extractor was able to fit the PSF, as determined by the value of the reduced χ^2. The flag also reflects the SNR level of the detections. The flag can take on values from zero to nine according to the formula

$$R_a = R_{a,\chi^2} + R_{a,SNR} \tag{34}$$

or $R_a = 9$ if the source was not detected in that band.

If all detections in band a have $\chi^2 < 3$, the R_{a,χ^2} component is set to zero. The R_{a,χ^2} component takes on a value of 1 if some χ^2 values are greater than 3 and some are less than three. It is set to 2 if all extractions in the band have $\chi^2 > 3$. If all extractions are poor fits to the PRF, this is generally an indication that the source is embedded in some nebulosity. It is often the case that quality 2 flags are seen in Bands A and E for sources in the Galactic plane. Examination of the MSX image data shows that nebulosity is more of a problem at these wavelengths, and to a lesser degree in Band C, as well. Quality flags of 1 tend to show up for brighter sources, and, as indicated above, are likely a result of a source detection corrupted by bad pixels. In any case, the reported positions and flux densities of sources for which $R_{a,\chi^2} > 0$ are likely to have larger uncertainties than those quoted in the catalog.

The $R_{a,SNR}$ component of the reliability flag can take on values of zero, three, or six. If the minimum SNR detection in band a is greater than three, $R_{a,SNR} = 0$. If the minimum SNR value is less than three, but the maximum SNR is greater than three, $R_{a,SNR} = 3$. If all the SNR values are less than three, $R_{a,SNR} = 6$.

5 Catalog Details

The catalog files are in ASCII format with entries as given in Table 6. The columns are space delimited (except for the variability, confusion, and measurement reliability flags, which are each given as a block), and were written out using the following FORTRAN format statement:

```
2002 format(a23,1x,f9.4,1x,f9.4,2(1x,f4.1),1x,f5.1,1x,i3,
     & 6(1x,1pe12.4,1x,i1,1x,0pf5.1,1x,f6.1,1x,f6.1,1x,i3,1x,f5.1),1x,6i1,1x,6i1,1x,6i1)
```

The MSX catalog names of the sources have been defined according to International Astronomical Union (IAU) conventions with a unique identifer combined with the position of the source. In this case, the MSX PSC v1.0 sources are named using the convention MSX5C_GLLL.llll±BB.bbbb, where MSX5C denotes that this is MSX data run using Version 5.0 of the CONVERT software, and GLLL.llll±BB.bbbb gives the Galactic coordinates of the source.

For ease of handling, the catalog is broken into six files. The coverage of the sub-catalogs is listed in the "Location" column of Table 7.

Table 6: Format of MSX Point Source Catalog files

Column	Format	Field	Units
1	a23	Name	
25	f9.4	Right Ascension	J2000 decimal degrees
35	f9.4	Declination	J2000 decimal degrees
45	f4.1	in-scan uncertainty (1σ)	arcseconds
50	f4.1	cross-scan uncertainty (1σ)	arcseconds
55	f5.1	scan angle	degrees E of N
61	i3	total number of sightings	
65	e12.4	Band B_1 flux density	Jy
78	i1	Band B_1 flux quality flag	
80	f5.1	Band B_1 flux uncertainty (1σ)	%
86	f6.1	lowest SNR value, Band B_1 detections	
93	f6.1	highest SNR value, Band B_1 detections	
100	i3	number of Band B_1 detections	
104	f5.1	variation of Band B_1 measurements	
110	e12.4	Band B_2 flux density	Jy
123	i1	Band B_2 flux quality flag	

Table 6: (continued)

Column	Format	Field	Units
125	f5.1	Band B_2 flux uncertainty (1σ)	%
131	f6.1	lowest SNR value, Band B_2 detections	
138	f6.1	highest SNR value, Band B_2 detections	
145	i3	number of Band B_2 detections	
149	f5.1	variation of Band B_2 measurements	
155	e12.4	Band A flux density	Jy
168	i1	Band A flux quality flag	
170	f5.1	Band A flux uncertainty (1σ)	%
176	f6.1	lowest SNR value, Band A detections	
183	f6.1	highest SNR value, Band A detections	
190	i3	number of Band A detections	
194	f5.1	variation of Band A measurements	
200	e12.4	Band C flux density	Jy
213	i1	Band C flux quality flag	
215	f5.1	Band C flux uncertainty (1σ)	%
221	f6.1	lowest SNR value, Band C detections	
228	f6.1	highest SNR value, Band C detections	
235	i3	number of Band C detections	
239	f5.1	variation of Band C measurements	
245	e12.4	Band D flux density	Jy
258	i1	Band D flux quality flag	
260	f5.1	Band D flux uncertainty (1σ)	%
266	f6.1	lowest SNR value, Band D detections	
273	f6.1	highest SNR value, Band D detections	
280	i3	number of Band D detections	
284	f5.1	variation of Band D measurements	
290	e12.4	Band E flux density	Jy
303	i1	Band E flux quality flag	
305	f5.1	Band E flux uncertainty (1σ)	%
311	f6.1	lowest SNR value, Band E detections	
318	f6.1	highest SNR value, Band E detections	
325	i3	number of Band E detections	
329	f5.1	variation of Band E measurements	
335	i1	Band B_1 variability flag	
336	i1	Band B_2 variability flag	
337	i1	Band A variability flag	
338	i1	Band C variability flag	
339	i1	Band D variability flag	
340	i1	Band E variability flag	
342	i1	Band B_1 confusion flag	
343	i1	Band B_2 confusion flag	
344	i1	Band A confusion flag	

Table 6: (continued)

Column	Format	Field	Units
345	i1	Band C confusion flag	
346	i1	Band D confusion flag	
347	i1	Band E confusion flag	
349	i1	Band B_1 measurement reliability flag	
350	i1	Band B_2 measurement reliability flag	
351	i1	Band A measurement reliability flag	
352	i1	Band C measurement reliability flag	
353	i1	Band D measurement reliability flag	
354	i1	Band E measurement reliability flag	

5.1 Source Statistics

MSX PSC Version 1.2 contains a total of 329,312 sources in the combined catalog. Of these, 323,052 are included in the Galactic plane survey (lying within $|b| < 6°$), and 6,260 are in the areas missed by IRAS at latitudes higher than $|b| = 6°$. Given the characteristic sensitivities of the SPIRIT III infrared arrays, most (~80%) of the sources were only detected in Band A. The breakdown of sources with non-limit detections ($Q_a \geq 2$) in each band is given in Table 7.

Table 7: Source count numbers by band and location.

Location	B_1	B_2	A	C	D	E
IRAS Gaps	64	96	6196	350	351	149
$2° < b \leq 6°$	413	465	63146	5139	5111	3080
$0.5° < b \leq 2°$	569	504	63806	7422	7607	4263
$-0.5° < b \leq 0.5°$	605	731	52612	10231	10853	6969
$-2° < b \leq -0.5°$	379	711	61655	8125	8191	4734
$-6° < b \leq -2°$	540	575	71279	5662	5556	3601

5.2 Flag Statistics

5.2.1 Flux Quality

For general purpose use, the flag which should be used to decide the trustworthiness of a quoted flux density is the flux quality flag, Q_a. In Section 6 we shall use this flag to aid in the analysis of the catalog sources. Table 8 details the number of sources in each quality category for each SPIRIT III radiometric band. The statistics are also broken down by sub-catalog location. To be included in the catalog, there must be at least one band for which $Q_a \geq 2$.

5.2.2 Variability

A variability flag of $V_a = 1$, denotes that the variation of the measurements over the MSX SPIRIT III mission is greater than $3\sigma_a$. Table 9 lists the number of sources in each band, as a function of location, which showed variability over the mission lifetime that is not likely to be due to statistical error in the measurements.

5.2.3 Confusion

Table 10 reports the number of confused sources (also reported by band) in various parts of the catalog. Examining these numbers for the density of confused sources (number per square degree), we find the expected result that confusion is an increasing problem toward the galactic equator. The lowest confusion density is away from the plane, in the IRAS gaps.

5.2.4 Measurement Reliability

Table 11 lists the measurement reliability flag statistics for the entire MSX PSC v1.0, for each SPIRIT III band. In this case, a value of $R_a = 9$ means that the source was not detected in band a. Most of the detected sources in each band fall in the $R_a = 0$ category, which means that they fit the point source function well and all measurements were of adequate signal-to-noise.

Table 8: Statistics of Flux Quality Flags.

		B_1	B_2	A	C	D	E
$Q=0$	IRAS Gaps	5624	5927	36	5483	5573	5515
	$2° < b \leq 6°$	61634	63292	1538	56913	57523	58451
	$0.5° < b \leq 2°$	61704	64110	1743	54995	55098	57701
	$-0.5° < b \leq 0.5°$	51310	53370	2598	41161	41440	44365
	$-2° < b \leq -0.5°$	60343	61427	1763	51676	52433	54937
	$-6° < b \leq -2°$	69034	71377	1778	64496	65270	65629
$Q=1$	IRAS Gaps	572	237	28	427	336	596
	$2° < b \leq 6°$	2852	1142	215	2847	2265	3368
	$0.5° < b \leq 2°$	3496	1155	220	3392	3064	3805
	$-0.5° < b \leq 0.5°$	3470	1284	175	3993	3092	4051
	$-2° < b \leq -0.5°$	2901	1485	205	3822	2999	3952
	$-6° < b \leq -2°$	3802	1424	319	3218	2547	4146
$Q=2$	IRAS Gaps	17	39	123	34	61	25
	$2° < b \leq 6°$	170	256	1352	188	188	493
	$0.5° < b \leq 2°$	131	148	983	181	190	455
	$-0.5° < b \leq 0.5°$	119	251	819	288	272	528
	$-2° < b \leq -0.5°$	105	186	1012	233	214	483
	$-6° < b \leq -2°$	98	237	1506	165	171	554
$Q=3$	IRAS Gaps	33	33	3118	87	71	67
	$2° < b \leq 6°$	240	203	30960	2032	1947	1536
	$0.5° < b \leq 2°$	414	343	22912	2077	1878	1889
	$-0.5° < b \leq 0.5°$	403	406	17038	2728	2387	2742
	$-2° < b \leq -0.5°$	271	403	22835	2433	2101	2102
	$-6° < b \leq -2°$	433	311	32119	1830	1676	1832
$Q=4$	IRAS Gaps	14	24	2955	229	219	57
	$2° < b \leq 6°$	3	6	30834	2919	2976	1051
	$0.5° < b \leq 2°$	24	13	39911	5164	5539	1919
	$-0.5° < b \leq 0.5°$	83	74	34755	7215	8194	3699
	$-2° < b \leq -0.5°$	3	122	37808	5459	5876	2149
	$-6° < b \leq -2°$	9	27	37654	3667	3712	1215

Table 9: Statistics of Variability Flags.

		B_1	B_2	A	C	D	E
$V=1$	IRAS Gaps	0	5	835	85	44	27
	$2° < b \leq 6°$	0	12	5773	865	528	230
	$0.5° < b \leq 2°$	0	9	6244	1385	870	284
	$-0.5° < b \leq 0.5°$	0	21	8996	2566	1928	662
	$-2° < b \leq -0.5°$	0	24	8863	1962	1446	412
	$-6° < b \leq -2°$	0	15	6425	995	648	264

Table 10: Statistics of Confusion Flags.

		B_1	B_2	A	C	D	E
$C=1$	IRAS Gaps	10	5	232	14	11	16
	$2° < b \leq 6°$	30	17	1898	158	150	105
	$0.5° < b \leq 2°$	54	12	1639	173	144	136
	$-0.5° < b \leq 0.5°$	52	18	2041	394	358	316
	$-2° < b \leq -0.5°$	56	15	1700	269	215	189
	$-6° < b \leq -2°$	40	12	1399	93	84	58

Table 11: Statistics of Measurement Reliability Flags.

	B_1	B_2	A	C	D	E
$R=0$	12786	9139	284614	49703	50106	37801
$R=1$	11	7	4975	777	346	748
$R=2$	26	24	2792	431	503	874
$R=3$	671	64	26398	1007	655	1137
$R=4$	8	1	91	7	17	20
$R=5$	0	0	4	0	2	0
$R=6$	6124	573	982	2695	341	2132
$R=7$	1	0	0	0	1	1
$R=8$	36	1	0	8	4	1
$R=9$	309649	319503	9456	274684	277337	286598

6 Analysis of Results

In this section we examine the accuracy and precision of the measurements in the catalog, comparing the formal, quoted errors to actual errors determined by comparing "truth" data to the measurements. This analysis has been performed for the photometric results for the Galactic plane scans since the large number of sources gives us a good statistical base. We have not provided analysis for the IRAS Gap sources. In part, this is because there is little "truth" data available for sources in the IRAS Gap regions. However, we have no reason to expect the photometric accuracy to be different than those sources in the Galactic plane scans. We also examined the astrometric accuracy of the catalog. In this case, because the scan patterns are quite different, the Galactic Plane survey and the IRAS Gap survey are treated independently.

6.1 Photometric Accuracy

6.1.1 Calibration Stars

As discussed in Section 4.3.2, the on-orbit calibration of the SPIRIT III sensor and CONVERT process was measured against truth values provided by the Cohen-Walker-Witteborn (CWW) spectral templates for certain stars. The complete CWW database currently consists of 422 templates, 3 composite spectra, and 12 model spectra (Cohen et al. 1999). To establish the accuracy of the irradiance extracted by the Celestial Automated Processing we have identified 12 CWW template stars in the Galactic plane survey data. Figures 5-10 plot the measured in-band irradiance versus the in-band irradiance value predicted by convolving the CWW spectrum over the Relative-Spectral-Response (RSR) for each SPIRIT III band. The error bars are $\pm 1\sigma$ flux uncertainties for the measured irradiances, and the calculated model uncertainties for the CWW template in-band irradiance calculations. Flux density units (Jy) are shown on the top and right-hand axes.

The black symbols represent those stars found in quadrants I and IV of the Milky Way, while stars located in the anti-center direction (quadrants II and III) are shown in blue. This breakdown also shows the behavior of the calibration over time (and hence focal plane temperature) since the anti-center was surveyed after the center region, generally at higher focal plane temperatures.

Because they must be well studied, photometrically and spectroscopically, calibration star tend to be bright. This is especially true in high density regions, and we see that the stars from quadrants I and IV are brighter than those from quadrants II and III. In Band A (and to a lesser extent D) they are bright enough that this set of stars does not fully probe the calibration over the full dynamic range of the SPIRIT III instrument. This is most severe in Band A, where we have two decades of irradiance (to 10^{-18} W cm^{-2}) unprobed. To test the lower decades of flux calibration in Band A, and to improve the statistics for all bands, Cohen & Hammersley (1999) have extended the above results to 16 Cohen et al. (1998) template stars, plus 103 Hipparcos stars represented by Kurucz (1991) models. The Hipparcos stars were used as part of the calibration of ISO. Their results are listed in Table 12. Note that, although a very wide variety of spectral types was used to support ISO's requirements, we do not believe that any supergiants should be utilized for radiometric checks because of the possibility that these will have stellar winds with free-free emission over and above their photospheric radiation (if of types B, A, F, or G), and/or emission by warm circumstellar dust (if of types K or M). Both these processes can fill in photospheric absorption features, such as the CO fundamental that is sampled by Bands B_1 and B_2, and such stars were explicitly excluded from these radiometric checks.

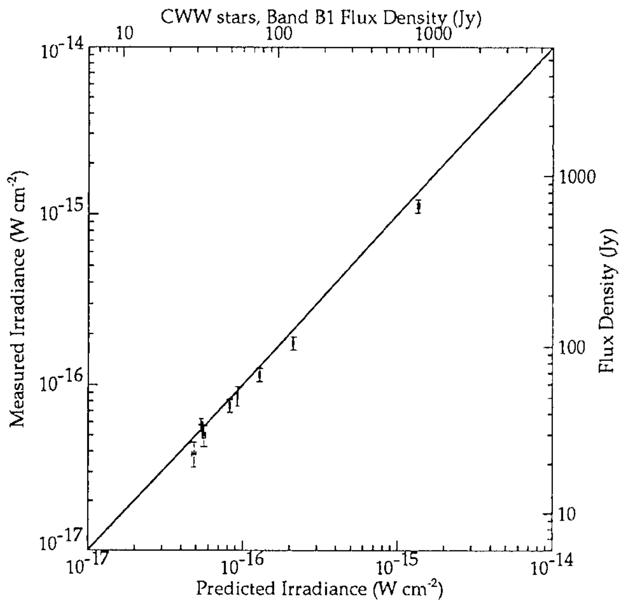

Figure 5: Band B_1 calibration stars.

Table 12: MSX PSC calibration results.

Band	N_{stars}	$L_{\min}$ $(W\ cm^{-2})$	$L_{\max}$ $(W\ cm^{-2})$	$\left\langle \frac{\text{Measured Irradiance}}{\text{Predicted Irradiance}} \right\rangle$	Total Error
B_1	40	1.60×10^{-17}	1.5×10^{-15}	0.92	± 0.02
B_2	45	1.67×10^{-17}	2.2×10^{-15}	0.95	± 0.02
A	107	2.0×10^{-18}	4.1×10^{-15}	1.00	± 0.01
C	55	2.8×10^{-18}	4.8×10^{-16}	0.99	± 0.01
D	56	1.7×10^{-18}	2.9×10^{-16}	0.99	± 0.01
E	15	1.3×10^{-17}	1.8×10^{-16}	1.07	± 0.025

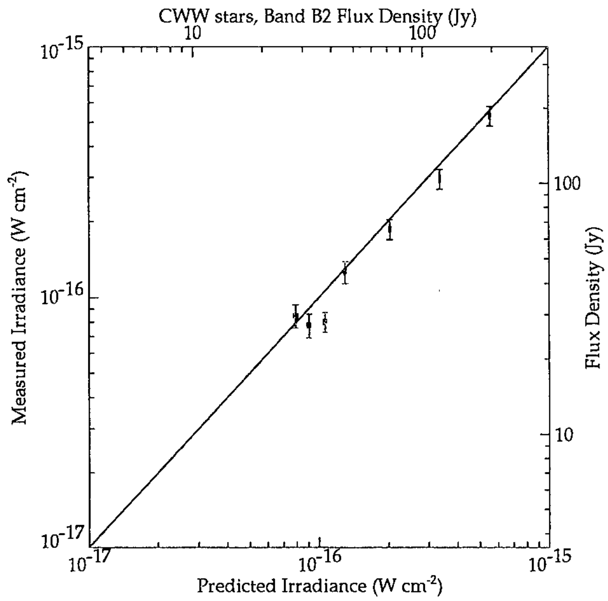

Figure 6: Band B_2 calibration stars.

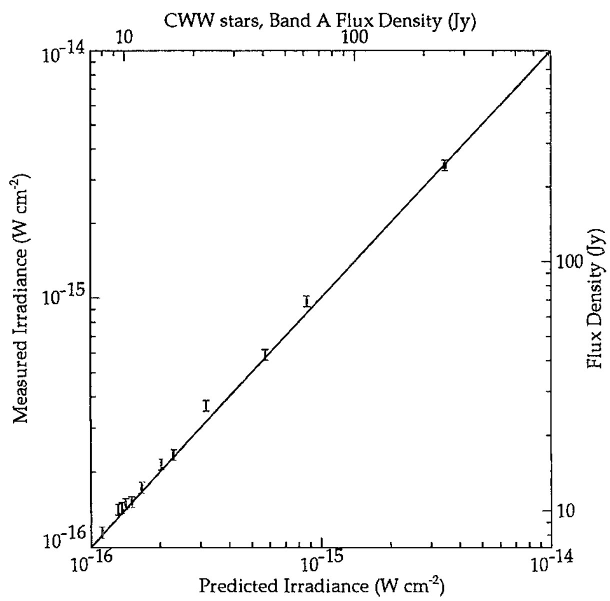

Figure 7: Band A calibration stars.

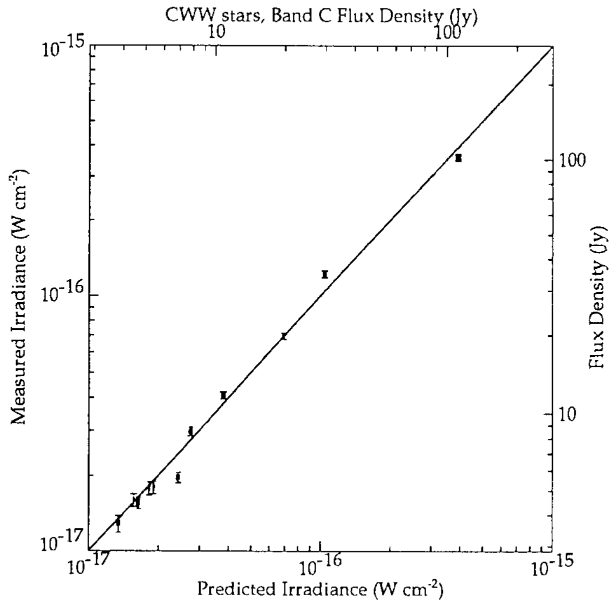

Figure 8: Band C calibration stars.

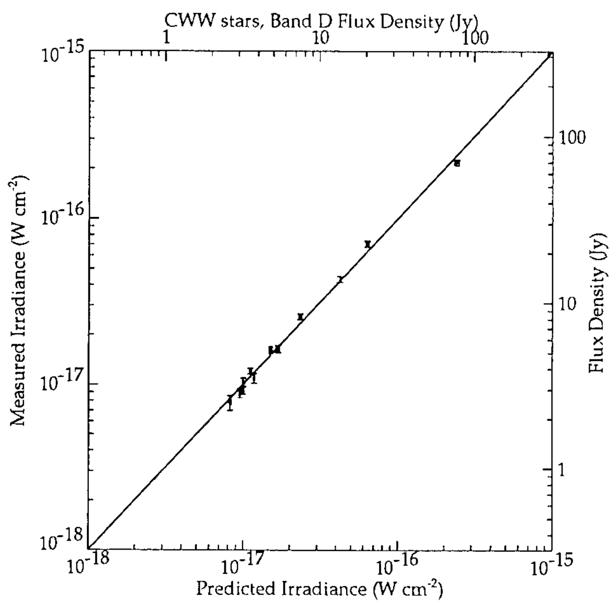

Figure 9: Band D calibration stars.

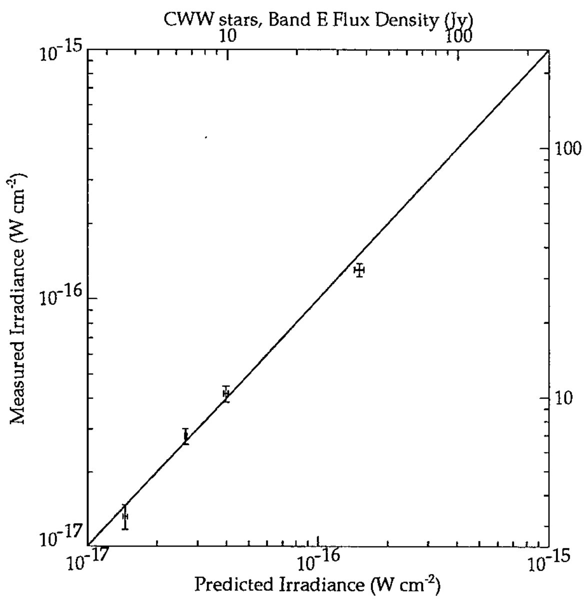

Figure 10: Band E calibration stars.

6.1.2 Galactic Plane Survey

Quoted Uncertainties - The quoted errors for the flux densities in the MSX survey are the RSS of the formal extraction error and the irradiance uncertainties as determined by the DCATT. The DCATT error is fixed for each band, while the formal extraction error is essentially a function of the SNR of the source weighted by the number of times it was observed. For each band we have shown (Figures 11 - 16) the distribution of the quoted uncertainties, as well as the distribution of uncertainty broken down by flux quality flag.

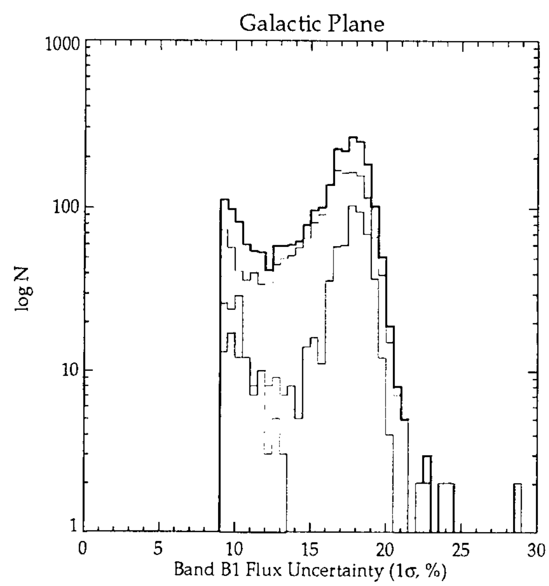

Figure 11: Quoted 1σ uncertainties in Band B_1 flux density.

Again, totals are shown in black, while the colored lines represent measurements with different flux quality flags. Measurements of the highest quality, $Q_a = 4$, are shown in green, moderate quality $Q_a = 3$, are in red, and the blue line shows measurements of low quality, $Q_a = 2$. In all bands, the $Q_a = 4$ sources have the lowest uncertainties, as they should since they are high SNR and have the maximum number of sightings. Thus, the uncertainties are also reduced by the statistics of weighted averaging. The moderate quality fluxes generally show a bi-modal distribution with peaks at the DCATT uncertainty floor, and another just beyond the limiting uncertainty of the $Q_a = 4$ sources. The first peak is composed of high SNR sources which were not sighted in four scans. The second peak is primarily composed of lower SNR sources. The poor quality sources ($Q_a = 2$, in blue) also show this type of behavior, although in some cases (Bands C, D, and E) the low uncertainty peak is simply an extended tail on the high uncertainty distribution. Since the measurements in this category represent the lowest SNR sources and those of high SNR but only a single sighting, the fact that the high uncertainty peak contains the majority of the sources is an expected result.

IRAS based flux comparisons: The combination of CWW calibration stars and templates do an excellent job of establishing the calibration of the brighter sources (to SNRs of about 70 in Band A). In order to test the photometric accuracy of the entire range of fluxes in the catalog, we are forced to take a less

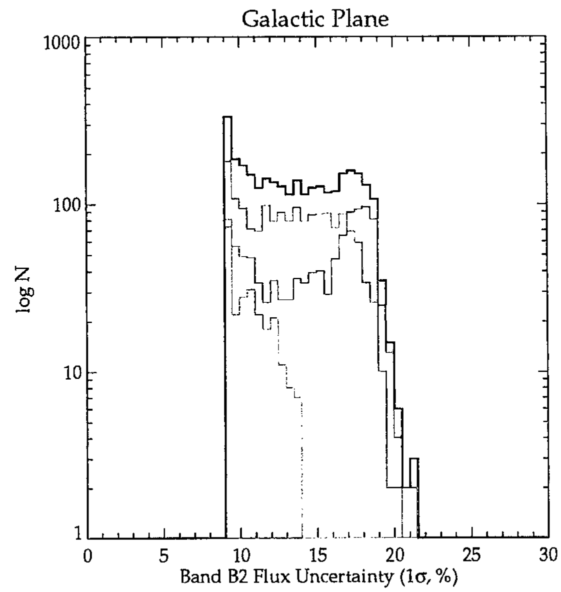

Figure 12: Quoted 1σ uncertainties in Band B_2 flux density.

precise and more statistical approach. To this end, we shall use as truth data the predicted MSX in-band irradiances calculated for the MSX Infrared Astrometric Catalog (Egan & Price 1996).

For this comparison, we put a premium on the confidence in our predicted fluxes. To ensure that we are using the most accurate flux predictions, we require the sources in this comparison to satisfy these criteria: 1) the measured source position must be within 3 arcsec of the astrometric position; 2) the astrometric star must have an IRAS PSC or FSC measurement; 3) be an M-type star. The last criterion is included because the prediction method of Egan & Price assumes a Planckian source function. We find that M-type stars (with little or no circumstellar dust) best conform to this model, and therefore will have the most accurate predicted fluxes.

Figures 17 through 22 show the measured *vs.* predicted irradiances for each MSX band for the Galactic plane scans. The error bars are the 1σ quoted errors for the measured irradiances, and an error bar of 14% for the predicted value. The 14% value represents the RSS value of the 1σ errors of the IRAS measurements (~10% in the $12\mu m$ band according to the IRAS Explanatory Supplement) and an estimate of the error inherent in estimating the spectral shape from the spectral type information (assumed to be 10%). The symbols are color coded according to the value of the flux quality flag. The color codes are listed in Table 13.

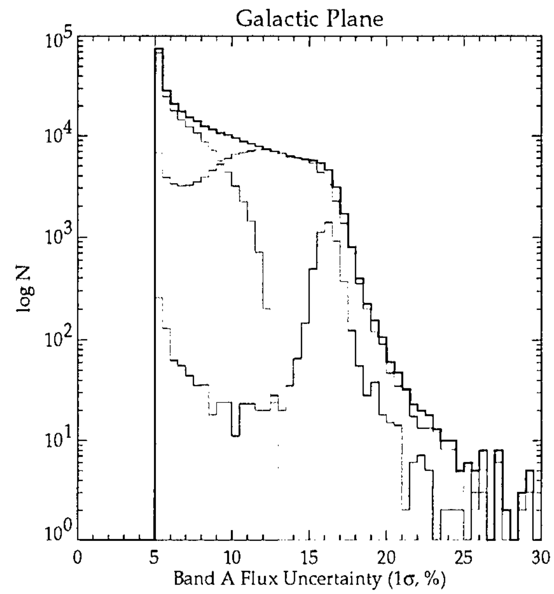

Figure 13: Quoted 1σ uncertainties in Band A flux density.

Table 13: Color code of Flux Quality flag.

Flux Quality Flag, Q_a	Symbol or Line Color
4	Green
3	Red
2	Blue
1	Cyan

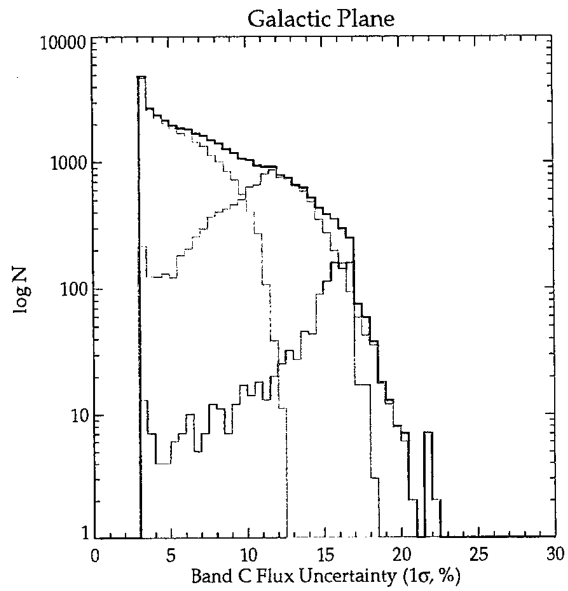

Figure 14: Quoted 1σ uncertainties in Band C flux density.

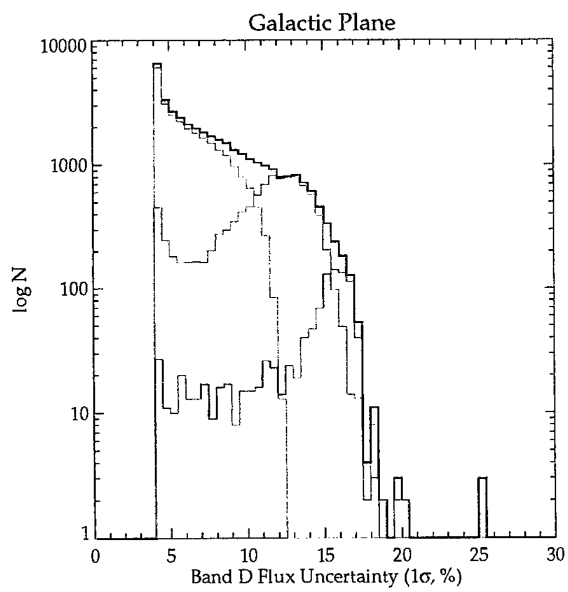

Figure 15: Quoted 1σ uncertainties in Band D flux density.

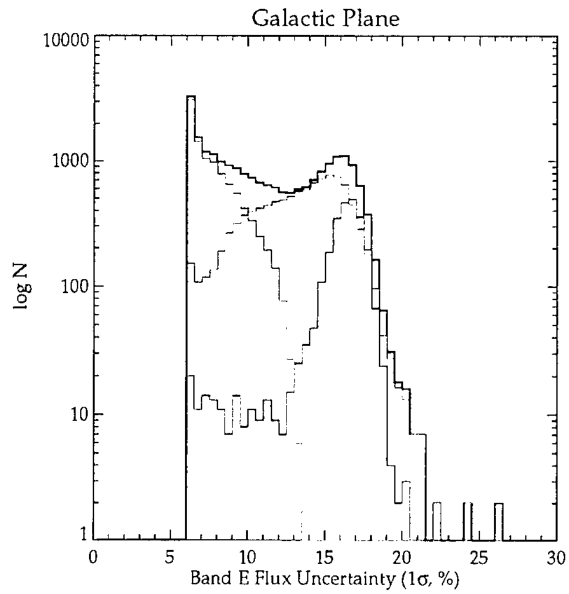

Figure 16: Quoted 1σ uncertainties in Band E flux density.

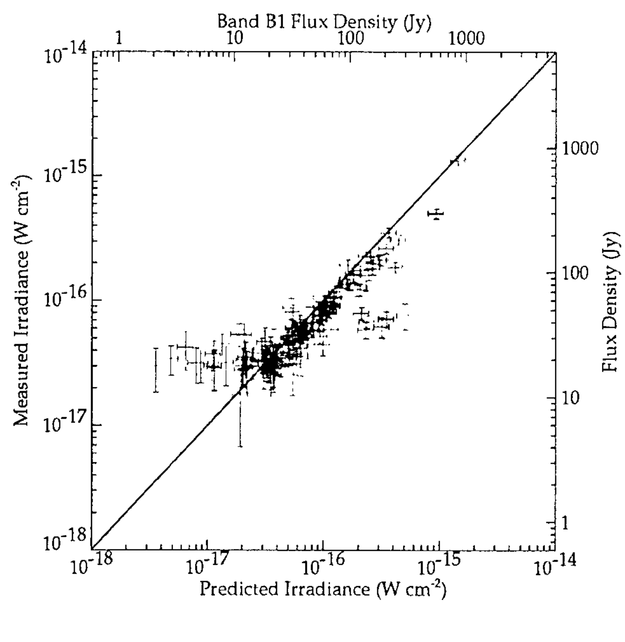

Figure 17: Band B_1 measurements versus IRAS based predicted fluxes.

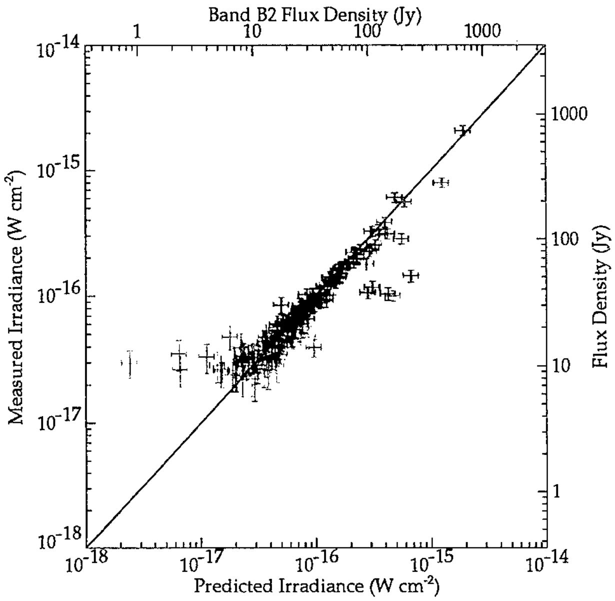

Figure 18: Band B_2 measurements versus IRAS based predicted fluxes.

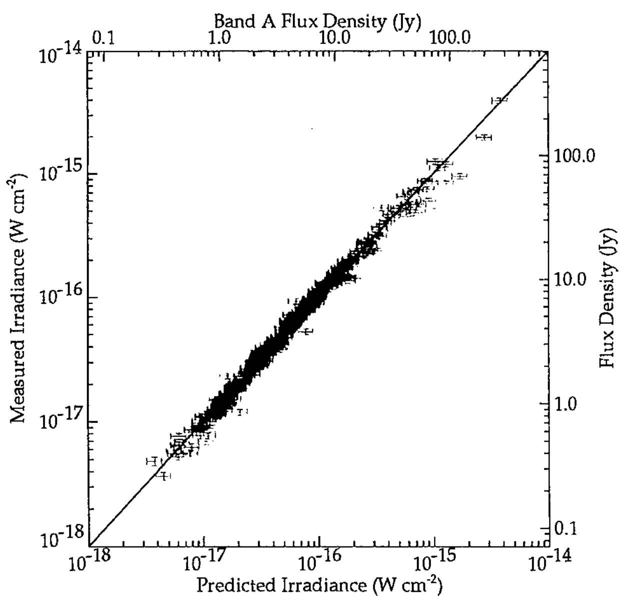

Figure 19: Band A measurements versus IRAS based predicted fluxes.

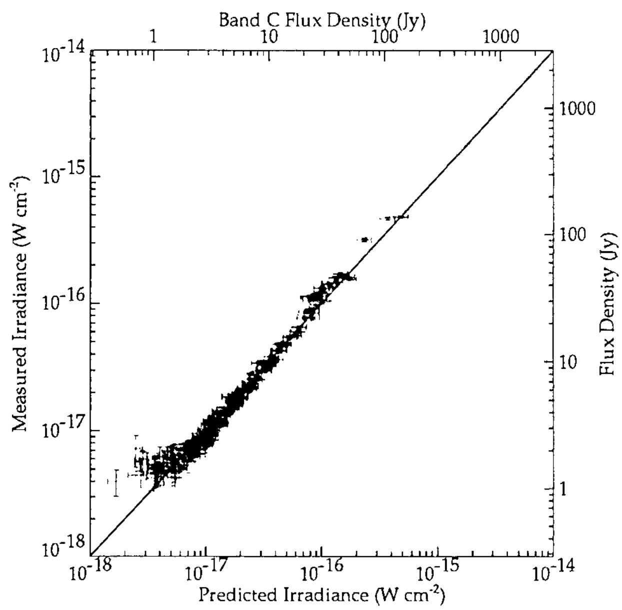

Figure 20: Band C measurements versus IRAS based predicted fluxes.

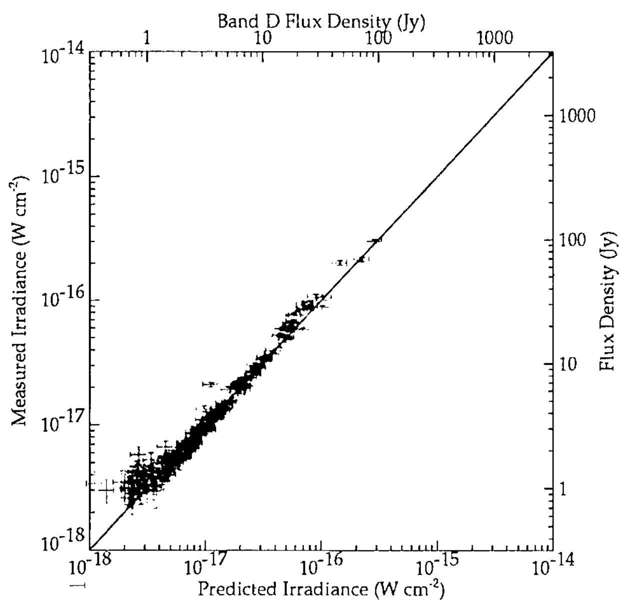

Figure 21: Band D measurements versus IRAS based predicted fluxes.

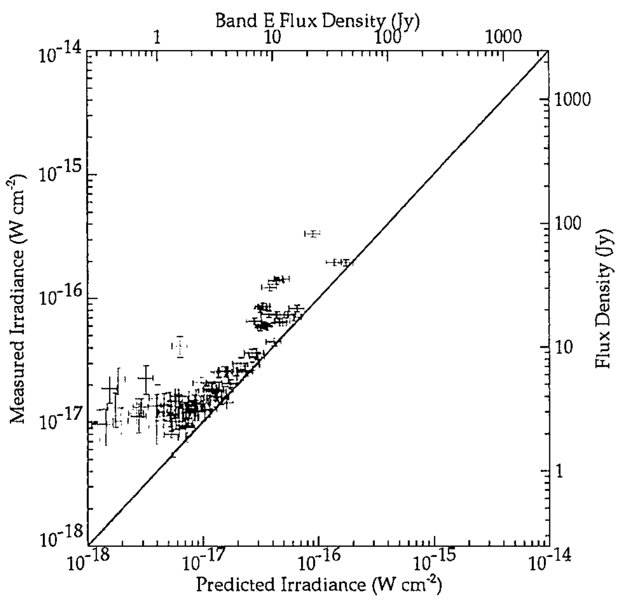

Figure 22: Band E measurements versus IRAS based predicted fluxes.

6.2 Positional Accuracy

The positional uncertainties (in-scan and cross-scan) quoted in the catalog are the RSS of the uncertainties inherent in the point source extraction procedure and the uncertainty in the spacecraft attitude determination remaining after the boresight refinement procedure has been applied. Expressed mathematically, this is

$$\sigma = \sqrt{\sigma_{pos}^2 + \sigma_{BPR}^2}. \tag{35}$$

For a given scan, the uncertainty in the BPR results are generally $\sim 3''$. The source extraction procedure is able to fix the position of the peak of the PSF in focal plane coordinates within about 0.1 pixel, or $\sim 1.8''$ for both in-scan and cross-scan. Therefore, the positional accuracy of the catalog is driven by the uncertainty in global spacecraft attitude. For those areas of the sky for which we have quadruply redundant scans, we expect to gain a factor of two improvement in the positional uncertainty. Given that in-scan and cross-scan uncertainties for a single scan are typically $\sim 4''$, this translates to an expected final uncertainty in the catalog of $\sim 2''$ in each direction. Below we shall examine the statistics of the quoted positional uncertainties for the Galactic plane and the IRAS Gap catalogs, and probe the true positional accuracy of the catalog by comparing the catalog stars to positions of some of the stars to their positions from astrometric catalogs.

6.2.1 The Galactic Plane

Quoted Uncertainties - The quoted 1σ uncertainty in in-scan and cross-scan position is shown in Figures 23 and 24 respectively. The black line shows the distribution of uncertainties for the 312,498 sources with Band A flux qualities of $Q_A \geqslant 2$. These have been further broken down by Q_A. As above green denotes $Q_A = 4$, red denotes $Q_A = 3$, and blue denotes $Q_A = 2$. Because the flux quality flag is in large part based on the number of scans in which the source was detected, the higher quality flux measurements also have less uncertainty in their position determination. The mean values of each of these distributions can be found in Table 14.

Measured Position Accuracy - The quoted position uncertainties are derived from statistical errors associated with the point source extraction process and the boresight pointing refinement. Done properly, these numbers should accurately reflect the trustworthiness of the quoted position. To test our results, we have cross referenced the MSX PSC to the MSX Infrared Astrometric Catalog (Egan & Price 1996), using a Band A flux matching criteria to confirm positional associations. In the Galactic plane, we have identified 3,740 MSX PSC stars which fell within a radius of 30 arcseconds of the astrometric star position and had $0.85 \leq F_{measured}/F_{predicted} \leq 1.18$. The in-scan and cross-scan component of the position differences were computed. The results are shown in Figure 25, where the in-scan distribution of error (truth position − MSX PSC position) is shown in red, and the cross-scan distribution is in blue. We fit a Gaussian model to each distribution. The parameters of each are listed in Table 14. The σ values of the models are quite similar to the mean measured uncertainties. As was found in the measured uncertainties, the in-scan error is larger than the cross-scan error.

6.2.2 Areas Missed by IRAS

We examine the position accuracies of the IRAS Gap stars independently from the Galactic plane stars because of the possibility that the difference in scan pattern could have introduced a different character to the in-scan and cross-scan error behavior. We find that this is not the case, and that the positional errors (both quoted uncertainty and actual error) of the IRAS Gap sources are consistent with the Galactic plane data.

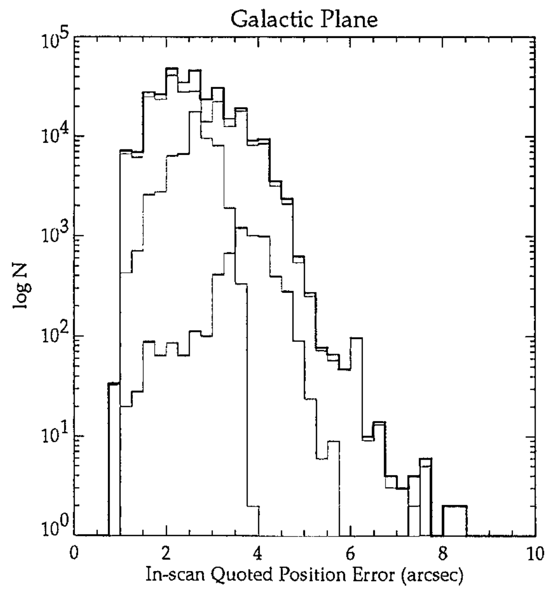

Figure 23: Quoted in-scan position uncertainties (1σ) of the Galactic plane sources.

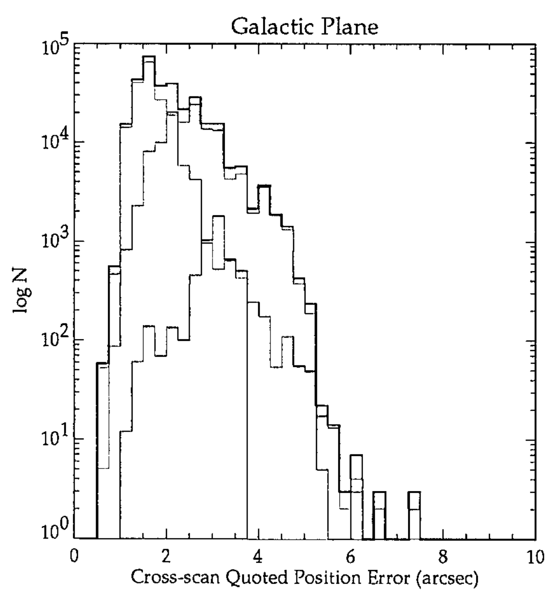

Figure 24: Quoted cross-scan position uncertainties (1σ) of the Galactic plane sources.

Table 14: MSX PSC positional uncertainties.

	σ_{FIT}	$\langle\sigma_{\mathrm{quoted}}\rangle(Q_A \geq 2)$	$\langle\sigma_{\mathrm{quoted}}\rangle\ (Q_A = 4)$	$\langle\sigma_{\mathrm{quoted}}\rangle\ (Q_A = 3)$	$\langle\sigma_{\mathrm{quoted}}\rangle\ (Q_A = 2)$
G.P. in-scan	2.26″	2.57″	2.15″	3.12″	3.68″
G.P. cross-scan	1.93″	2.06″	1.66″	2.59″	3.12″
I.G. in-scan	2.13″	2.57″	2.26″	2.83″	3.62″
I.G. cross-scan	1.87″	1.79″	1.46″	2.07″	2.73″

Quoted Uncertainties - The quoted 1σ uncertainties in in-scan and cross-scan positions are shown in Figures 26 and 27, respectively. The black line shows the distribution of uncertainties for the 6,196 sources with $Q_A \geqslant 2$. As for the Galactic plane figures, green denotes $Q_A = 4$, red denotes $Q_A = 3$, and blue denotes $Q_A = 2$. The mean values of each of these distributions are listed in Table 14.

Measured Position Accuracy - Cross referencing of the MSX PSC to the MSX Infrared Astrometric Catalog using the matching and confirmation criteria described above finds 1053 stars in the IRAS gaps. As for the Galactic plane stars, the in-scan and cross-scan component of the position differences were computed. The results are shown in Figure 28, where the in-scan distribution of error (truth − measured) is shown in red, and the cross-scan distribution is in blue. A Gaussian model fits each distribution. The width parameter of each model is listed in Table 14. The σ values of the models are quite similar to the mean measured uncertainties in in-scan and cross-scan. As was found in the measured uncertainties, the in-scan error is larger than the cross-scan error. Comparing the reported catalog positions to the astrometric positions from the MSX IR Astrometric Catalog, we see that both the in-scan and cross-scan error distributions are very close to Gaussian.

7 Reliability and Completeness

For version 1.2 of the MSX Point Source Catalog, our discussion of reliability and completeness shall center on an examination of the differential source counts in various regions of the Galactic plane and in each of the IRAS gaps. We have examined a few selected areas of the plane in a more rigorous manner using the deep CB03 raster scans and by doing some comparisons to ISOGAL (Pérault *et al.,* 1996) fields. We will use these results in support of the conclusions drawn from the differential source counts. However, a more complete analysis shall not be completed until the production of Version 2.0 of the catalog.

Figures 29 - 38 in this section show plots of the differential source counts ($d \log N/dS$) as a function of source strength (S = Flux density in Jy) for ten different areas. We have separately plotted the source counts for each IRAS gap, and each octant of the galaxy. Each figure contains a subplot for each of the six MSX photometric bands.

The completeness of the catalog is driven by the sensitivity of the 8.3 μm band (A) since it is $\geq$10 times more sensitive than the other bands. This is reflected in relative numbers of sources with source quality flags = 1 in the various bands. The criteria for keeping a source in the catalog were such that the sources with Band A limits ($Q_A = 1$) were minimized. Such sources are usually HII regions which are very strong at long wavelengths, but at the detection limits in Band A. The majority of sources are only detected in Band A. A large number of them were detected only at the lower limit threshold (and only in the most sensitive scans) of the other bands. However, the Band A detection confirms that the source is in fact real. This accounts for the large number of $Q = 1$ sources in the other bands.

A related issue that must be noted is the flux overestimation problem for low SNR sources. This effect

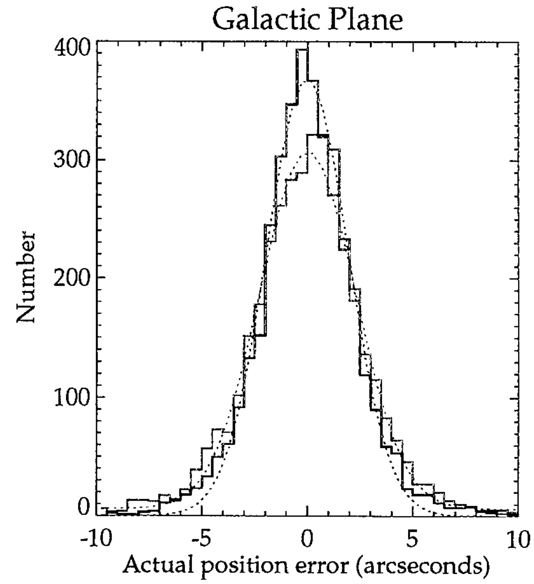

Figure 25: Position error (truth – measured) distribution of Galactic plane sources.

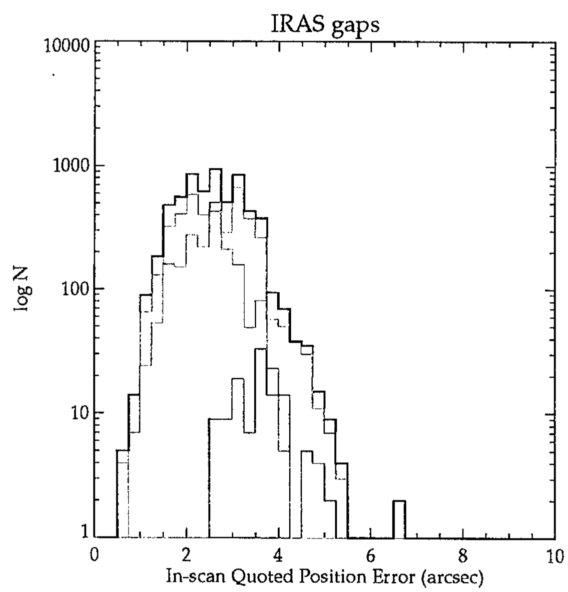

Figure 26: Quoted in-scan position uncertainties (1σ) of the IRAS Gap sources.

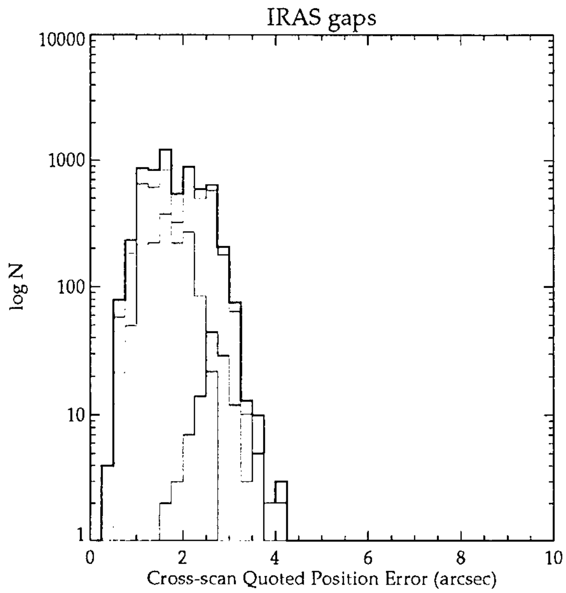

Figure 27: Quoted cross-scan position uncertainties (1σ) of the IRAS Gap sources.

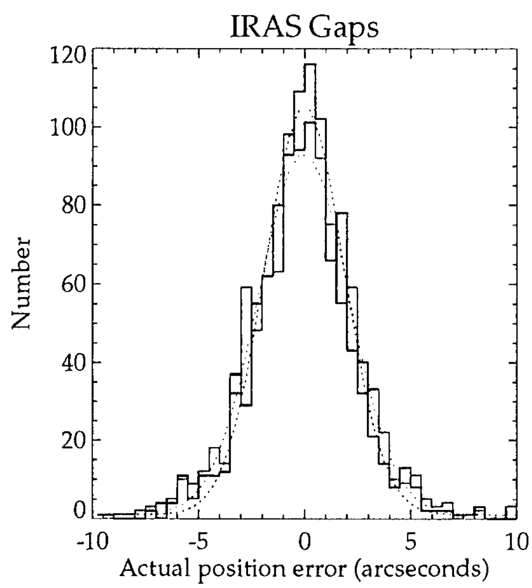

Figure 28: Position error (truth − measured) distribution of IRAS Gap sources.

is discussed in some detail in the IRAS Faint Source Survey Explanatory Supplement (Moshir et al. 1992). Briefly stated, the effect is caused by noise in the measurements enhancing the apparent SNR of a source. For example, if an source of true SNR 2.8 is enhanced by noise, to an apparent SNR of 3.1, it will be included in the catalog, while if it is not enhanced it does not meet the threshold for inclusion in the catalog. We have not applied a correction for this flux overestimation bias in the catalog. The primary concern to the user should be in determining source colors when using a high SNR Band A source and a low SNR source from one of the other bands.

7.1 Band A

For Band A, the turnover in differential source counts occurs at 100 mJy, except for the octants covering the ninety degrees about the Galactic center. Here the source counts turn over at 200 mJy. Away from the center octants, the slope of the differential source counts in the plane also appear to be consistent with the -1 value expected for an evenly distributed disk. The IRAS Gap source counts also appear to be consistent with expectations. The double peak in the Gap 1 source counts is likely due to the change in scan rate and integration mode implemented toward the end of the mission when higher focal plane temperatures degraded the sensistivity of the normal scan mode.

The decline of the of the source count slope below ~7 Jy for $|l| < 45°$ has (at least) two contributing factors. First, there is the unexpected discovery of mid-infrared extinction clouds (Perault et al., 1996, Egan et al. 1998). The MSX survey indicates that in the inner two octants, and within $|b| < 1°$ these infrared dark clouds can reduce the Band A star counts by ~10%. The second factor is source confusion. The source candidate finding algorithm used in this version of the MSX PSC could find a maximum of about 500 sources per square degree. The number density of sources within $|l| < 45°$ which are above the MSX sensitivity limit in Band A is much higher than 500 per square degree. In these octants, especially near the plane, the catalog completeness is limited by the source detection limits imposed in the software. These constraints, imposed because of the problems with the DAF pointing errors, will be resolved in version 2 of the MSX PSC. We expect to be able to detect ≥ 1000 sources per square degree in the version 2.

At this point we have examined the completeness and reliability for four areas, all near the plane. We have used the DAOPHOT (Stetson 1987) package to extract sources from one of the MSX deep raster scan co-adds. These images are sensitive to point sources above 20 mJy in the absence of confusion. We have compared these sources to the sources extracted from a single long survey scan at $l = 30°, b = 1°$. We find that requiring 2 detections out of 4 scans should give us a catalog which is >95% complete above 0.25 Jy, and 50% complete at 0.1 Jy in Band A. Further, for a single scan, there were no false detections above 0.16 Jy, indicating that the catalog is >99% reliable above this flux limit.

These conclusions are confirmed by our comparisons of catalog sources to sources in three ISOGAL fields near the Galactic Center (Omont & Ganesh private communication 1999). These fields, taken with ISOCAM in the LW2 ($\sim 7\ \mu m$) and LW3 ($\sim 15\ \mu m$) filter bands, were centered on: $l = 0.0°$, $b = 1.0°$; $l = 1.03°$, $b = -3.83°$; and $l = 1.37°$, $b = -2.63°$. The raster scan ISOCAM images each covered $15' \times 15'$ fields-of-view. These fields all reach the MSX PSC source density limit of 500 sources per square degree. While a direct comparison of magnitudes is not possible, given the different wavelength coverages of the MSX and ISOCAM filters, we can estimate the completeness of the MSX PSC from this comparison. First, we note that every MSX PSC source within the ISOCAM fields has a counterpart of comparable magnitude in the ISOCAM field. This implies that no spurious sources have been created in the MSX PSC processing. The larger pixel size of MSX/SPIRIT III with respect to ISOCAM is apparent in the fact that a few of the MSX PSC sources are resolved into multiple objects by the ISOCAM image. Comparing the source counts as a function of brightness, the MSX PSC v1.2 appears to be complete (in these fields) above 0.2 Jy in Band

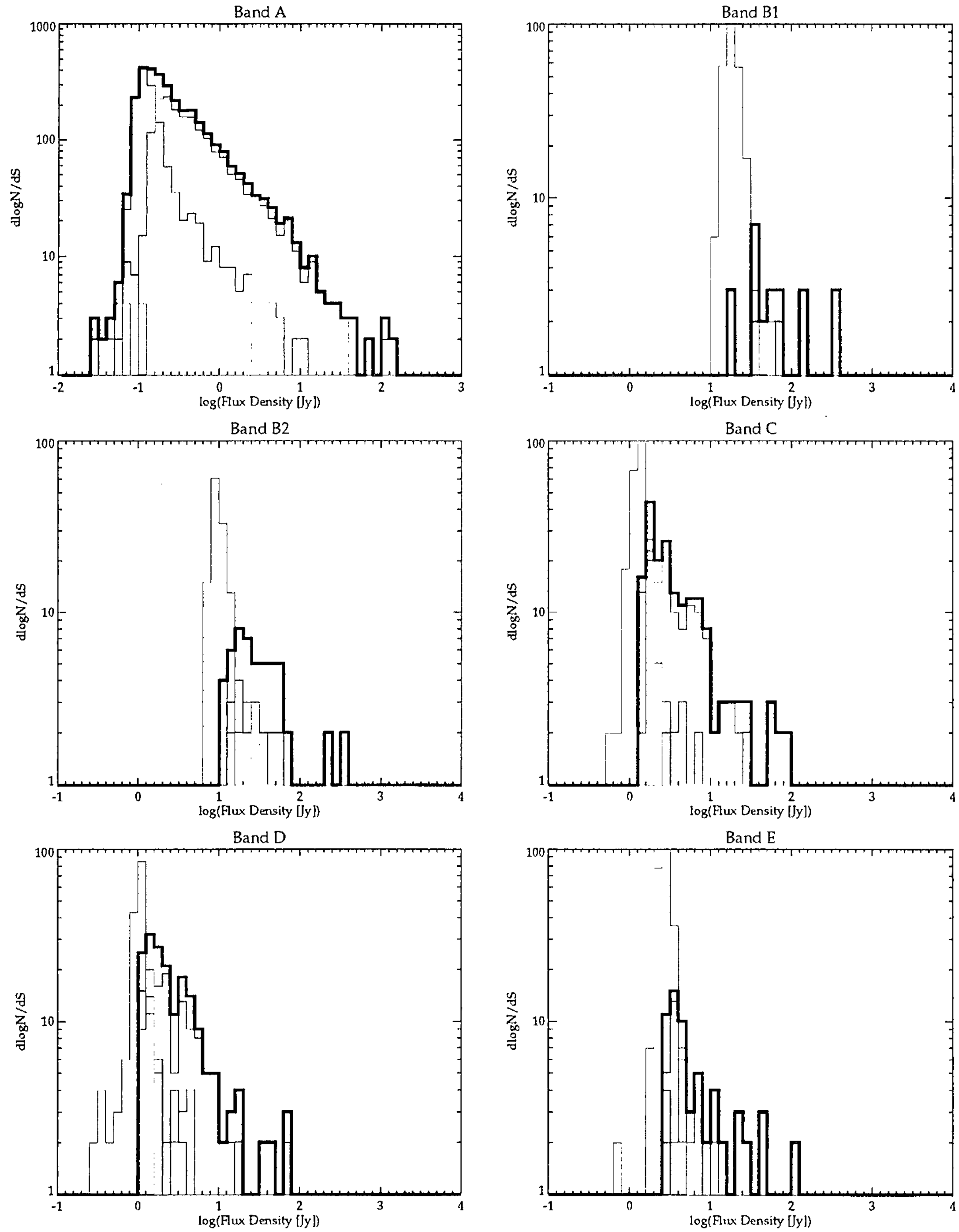

Figure 29: MSX PSC source counts, IRAS Gap 2.

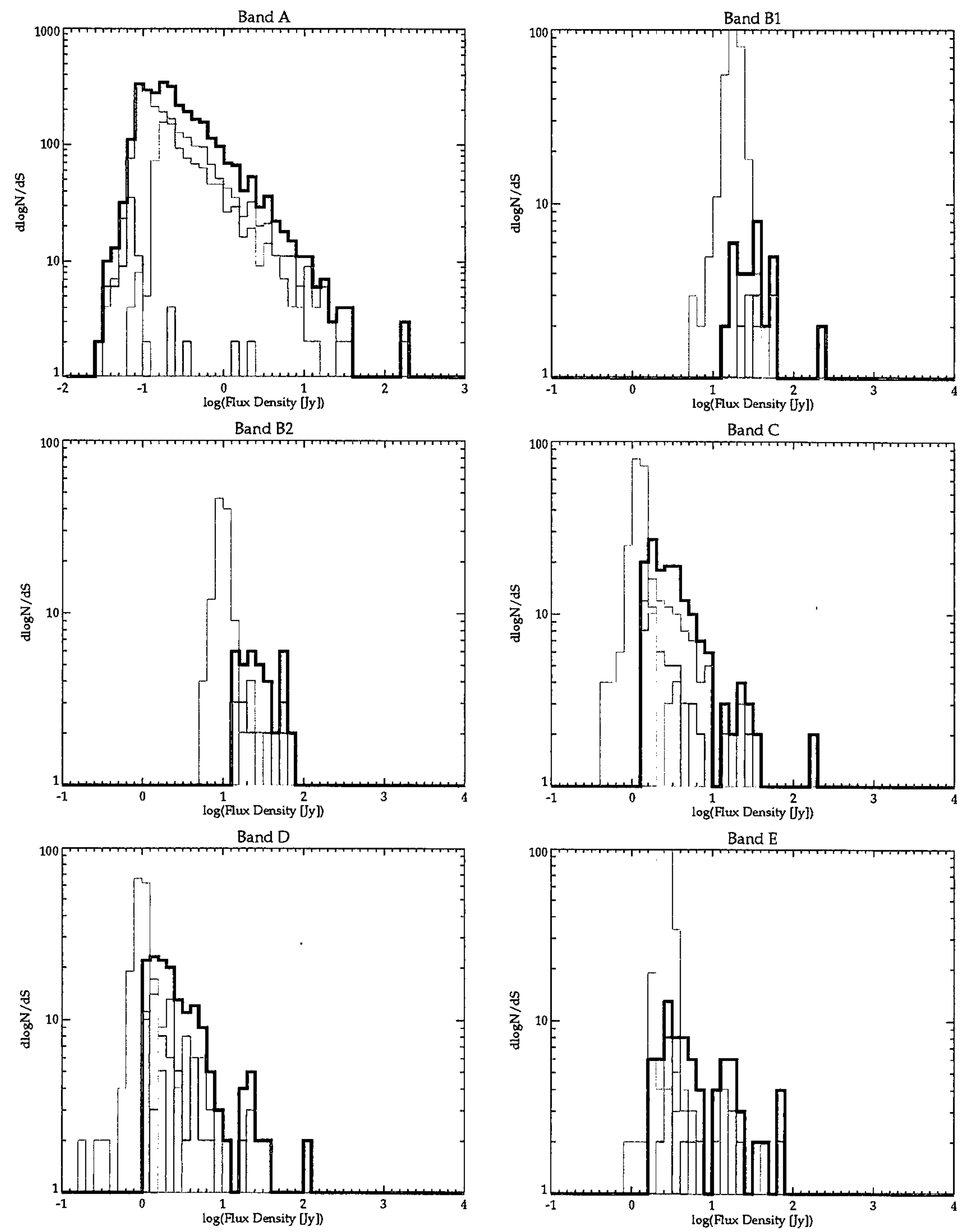

Figure 30: MSX PSC source counts, IRAS Gap 1.

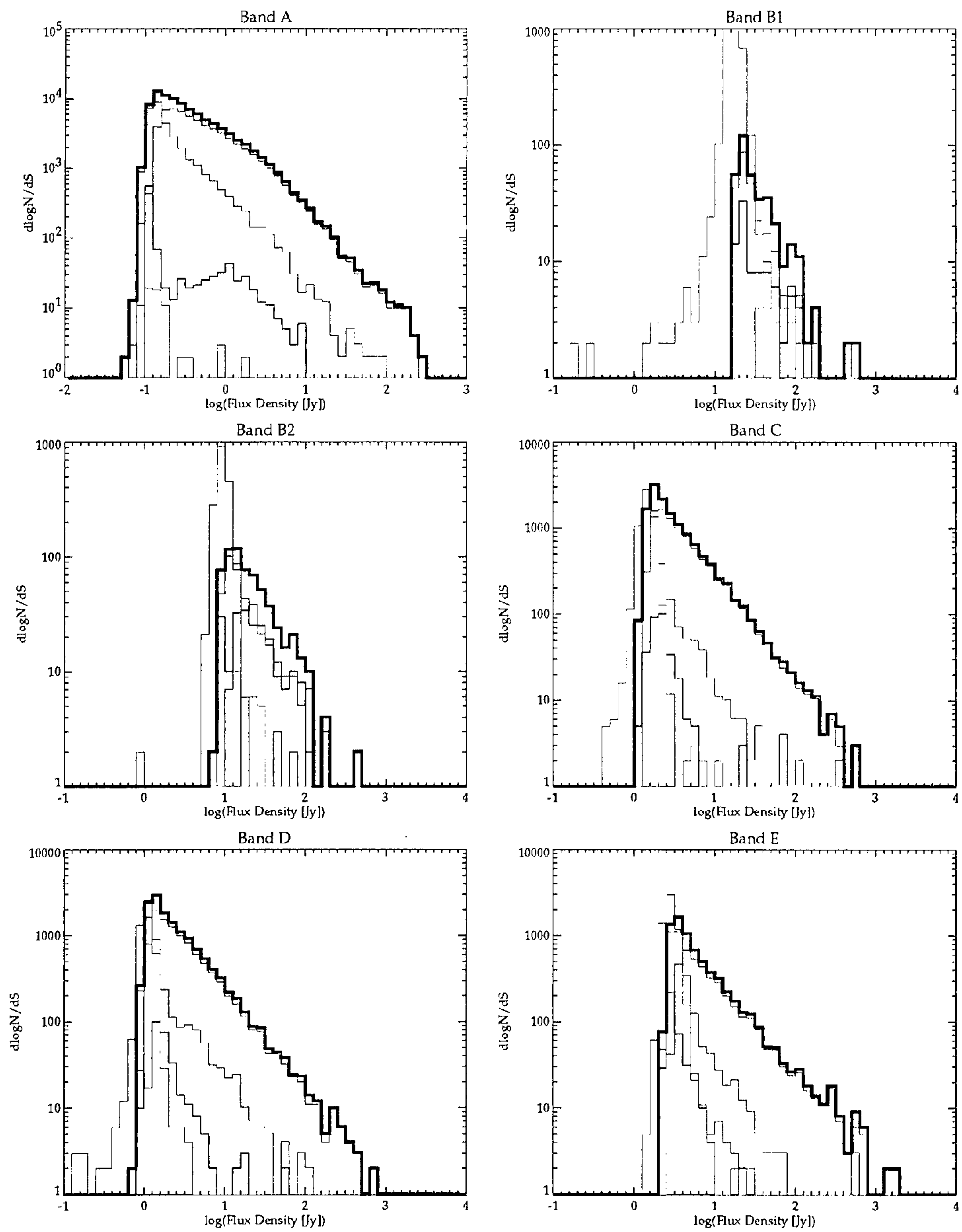

Figure 31: MSX PSC source counts, $0 < l \leq 45$.

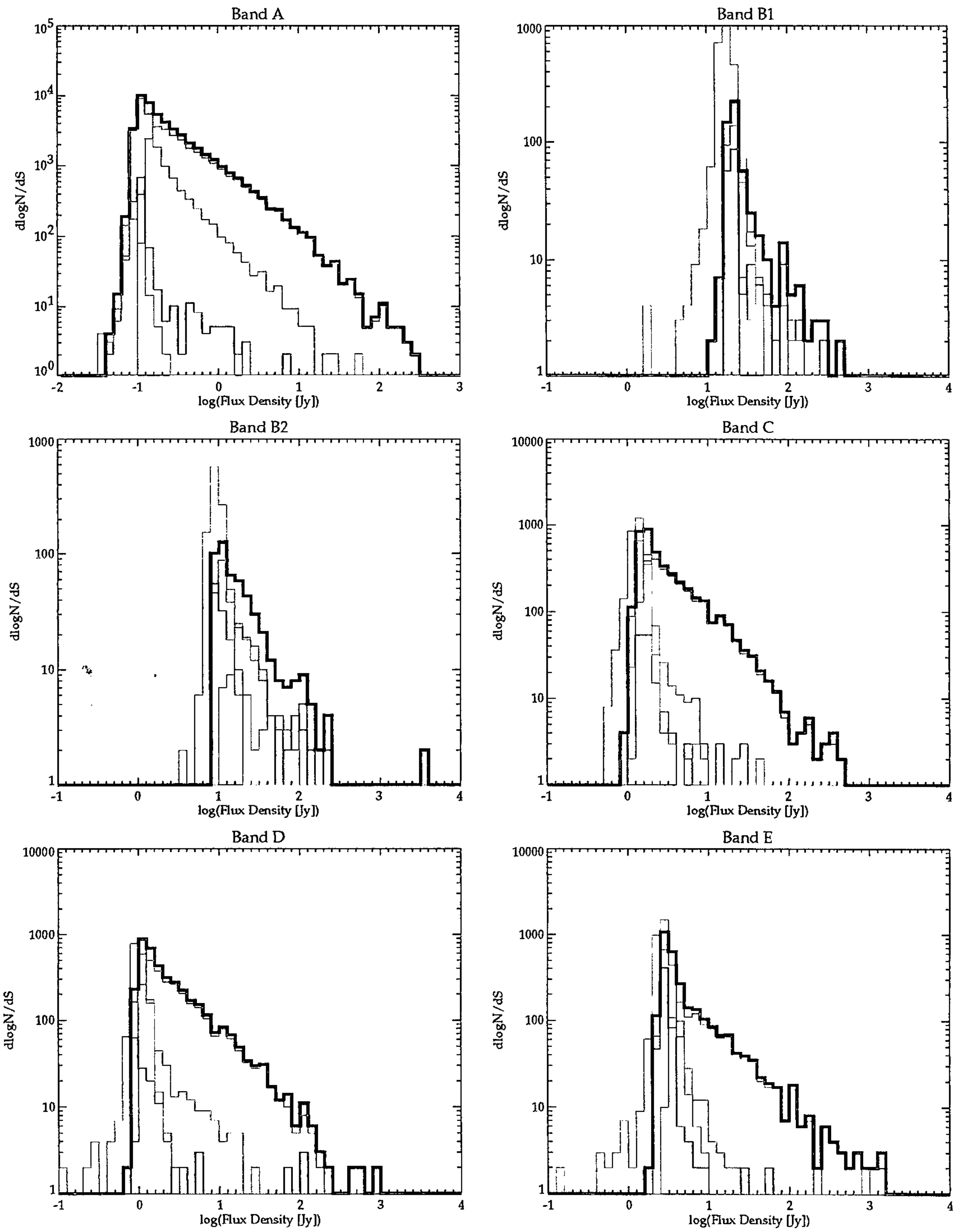

Figure 32: MSX PSC source counts, $45 < l \leq 90$.

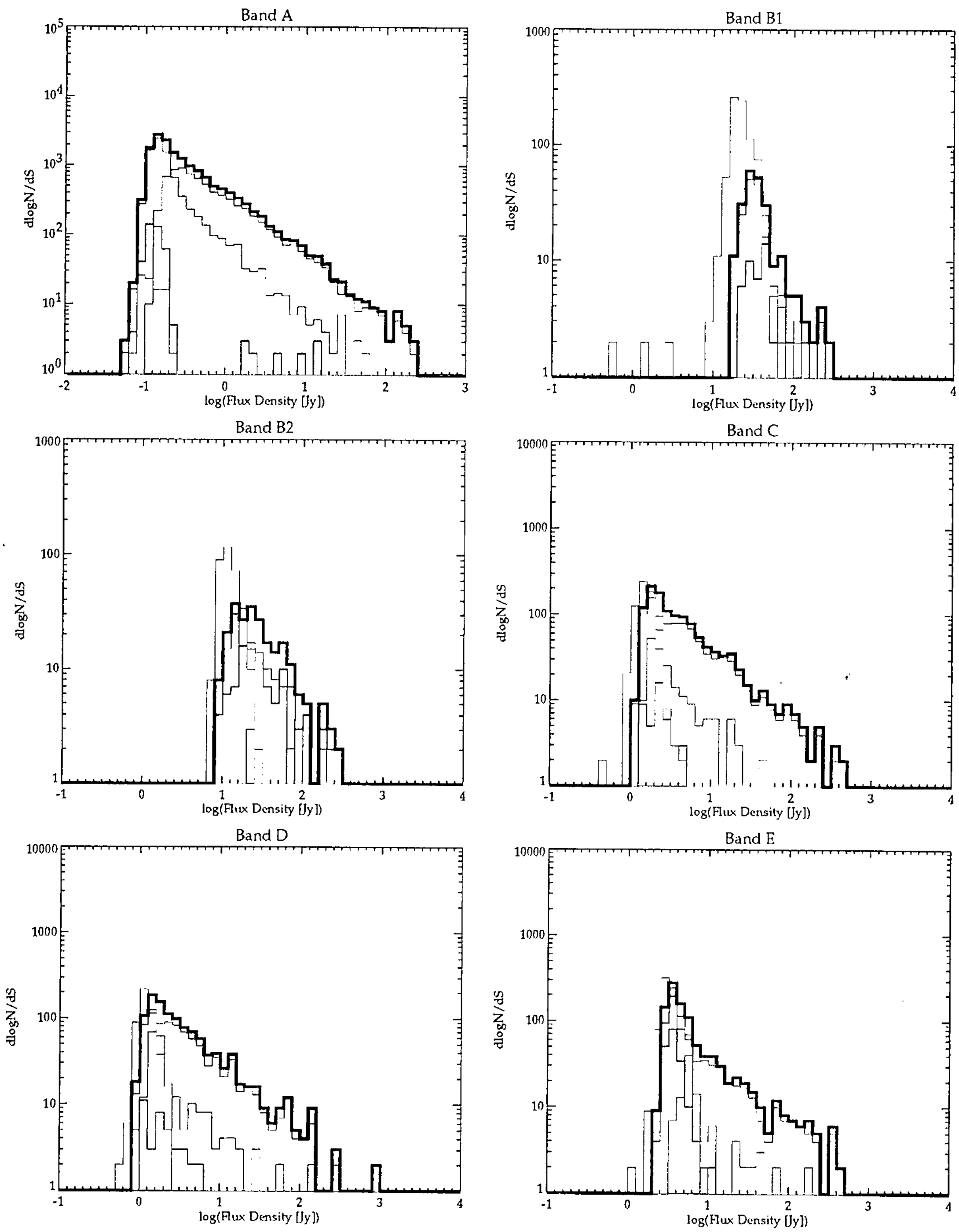

Figure 33: MSX PSC source counts, $90 < l \leq 135$.

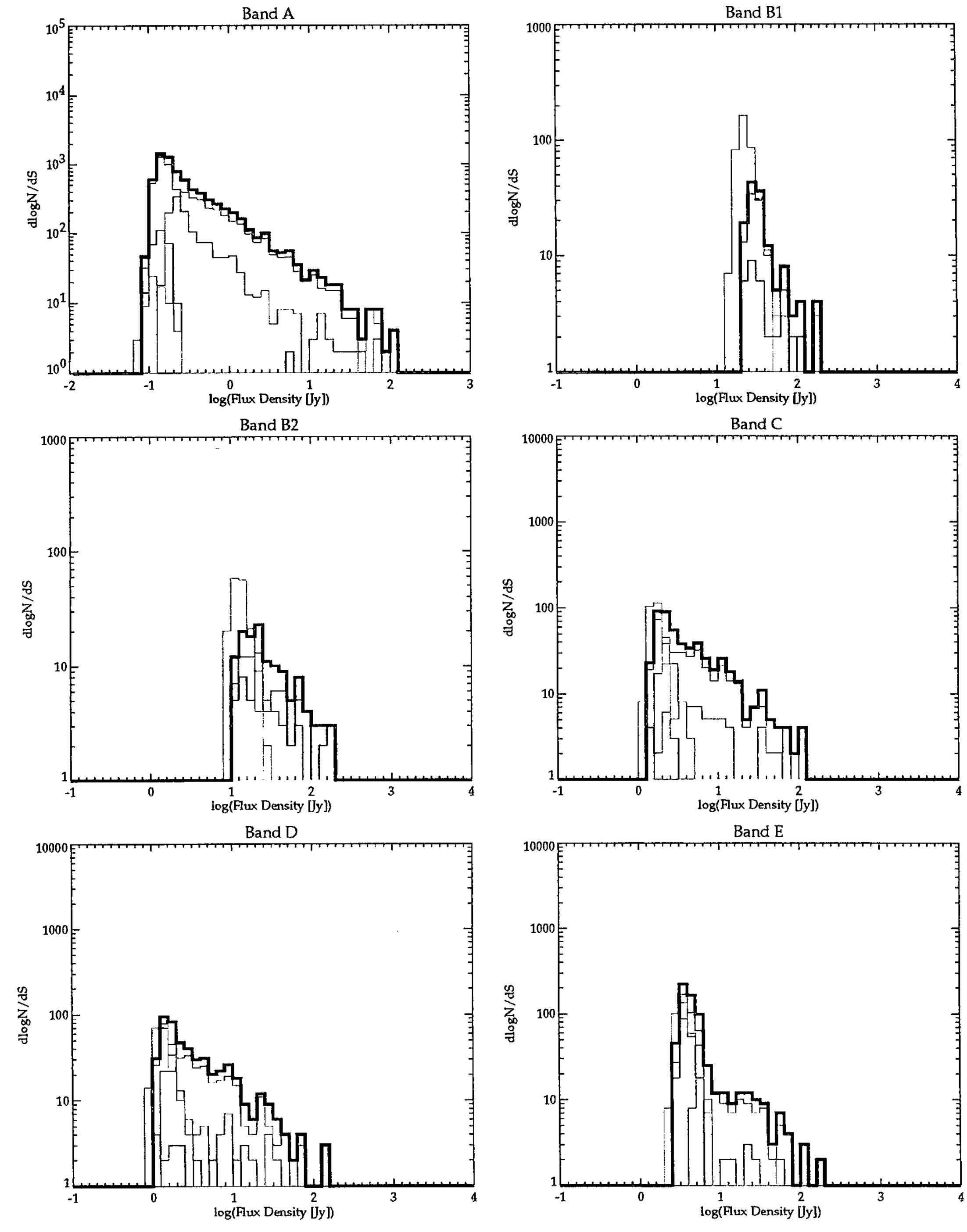

Figure 34: MSX PSC source counts, $135 < l \leq 180$.

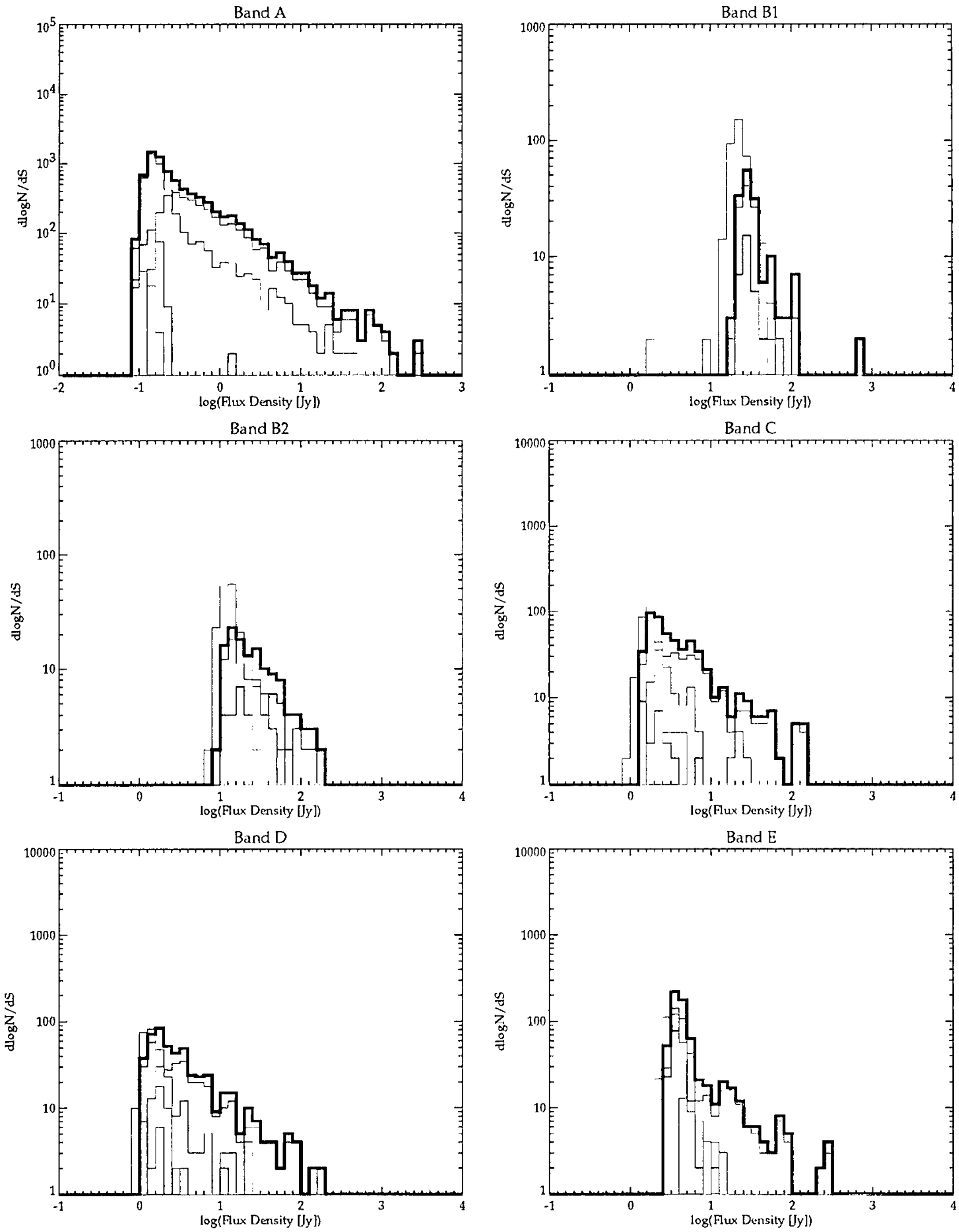

Figure 35: MSX PSC source counts, $180 < l \leq 225$.

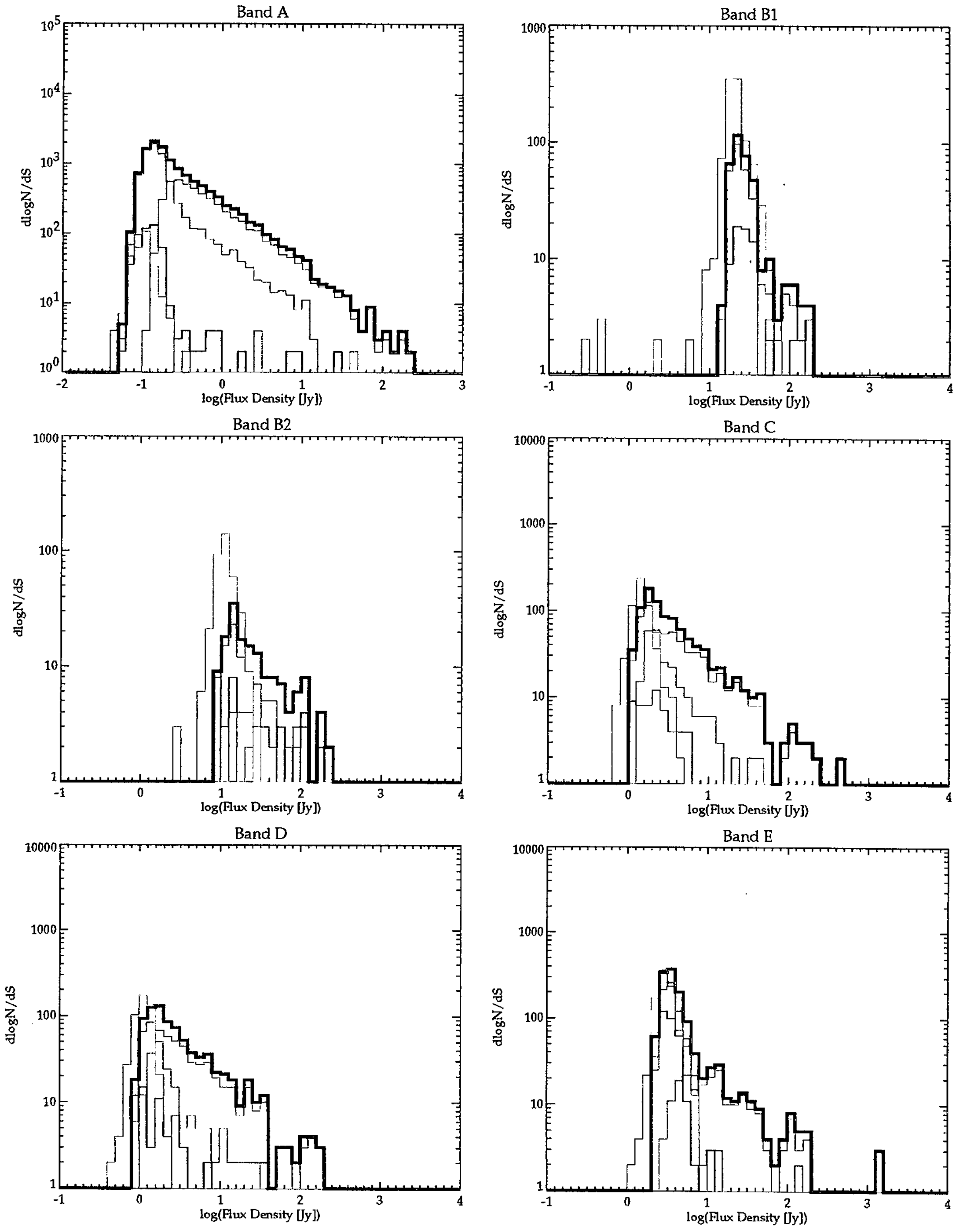

Figure 36: MSX PSC source counts, $225 < l \leq 270$.

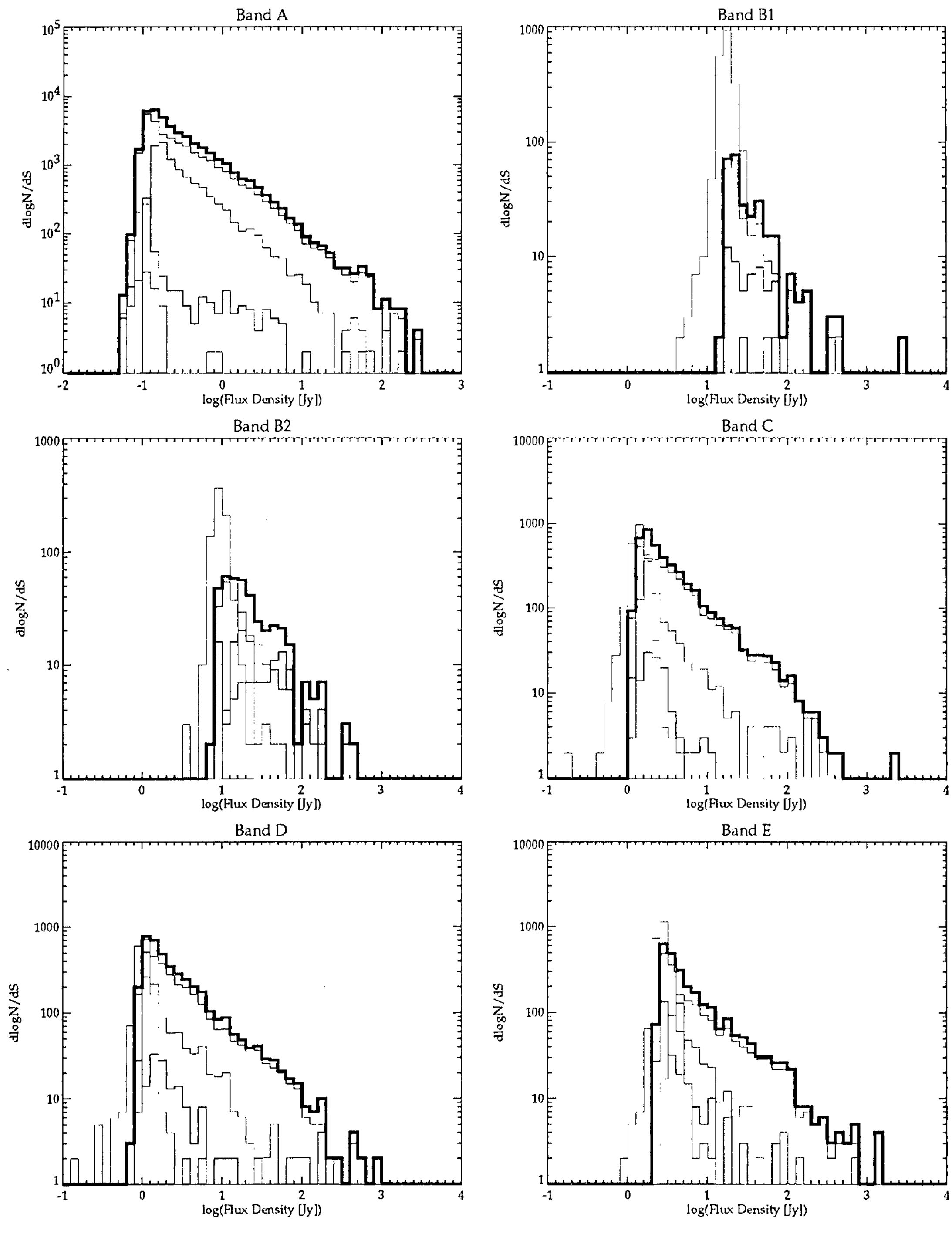

Figure 37: MSX PSC source counts, $270 < l \leq 315$.

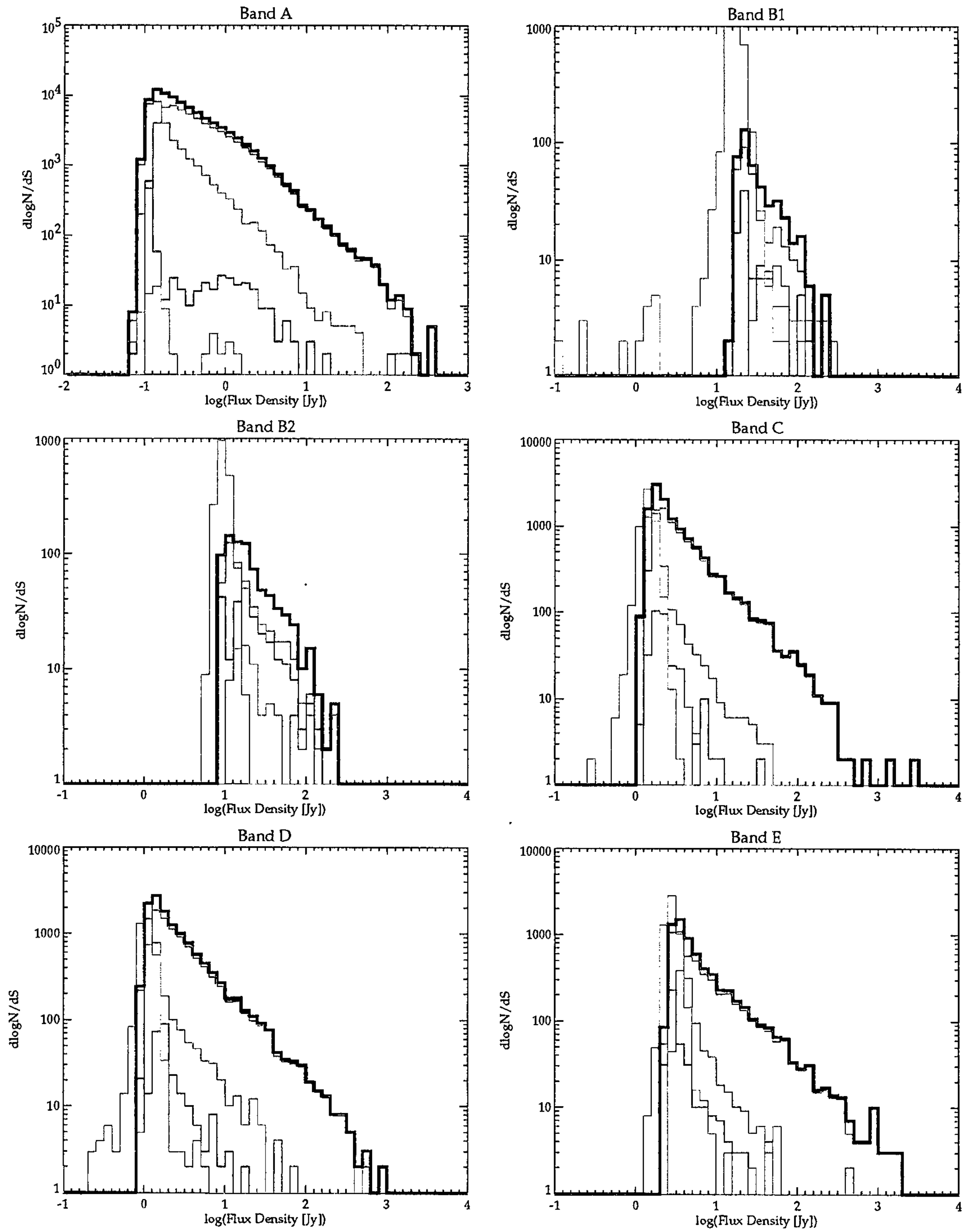

Figure 38: MSX PSC source counts, $315 < l \leq 360$.

A, and about 50% complete at a flux of 0.17 Jy. The faintest MSX source observed in these fields is 0.12 Jy. These numbers are consistent with the expectations for completeness and reliability derived statistically from the comparison the the CB03 raster scan, and with the source count behavior shown in Figures 31 and 38.

7.2 Bands B_1 and B_2

The short wavelength B bands are the least sensitive of the MSX Infrared bands, with detection sensitivities (for at least $Q = 2$ detections) of approximately 15 Jy in Band B_1 and 8 Jy in Band B_2. The differential source counts turn over in Band B_1 at about 22 Jy, indicating that we can expect the catalog to be reasonably complete above this level. The turnover occurs at ~14 Jy in Band B_2.

One of the factors to consider when using the B band data are that the survey is by definition less complete in these bands, given the split nature of the focal plane. The survey plan yields a 2× survey in these bands, rather than a 4× survey as in the other bands. Given the definition used for the flux quality flag, we end up with many good measurements tagged as upper limits in Bands B_1 and B_2.

7.3 Band C

The C band has 4 active columns, two on each side of the stagger line. The C array had the poorest noise characteristics, including a number of artifacts which were uncorrected for the processing done for Version 1 of the MSX PSC. The turnover in the early part of the mission occurs at ~1.6 Jy, and at ~2 Jy late in the mission. The distribution of sources with flux limits ($Q = 1$) in Band C peaks at 1.4 Jy, and in the Galactic plane scans appears to be consistent with the slope of the distribution at higher source strengths. This implies that for most sources in the Galactic plane catalog, the $Q = 1$ flux density values in Band C will be fairly good representations of the true Band C flux density. This is confirmed by Figure 20, where in most of the $Q = 1$ sources, the quoted flux densities are within the quoted error tolerances of the "truth". In the IRAS Gaps, however, there is a large excess of $Q = 1$ sources. These are likely due to the increased coverage in the middle and ends of the IRAS-like scan pattern. There is up to six-fold redundance in the center of the IRAS Gap scans. At the scan ends, where all of the scans converge, the coverage can be >20× over a given area. In these locations, we are much more likely to see a spurious detection at a given location once in six or twenty scans than once in four scans. Further, because Gap 1 was observed later in the mission when the noise was higher, the likelihood of having spurious detections increases. This explains the large numbers of "detection limit" measurements in the B, C, D, and E bands in the IRAS Gaps. While one should only use any of the $Q = 1$ flux density values with great caution, remember that these are least reliable in the IRAS Gap catalog.

7.4 Band D

Another 4-column detector array, the D band has slightly better noise characteristics than Band C, and therefore slightly better performance. From the figures, one finds that the differential source counts begin turnover at ~1 Jy for the early scans and ~1.5 Jy in the later scans. As is expected the shapes of the source count curves for Bands C and D are quite similar, including the details of the behavior of the $Q = 1$ source counts.

7.5 Band E

A 2-column array, the E band is less sensitive than the C and D bands. The 2-column structure also makes detector dropouts a bigger problem, increasing the likeliehood that a real source will not be detected in a given scan. This accounts for the larger number of $Q = 1$ sources in this band. In the early part of the mission (quadrants I and IV), the turnover in source counts occurs at ~2.5 Jy. For the later scans (quadrants II and III, the IRAS Gaps) the turnover has moved to ~3.5 Jy. Also noticeable is an upturn in the slope of the distribution at ~5 Jy. This is especially apparent in the later scans, probably because of the smaller numbers of real sources in the anti-center and gaps. This is most likely due to selection biases at the low SNR levels. In Band E this bias is a more severe problem than in Bands C and D.

8 Final Notes to the User

8.1 Caveats

8.1.1 Artifacts Near Bright Sources

The SPIRIT III instrument suffered from internal glints from the brightest IR sources, notably in the cross-scan direction. Typically these are not point-like and should have been removed by the cascade-average filtering process. However, it is possible that these glints may cause spurious companions to very bright ($\geq$ a few hundred Jy) sources.

8.1.2 Emission Ridge Line Sources

The Band A images show that within $\pm1.5°$ of the Galactic equator, the background is dominated by bright, highly structured diffuse emission. To the point source extractor, knots in this emission may appear to be point-like. In some areas, notably the Cygnus region, we often see point sources in a line along a ridge of emission. Whether there are actually embedded objects in these knots is not known.

8.1.3 Sources Near the North Ecliptic Pole

The IRAS Gap scans cover an ecliptic latitude range from $-65° \leq \beta \leq 90°$. Due to the coordinate degeneracy near the North Ecliptic Pole (NEP), nearly all of the scans overlap at this point. A total of fifty scans cover the NEP. This results in a breakdown of the source acceptance criteria defined in Table 5, which have been optimized for the maximum of 6 coverages in the center of the main scan region. Requiring only 3 sightings near the pole results in many false detections. To avoid reliability problems near the NEP, Version 1.2 of the MSX PSC has rejected sources for which $\beta \geq 75°$, the Band A flux density is less than 0.14 Jy, and the number of total DCEs the source is sighted in is less than 8.

This does throw out a number of real sources, along with a much greater proportion of spurious sources. **Even so, the user should still treat faint sources with few sightings near the NEP with some skepticism.**

8.2 Planned Updates

At the present writing, we plan to begin reprocessing of the data for version 2 of the MSX PSC in late 1999 for release in late 2000 to early 2001. Version 2 will take advantage in improvements in calibration, and pointing, as well as refinements of the algorithm based on what has been learned about the data from the processing and validation of MSX PSC Version 1.

8.2.1 Global Minimization/CONVERT 6 Processing

Version 2 of the MSX PSC will be processed with CONVERT 6 and the final Instrument Product Files. The significant changes in CONVERT 6 from 5.2 concern the processing of interferometer data. Some minor changes to the software to process the radiometer data corrects problems that rejected small blocks of data. We will also process the data with some of the default rejection options turned off. For example, currently data following saturation is rejected owing to the inability to accurately quantify the subsequent change in dark current for the saturated pixel during calibration. Not only has the Celestial Background processing team estimated and corrected the effects, this problem is removed by the cascade-average filtering.

As described in Section 4.2.2, calibration was based on ground based measurements scaled to on orbit values of observations of α Boo. The other calibration stars and the reference spheres were used to assess the accuracy of the calibration. Thus, the bias term was introduced into the uncertainty calculation. The global calibration includes all the calibration measurements, thereby eliminating the bias term. Although not pertinent for the MSX PSC, the global calibration also eliminates the Unprobed Uncertainties in the radiance error. The global calibration clearly shows that the photometric error is related to temperature and this dependence is incorporated in the error terms.

The new calibration will also fix the difficulties seen in the Bands B and E calibration. The irradiance error associated with the calibration should also be reduced from the CONVERT 5 values. In addition to the improvement in the calibration, the Celestial Backgrounds analysis team has better characterized the instrument noise and dark current behavior. These changes will be used as additional (non-DPC) inputs to CONVERT 6.

8.2.2 Pointing Refinement

Version 2 of the MSX PSC will have significantly improved positions. The nominal fifth order polynomial used to update the boresight of the long scans has been replaced with a cubic spline with knots spaced 7°to 10°apart, on the average. This alone has improved the position errors up to a factor of two. On the average the area density of astrometric stars is 1 to 1.5 per square degree; this number applies to a linear degree of scan since the focal planes are ˜1°across. We will use multiply observed stars in the MSX PSC to cross-tie the astrometric observations from the different scans. This should improve the positions another 20%. We anticipate meeting or exceeding the pointing requirement of a half cone angle of 1.8″.

8.2.3 PSC Algorithm Updates

The major PSC algorithm update will improve the local maximum finding routine used to find point source candidates. MSX PSC Version 1 proved to be deficient in regions of high source density, limiting the source density extracted to a maximum of 500 sources per square degree. Even in regions of lower source density, it was found that the fainter of a stellar pair can be missed if they were too close together. Tests of the new method indicate that we should be able to achieve source extractions of more than 800 sources per square degree in Version 2 of the MSX PSC.

A SPIRIT III RELATIVE SPECTRAL RESPONSE

This appendix begins on page 65.

B SPIRIT III EFFECTIVE WAVELENGTH TABLES

This appendix begins on page 87.

C SPIRIT III PHOTOMETRIC CONVERSIONS

This appendix begins on page 95.

D SPIRIT III COLOR CORRECTION TABLES

This appendix begins on page 111.

References

[1] Burdick, S.V. and Morris, D. C. 1997, Optical Engineering, 36, 2971

[2] Cohen, M., Walker, R.G., Barlow, M.J. and Deacon, J.R. 1992, AJ, 104, 1650

[3] Cohen, M., Walker, R.G., Carter, B., Hammersley, P., Kidger, M. and Noguchi, K. 1999, AJ, 117, 1864

[4] Cohen, M. and Hammersley, P. 1999 in preperation

[5] Egan, M. P. & Price, S.D., 1996, AJ, 112, 2862

[6] Egan, M. P., Shipman, R. F., Price, S. D., Carey, S. J., Clark, F. O., & Cohen, M. 1998, ApJ, 494, L199

[7] Gezari, D.Y., Schmitz, M., Pitts, P.S., and Mead, J.M. 1993, *Catalog of Infrared Observations, 3rd Ed.* (NASA:Washington DC)

[8] Hindsley, R.B, and Harrington, R.S., 1994, AJ, 107, 280

[9] Kurucz, R. L. 1991 in "Stellar Atmospheres - Beyond Classical Models" (Knudsen)

[10] Mill, J. M., O'Neil, R., Price, S. D., Romick, G., Uy, M., & Gaposchkin, E. M. 1994, J. Spacecraft & Rockets, 31, 900

[11] Moshir, M., et al. 1992, IRAS Faint Source Survey Explanatory Supplement Version 2 (IPAC:Pasadena)

[12] Perault, M., Omont, A.,Simon, G., Seguin, P., Ojha, D., Blommaert, J., Felli, M., Gilmore, G., Guglielmo, F., Habing, H., Price, S.D., Robin, A., de Batz, B., Cesarsky, C., Elbaz, D., Epchtein, N., Fouque, P., Guest, S., Levine, D., Pollock, A., Prusti, T., Siebenmorgen, R., Testi, L. and Tiphene, D. 1996 A&A, 315, L165

[13] Pratt, W.K., Cooper, T.J., and Kabir, I. 1984, "Pseudomedian Filter" in *Proc. SPIE Conf.*, Los Angeles, CA, January 1984

[14] Pratt, W.K. 1991, *Digital Image Processing, Second Edition,* (Wiley-Interscience:New York)

[15] Press, W.H., Teukolsky, S.A., Vetterling, W.T., Flannery, B.P., 1992, *Numerical Recipes in Fortran, 2e,* (Cambridge University Press:Cambridge)

[16] Price, S.D., Tedesco, E. F., Cohen, M., Walker, R. G., Henry, R. C., Moshir, M., Paxton, L. J., Witterborn, F. C., "Astronomy of the Midcourse Space Experiment", New Horizons from Multi-Wavelength Sky Surveys, Proceedings of the 179th Symposium of the International Astronomical Union, held in Baltimore, USA August 26-30, 1996, Kluwer Academic Publishers, edited by Brian J. McLean, Daniel A. Golombek, Jeffrey E. Hayes, and Harry E. Payne, p. 115.

[17] Midcourse Space Experiment document TP-010200-001 F01.00-961017, 1996, "SPIRIT III Integrated Ground and On-Orbit Calibration Report in Support of CONVERT 3.2," , (Utah State University: Logan, UT)

[18] SPIRIT III Data Processing Center, August 1997, *Convert User's Manual Version 5.0*: SDL/92-113, SD-070500-0001-D10.00-970829, (Utah State University: Logan, UT)

[19] SPIRIT III Data Processing Center, August 1998, *Convert User's Manual Version 6.2*, SDL/92-113, SD-070500-0001-D11.00-980826, (Utah State University: Logan, UT)

[20] SPIRIT III Data Processing Center, *SPIRIT III Sensor Users Guide* (RV.3 5/93, SDL 92-041), (Utah State University: Logan, UT)

[21] SPIRIT III Data Processing Center, March 1996, *SPIRIT III Infrared Sensor Ground Calibration Report in Support of Convert 3.0 (*SDL/95-058), (Utah State University: Logan, UT)

[22] SPIRIT III Data Processing Center, March 1998, *SPIRIT III Infrared Sensor Ground Calibration Report in Support of Convert 5.0 (*SDL/97-056), (Utah State University: Logan, UT)

[23] Stetson, P. B. 1987, PASP, 99, 191

[24] Van Der Hucht, K. A., Morris, P. W., Williams, P. M., Setia Gunawan, D. Y. A., Beintema, D. A., Boxhoorn, D. R., De Graauw, T., Heras, A., Kester, D. J. M., Lahuis, F., Leech, K. J., Roelfsema, P. R., Salama, A., Valentijn, E. A. and Vandenbussche, B. 1996 A&A, 315, L193

APPENDIX A
SPIRIT III RELATIVE SPECTRAL RESPONSE

The relative spectral response (RSR) for the entire system for each spectral band was measured during the ground calibration using a standard source and an external (to the sensor) Michelson step-scan interferometer (SDL/97-056). The in-band response for each array was measured at high spectral resolution (1.9 cm^{-1}) with the scatter source as the reference. The noise floor of these measurements produces a dynamic range of 100-200. Ten frames of radiometer data were collected at each interferometer position and an average was taken over 8 of the 10 frames. The resulting interferogram was apodized with a Kaiser-Bessel function, Fourier transformed and phase corrected using a triangular moving average. The resulting spectra were corrected for various transmissions and optical efficiencies in the calibration chamber to produce the relative spectral response in Tables A-2 through A-6.

All relative spectral responses, except for Band B_1, show channel spectra at a spacing of approximately 2.9 cm^{-1}. A careful examination of the chamber and source factors leads to the conclusion that the absorption at 8.80 µm in Band A is real.

The relative spectral response curves are shown in Figure A-1. Electronic files of these data are available from the DCATT and Celestial Background teams in both ASCII and IDL xdr saveset formats. The percent uncertainties are the root sum square of the estimated or measured variances in the efficiencies/transmission factors in the calibration chamber, in the input and the measurement noise. The uncertainty envelopes are shown in the dashed lines in Figure A-1.

Because of the wide variety of source functions encountered by the MSX experiments the out-of-band response was measured to levels of $\sim 10^{-6}$ to 10^{-9} of the peak in-band response. Optical filters were used to block the in-band response permitting the source flux to be increased without saturating the radiometer or increasing the photon noise. The resolution was increased to 16.3 cm^{-1}. The out-of-band responses were absent or very small. The B Bands have a fairly broad response at the $\sim 10^{-5}$ level out to 6.7 µm where it is completely attenuated with a Sapphire blocking filter. The other bands have a $\sim 10^{-6}$ response shortward of the passband but over a very limited spectral range.

The nominal wavelengths for the full-widths at one-tenth-maximum (FWTM) response are listed in Table A-1. The FWHM wavelengths are listed in Table 1 of the main text.

Table A-1. Nominal SPIRIT III Square Bandpasses

	A	*B1*	*B2*	*C*	*D*	*E*
λ_{min}	6.0	4.21	4.23	11.1	13.3	18.0
λ_{max}	10.9	4.37	4.47	13.3	16.1	26.8

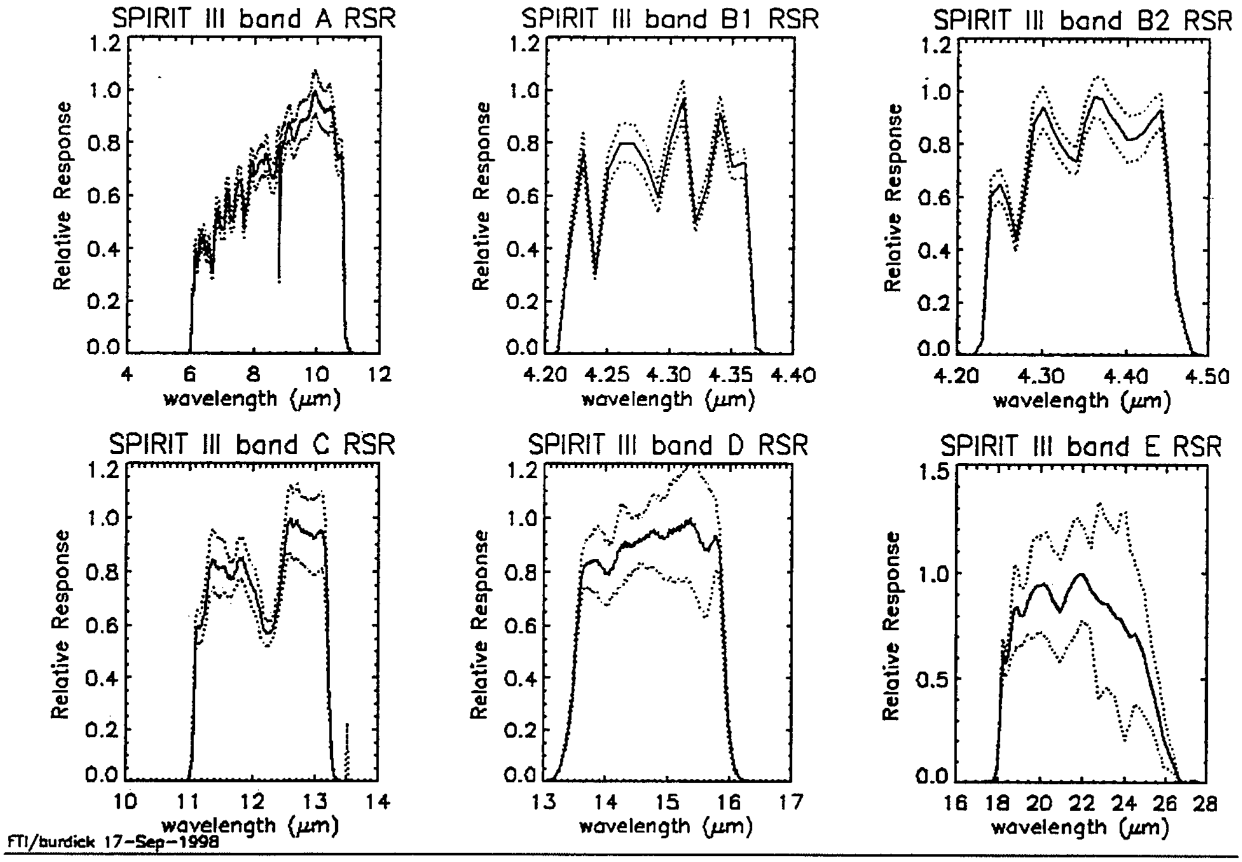

Figure A-1. SPIRIT III Radiometer Measured Relative Spectral Response (RSR)

Table A-2. Band B RSRs

Wavelength (μm)	B1	B2
4.16	0.000000	0.000000
4.17	0.000321	-0.001025
4.18	0.002414	-0.003327
4.19	0.001936	-0.000994
4.20	-0.006701	0.009207
4.21	0.011578	0.001545
4.22	0.452245	0.004766
4.23	0.777577	0.058407
4.24	0.304161	0.608008
4.25	0.697123	0.650190
4.26	0.801535	0.575328
4.27	0.799120	0.435930
4.28	0.724311	0.643920
4.29	0.596705	0.883153
4.30	0.816915	0.943367
4.31	0.968638	0.871503
4.32	0.501933	0.805304
4.33	0.645571	0.754601
4.34	0.917999	0.737379
4.35	0.709830	0.888530
4.36	0.727218	0.980702
4.37	0.029982	0.972837
4.38	-0.006652	0.913560
4.39	-0.004878	0.864674
4.40	-0.005017	0.820818
4.41	0.000629	0.827113
4.42	-0.000207	0.852358
4.43	0.001989	0.898642
4.44	0.001059	0.937199
4.45	0.003335	0.648012
4.46	0.005043	0.255528
4.47	-0.003555	0.115852
4.48	-0.001868	0.017378
4.49	0.000003	0.000589
4.50	-0.004080	0.003769
4.51	-0.000254	-0.000620
4.52	0.004378	-0.001550
4.53	-0.004066	0.003610
4.54	0.002668	0.002098
4.55	0.000000	0.000000

Table A-3. Band A RSR

Wavelength (µm)	A	Wavelength (µm)	A	Wavelength (µm)	A
5.47	0.000000	5.97	0.009396	6.47	0.385517
5.48	-0.000315	5.98	0.012155	6.48	0.379606
5.49	0.000071	5.99	0.017347	6.49	0.375760
5.50	-0.000081	6.00	0.027535	6.50	0.382499
5.51	-0.000332	6.01	0.044530	6.51	0.390996
5.52	0.000730	6.02	0.073925	6.52	0.394983
5.53	0.000099	6.03	0.120096	6.53	0.403409
5.54	-0.000260	6.04	0.174823	6.54	0.410362
5.55	0.000781	6.05	0.209913	6.55	0.414612
5.56	-0.000277	6.06	0.231350	6.56	0.418207
5.57	0.000992	6.07	0.230204	6.57	0.410824
5.58	-0.000246	6.08	0.235028	6.58	0.407698
5.59	0.000418	6.09	0.244067	6.59	0.395046
5.60	0.001200	6.10	0.263588	6.60	0.384463
5.61	0.000469	6.11	0.288916	6.61	0.368905
5.62	0.000736	6.12	0.329386	6.62	0.355570
5.63	0.000408	6.13	0.369327	6.63	0.340187
5.64	-0.000391	6.14	0.396128	6.64	0.328004
5.65	0.000149	6.15	0.403652	6.65	0.323517
5.66	0.000318	6.16	0.390063	6.66	0.315891
5.67	-0.000156	6.17	0.371658	6.67	0.313424
5.68	0.000558	6.18	0.350065	6.68	0.314371
5.69	-0.000199	6.19	0.336074	6.69	0.326072
5.70	-0.000454	6.20	0.328446	6.70	0.339979
5.71	0.000622	6.21	0.327350	6.71	0.355364
5.72	-0.000303	6.22	0.333742	6.72	0.377231
5.73	0.000125	6.23	0.346703	6.73	0.401233
5.74	0.000292	6.24	0.367139	6.74	0.426820
5.75	0.000171	6.25	0.391409	6.75	0.451653
5.76	-0.000368	6.26	0.416367	6.76	0.473748
5.77	0.000372	6.27	0.435593	6.77	0.491115
5.78	-0.000244	6.28	0.443288	6.78	0.509462
5.79	0.000207	6.29	0.442696	6.79	0.522869
5.80	-0.000233	6.30	0.440689	6.80	0.541286
5.81	0.000368	6.31	0.441459	6.81	0.549941
5.82	0.000190	6.32	0.435750	6.82	0.552796
5.83	0.000651	6.33	0.428029	6.83	0.553285
5.84	0.000471	6.34	0.418284	6.84	0.549820
5.85	0.000223	6.35	0.423546	6.85	0.537861
5.86	0.001711	6.36	0.427868	6.86	0.519079
5.87	0.002409	6.37	0.432599	6.87	0.520042
5.88	0.001856	6.38	0.445541	6.88	0.516787
5.89	0.002763	6.39	0.448921	6.89	0.509425
5.90	0.002629	6.40	0.449929	6.90	0.499657
5.91	0.003186	6.41	0.435919	6.91	0.493018
5.92	0.002621	6.42	0.433301	6.92	0.488662
5.93	0.004226	6.43	0.427905	6.93	0.485753
5.94	0.004010	6.44	0.422693	6.94	0.481985
5.95	0.005713	6.45	0.410502	6.95	0.477722
5.96	0.006218	6.46	0.398529	6.96	0.471640

Table A-3 (continued)

Wavelength (μm)	A	Wavelength (μm)	A	Wavelength (μm)	A
6.97	0.478814	7.47	0.646108	7.97	0.704601
6.98	0.477031	7.48	0.653754	7.98	0.692965
6.99	0.473341	7.49	0.652951	7.99	0.691422
7.00	0.472542	7.50	0.656863	8.00	0.687336
7.01	0.473024	7.51	0.660540	8.01	0.682620
7.02	0.471294	7.52	0.654593	8.02	0.686771
7.03	0.473169	7.53	0.659593	8.03	0.679673
7.04	0.474714	7.54	0.657494	8.04	0.690161
7.05	0.492196	7.55	0.650288	8.05	0.685682
7.06	0.511286	7.56	0.651977	8.06	0.696141
7.07	0.532313	7.57	0.642447	8.07	0.697351
7.08	0.556427	7.58	0.634934	8.08	0.700001
7.09	0.576532	7.59	0.629804	8.09	0.707844
7.10	0.589700	7.60	0.611713	8.10	0.706349
7.11	0.602659	7.61	0.592465	8.11	0.718779
7.12	0.615275	7.62	0.574673	8.12	0.715157
7.13	0.623724	7.63	0.547002	8.13	0.725554
7.14	0.623750	7.64	0.521335	8.14	0.722358
7.15	0.622621	7.65	0.495537	8.15	0.728354
7.16	0.623450	7.66	0.476073	8.16	0.727872
7.17	0.610149	7.67	0.478585	8.17	0.728263
7.18	0.599436	7.68	0.491712	8.18	0.732707
7.19	0.588277	7.69	0.522558	8.19	0.728306
7.20	0.571725	7.70	0.545698	8.20	0.735303
7.21	0.549332	7.71	0.551033	8.21	0.727248
7.22	0.536179	7.72	0.558508	8.22	0.735704
7.23	0.528989	7.73	0.560765	8.23	0.728425
7.24	0.520420	7.74	0.562598	8.24	0.737886
7.25	0.511772	7.75	0.571490	8.25	0.732891
7.26	0.511088	7.76	0.571954	8.26	0.738155
7.27	0.506482	7.77	0.583114	8.27	0.734946
7.28	0.503534	7.78	0.591672	8.28	0.732543
7.29	0.510673	7.79	0.598145	8.29	0.722298
7.30	0.512367	7.80	0.616045	8.30	0.730495
7.31	0.512250	7.81	0.623564	8.31	0.745780
7.32	0.518392	7.82	0.640710	8.32	0.748865
7.33	0.523314	7.83	0.656912	8.33	0.759329
7.34	0.526000	7.84	0.667397	8.34	0.755612
7.35	0.535264	7.85	0.687624	8.35	0.763914
7.36	0.550284	7.86	0.695020	8.36	0.755474
7.37	0.562693	7.87	0.711267	8.37	0.761074
7.38	0.581907	7.88	0.721282	8.38	0.751506
7.39	0.602190	7.89	0.723283	8.39	0.754418
7.40	0.610440	7.90	0.734138	8.40	0.741450
7.41	0.619443	7.91	0.727328	8.41	0.743307
7.42	0.628377	7.92	0.733480	8.42	0.731616
7.43	0.630253	7.93	0.725512	8.43	0.731825
7.44	0.635582	7.94	0.720886	8.44	0.719148
7.45	0.643338	7.95	0.718063	8.45	0.720453
7.46	0.641036	7.96	0.703557	8.46	0.709166

Table A-3 (continued)

Wavelength (µm)	A	Wavelength (µm)	A	Wavelength (µm)	A
8.47	0.708559	8.97	0.825100	9.47	0.882820
8.48	0.699139	8.98	0.828402	9.48	0.883419
8.49	0.697760	8.99	0.841468	9.49	0.878432
8.50	0.689022	9.00	0.842916	9.50	0.890269
8.51	0.686833	9.01	0.857745	9.51	0.881337
8.52	0.678351	9.02	0.855512	9.52	0.887906
8.53	0.677511	9.03	0.870108	9.53	0.887974
8.54	0.670695	9.04	0.867474	9.54	0.882697
8.55	0.669559	9.05	0.876884	9.55	0.891172
8.56	0.664081	9.06	0.875987	9.56	0.882921
8.57	0.666043	9.07	0.878352	9.57	0.889912
8.58	0.663119	9.08	0.880010	9.58	0.889400
8.59	0.665729	9.09	0.874489	9.59	0.885145
8.60	0.664884	9.10	0.878435	9.60	0.893114
8.61	0.666864	9.11	0.864792	9.61	0.885701
8.62	0.668923	9.12	0.868077	9.62	0.892151
8.63	0.676696	9.13	0.853531	9.63	0.891550
8.64	0.680084	9.14	0.852288	9.64	0.887027
8.65	0.690003	9.15	0.843895	9.65	0.896135
8.66	0.694586	9.16	0.836016	9.66	0.890028
8.67	0.707556	9.17	0.834195	9.67	0.896272
8.68	0.713425	9.18	0.821476	9.68	0.897772
8.69	0.729787	9.19	0.824064	9.69	0.893403
8.70	0.735895	9.20	0.811401	9.70	0.904857
8.71	0.752735	9.21	0.815731	9.71	0.900498
8.72	0.756313	9.22	0.809802	9.72	0.907391
8.73	0.777608	9.23	0.811261	9.73	0.913072
8.74	0.777458	9.24	0.815133	9.74	0.906912
8.75	0.792853	9.25	0.808357	9.75	0.920949
8.76	0.787176	9.26	0.818700	9.76	0.919963
8.77	0.784099	9.27	0.812349	9.77	0.923319
8.78	0.729027	9.28	0.821093	9.78	0.937494
8.79	0.472745	9.29	0.821801	9.79	0.933772
8.80	0.290218	9.30	0.826645	9.80	0.948474
8.81	0.503975	9.31	0.834738	9.81	0.955167
8.82	0.630103	9.32	0.832594	9.82	0.955379
8.83	0.704594	9.33	0.844496	9.83	0.971224
8.84	0.772540	9.34	0.839929	9.84	0.968972
8.85	0.776315	9.35	0.850271	9.85	0.975598
8.86	0.759803	9.36	0.852505	9.86	0.986056
8.87	0.769375	9.37	0.853988	9.87	0.977891
8.88	0.791374	9.38	0.863588	9.88	0.989367
8.89	0.786147	9.39	0.858526	9.89	0.991182
8.90	0.799746	9.40	0.870082	9.90	0.987108
8.91	0.793387	9.41	0.866701	9.91	0.998688
8.92	0.804534	9.42	0.872865	9.92	0.991888
8.93	0.797504	9.43	0.878692	9.93	0.992047
8.94	0.809826	9.44	0.874561	9.94	0.996745
8.95	0.809961	9.45	0.885759	9.95	0.984782
8.96	0.818694	9.46	0.877036	9.96	0.989746

Table A-3 (continued)

Wavelength (μm)	A	Wavelength (μm)	A	Wavelength (μm)	A
9.97	0.985776	10.47	0.918957	10.97	0.046665
9.98	0.974911	10.48	0.918424	10.98	0.045030
9.99	0.979445	10.49	0.903450	10.99	0.042951
10.00	0.968467	10.50	0.896258	11.00	0.039863
10.01	0.962926	10.51	0.892849	11.01	0.034928
10.02	0.966954	10.52	0.874568	11.02	0.029144
10.03	0.953950	10.53	0.866463	11.03	0.025034
10.04	0.955628	10.54	0.861037	11.04	0.022867
10.05	0.957908	10.55	0.842872	11.05	0.020201
10.06	0.946420	10.56	0.831666	11.06	0.016835
10.07	0.952069	10.57	0.825350	11.07	0.013841
10.08	0.949022	10.58	0.808134	11.08	0.011200
10.09	0.938937	10.59	0.798081	11.09	0.008871
10.10	0.945959	10.60	0.793470	11.10	0.007030
10.11	0.939243	10.61	0.777713	11.11	0.005513
10.12	0.933604	10.62	0.768171	11.12	0.004446
10.13	0.941431	10.63	0.765359	11.13	0.003837
10.14	0.932670	10.64	0.753631	11.14	0.003153
10.15	0.930666	10.65	0.746280	11.15	0.002699
10.16	0.935492	10.66	0.747285	11.16	0.002766
10.17	0.925777	10.67	0.739491	11.17	0.002519
10.18	0.928359	10.68	0.737160	11.18	0.001660
10.19	0.929852	10.69	0.744417	11.19	0.001119
10.20	0.918796	10.70	0.743318	11.20	0.001737
10.21	0.923639	10.71	0.742179	11.21	0.002399
10.22	0.923781	10.72	0.751495	11.22	0.002086
10.23	0.916081	10.73	0.752902	11.23	0.001401
10.24	0.924107	10.74	0.751045	11.24	0.001276
10.25	0.921999	10.75	0.758192	11.25	0.001750
10.26	0.916113	10.76	0.757480	11.26	0.002424
10.27	0.924354	10.77	0.747625	11.27	0.002722
10.28	0.920019	10.78	0.744220	11.28	0.002334
10.29	0.918400	10.79	0.732253	11.29	0.001794
10.30	0.927333	10.80	0.702943	11.30	0.001428
10.31	0.922236	10.81	0.672837	11.31	0.001314
10.32	0.922498	10.82	0.635270	11.32	0.001177
10.33	0.929504	10.83	0.581131	11.33	0.000686
10.34	0.922617	10.84	0.523840	11.34	0.000299
10.35	0.923794	10.85	0.466520	11.35	0.000187
10.36	0.931271	10.86	0.400727	11.36	-0.000313
10.37	0.925033	10.87	0.335088	11.37	-0.000577
10.38	0.927672	10.88	0.275949	11.38	0.000308
10.39	0.935860	10.89	0.218556	11.39	0.001138
10.40	0.928797	10.90	0.165904	11.40	0.000671
10.41	0.931357	10.91	0.124094	11.41	-0.000614
10.42	0.938661	10.92	0.092919	11.42	-0.001549
10.43	0.929666	10.93	0.070463	11.43	-0.001396
10.44	0.931027	10.94	0.057988	11.44	0.000127
10.45	0.934080	10.95	0.052119	11.45	0.001869
10.46	0.922022	10.96	0.048793	11.46	0.002383

Table A-3 (continued)

Wavelength (μm)	A
11.47	0.001912
11.48	0.001296
11.49	0.001150
11.50	0.001280
11.51	0.001206
11.52	0.000988
11.53	0.001041
11.54	0.001192
11.55	0.000761
11.56	-0.000265
11.57	-0.000816
11.58	-0.000105
11.59	0.000977
11.60	0.001290
11.61	0.001043
11.62	0.000650
11.63	0.000297
11.64	0.000299
11.65	0.000623
11.66	0.000696
11.67	0.000340
11.68	0.000062
11.69	-0.000012
11.70	-0.000270
11.71	-0.000345
11.72	0.000426
11.73	0.001389
11.74	0.001510
11.75	0.000965
11.76	0.000412
11.77	0.000000

Table A-4. Band C RSR

Wavelength (µm)	C	Wavelength (µm)	C	Wavelength (µm)	C
10.53	0.000000	11.03	0.045861	11.53	0.816728
10.54	-0.000914	11.04	0.073646	11.54	0.821064
10.55	-0.000727	11.05	0.116041	11.55	0.824815
10.56	-0.000745	11.06	0.180054	11.56	0.815556
10.57	-0.000710	11.07	0.268399	11.57	0.803970
10.58	-0.001392	11.08	0.367111	11.58	0.801957
10.59	-0.002924	11.09	0.461857	11.59	0.799875
10.60	-0.003552	11.10	0.541751	11.60	0.789415
10.61	-0.002006	11.11	0.582732	11.61	0.781961
10.62	-0.000540	11.12	0.592429	11.62	0.785514
10.63	-0.000048	11.13	0.595371	11.63	0.786397
10.64	0.000941	11.14	0.600282	11.64	0.776755
10.65	0.001114	11.15	0.596081	11.65	0.770338
10.66	-0.000376	11.16	0.589153	11.66	0.775501
10.67	-0.000307	11.17	0.594159	11.67	0.779546
10.68	0.000252	11.18	0.600414	11.68	0.775725
10.69	-0.000401	11.19	0.599422	11.69	0.777365
10.70	-0.001333	11.20	0.604639	11.70	0.790802
10.71	-0.002582	11.21	0.619805	11.71	0.801077
10.72	-0.003791	11.22	0.630077	11.72	0.801720
10.73	-0.003848	11.23	0.634649	11.73	0.808188
10.74	-0.003444	11.24	0.650775	11.74	0.826442
10.75	-0.003285	11.25	0.675642	11.75	0.839255
10.76	-0.003240	11.26	0.691725	11.76	0.838775
10.77	-0.002170	11.27	0.707202	11.77	0.840581
10.78	-0.001128	11.28	0.733673	11.78	0.851027
10.79	-0.002164	11.29	0.757055	11.79	0.855590
10.80	-0.003254	11.30	0.770278	11.80	0.849256
10.81	-0.002783	11.31	0.789894	11.81	0.847240
10.82	-0.002651	11.32	0.815887	11.82	0.853587
10.83	-0.002713	11.33	0.828956	11.83	0.852686
10.84	-0.002335	11.34	0.829510	11.84	0.839411
10.85	-0.002059	11.35	0.837900	11.85	0.829114
10.86	-0.001661	11.36	0.851178	11.86	0.829090
10.87	-0.002191	11.37	0.850236	11.87	0.826714
10.88	-0.004347	11.38	0.841676	11.88	0.813243
10.89	-0.005525	11.39	0.842430	11.89	0.799741
10.90	-0.003773	11.40	0.841868	11.90	0.796164
10.91	-0.001382	11.41	0.828683	11.91	0.793991
10.92	0.000142	11.42	0.819150	11.92	0.784160
10.93	0.000674	11.43	0.821549	11.93	0.774647
10.94	0.000007	11.44	0.819564	11.94	0.773922
10.95	-0.000353	11.45	0.809130	11.95	0.773681
10.96	0.001146	11.46	0.808749	11.96	0.764548
10.97	0.003160	11.47	0.818953	11.97	0.753388
10.98	0.007546	11.48	0.821419	11.98	0.750020
10.99	0.010988	11.49	0.814055	11.99	0.749957
11.00	0.013128	11.50	0.813937	12.00	0.743866
11.01	0.018689	11.51	0.821276	12.01	0.734533
11.02	0.029163	11.52	0.820997	12.02	0.731074

Table A-4 (continued)

Wavelength (μm)	C	Wavelength (μm)	C	Wavelength (μm)	C
12.03	0.730451	12.53	0.937302	13.03	0.945024
12.04	0.722635	12.54	0.953886	13.04	0.944792
12.05	0.708970	12.55	0.974576	13.05	0.941964
12.06	0.699785	12.56	0.987508	13.06	0.945179
12.07	0.695293	12.57	0.987643	13.07	0.952966
12.08	0.686018	12.58	0.987425	13.08	0.957635
12.09	0.671838	12.59	0.994191	13.09	0.955204
12.10	0.661443	12.60	0.999549	13.10	0.949419
12.11	0.655480	12.61	0.992145	13.11	0.946060
12.12	0.645937	12.62	0.976015	13.12	0.941600
12.13	0.629844	12.63	0.967222	13.13	0.928023
12.14	0.614818	12.64	0.970762	13.14	0.901526
12.15	0.606542	12.65	0.976142	13.15	0.865228
12.16	0.600001	12.66	0.974949	13.16	0.822691
12.17	0.591091	12.67	0.973701	13.17	0.770620
12.18	0.582555	12.68	0.980872	13.18	0.702625
12.19	0.578402	12.69	0.991611	13.19	0.618561
12.20	0.576725	12.70	0.991006	13.20	0.526146
12.21	0.572682	12.71	0.979810	13.21	0.436962
12.22	0.568462	12.72	0.970563	13.22	0.355539
12.23	0.569773	12.73	0.971465	13.23	0.282405
12.24	0.573974	12.74	0.973731	13.24	0.217163
12.25	0.573115	12.75	0.967147	13.25	0.163171
12.26	0.568583	12.76	0.954937	13.26	0.121814
12.27	0.568734	12.77	0.950207	13.27	0.090776
12.28	0.576485	12.78	0.954999	13.28	0.066893
12.29	0.582601	12.79	0.959023	13.29	0.048544
12.30	0.582822	12.80	0.953985	13.30	0.035263
12.31	0.584365	12.81	0.945174	13.31	0.026145
12.32	0.593394	12.82	0.943652	13.32	0.019499
12.33	0.605218	12.83	0.949313	13.33	0.013888
12.34	0.611266	12.84	0.952164	13.34	0.009122
12.35	0.613958	12.85	0.946372	13.35	0.005454
12.36	0.624829	12.86	0.940372	13.36	0.003148
12.37	0.643474	12.87	0.941482	13.37	0.002164
12.38	0.660871	12.88	0.946862	13.38	0.001908
12.39	0.671621	12.89	0.946624	13.39	0.001694
12.40	0.684086	12.90	0.940718	13.40	0.001106
12.41	0.704255	12.91	0.936569	13.41	0.000097
12.42	0.725692	12.92	0.938257	13.42	-0.000989
12.43	0.741261	12.93	0.939507	13.43	-0.001558
12.44	0.755515	12.94	0.934586	13.44	-0.001172
12.45	0.777914	12.95	0.926862	13.45	-0.000393
12.46	0.804879	12.96	0.924296	13.46	-0.000190
12.47	0.826315	12.97	0.928839	13.47	-0.000981
12.48	0.840680	12.98	0.932106	13.48	-0.002009
12.49	0.858359	12.99	0.929682	13.49	-0.002046
12.50	0.884950	13.00	0.925710	13.50	-0.000846
12.51	0.910804	13.01	0.928891	13.51	0.000130
12.52	0.926906	13.02	0.938114	13.52	-0.000427

Table A-4 (continued)

Wavelength (μm)	C
13.53	-0.002132
13.54	-0.003475
13.55	-0.003364
13.56	-0.002184
13.57	-0.001205
13.58	-0.001231
13.59	-0.001799
13.60	-0.002197
13.61	-0.002341
13.62	-0.002575
13.63	-0.002992
13.64	-0.003254
13.65	-0.003138
13.66	-0.003012
13.67	-0.003424
13.68	-0.004068
13.69	-0.004130
13.70	0.000000

Table A-5. Band D RSR

Wavelength (μm)	D	Wavelength (μm)	D	Wavelength (μm)	D
12.65	0.000000	13.15	0.011608	13.65	0.825943
12.66	0.000321	13.16	0.013663	13.66	0.822369
12.67	0.000065	13.17	0.016324	13.67	0.823471
12.68	-0.000102	13.18	0.019253	13.68	0.830214
12.69	-0.000022	13.19	0.022441	13.69	0.835983
12.70	0.000701	13.20	0.026484	13.70	0.835575
12.71	0.001695	13.21	0.031327	13.71	0.831450
12.72	0.002043	13.22	0.035915	13.72	0.830640
12.73	0.001273	13.23	0.039546	13.73	0.835972
12.74	0.000357	13.24	0.042962	13.74	0.842487
12.75	0.000251	13.25	0.047680	13.75	0.843340
12.76	0.000767	13.26	0.054475	13.76	0.838448
12.77	0.001201	13.27	0.062068	13.77	0.835930
12.78	0.001421	13.28	0.069414	13.78	0.840715
12.79	0.001541	13.29	0.076381	13.79	0.848519
12.80	0.001379	13.30	0.083847	13.80	0.851021
12.81	0.000950	13.31	0.093238	13.81	0.845878
12.82	0.000846	13.32	0.104331	13.82	0.839555
12.83	0.001297	13.33	0.115835	13.83	0.839879
12.84	0.001753	13.34	0.126651	13.84	0.846564
12.85	0.001440	13.35	0.137468	13.85	0.851191
12.86	0.000448	13.36	0.149714	13.86	0.846679
12.87	-0.000587	13.37	0.163611	13.87	0.835952
12.88	-0.000711	13.38	0.177109	13.88	0.829414
12.89	0.000532	13.39	0.189313	13.89	0.831378
12.90	0.002191	13.40	0.202291	13.90	0.835534
12.91	0.002872	13.41	0.219043	13.91	0.833537
12.92	0.002011	13.42	0.240142	13.92	0.824632
12.93	0.000662	13.43	0.263148	13.93	0.816336
12.94	0.000025	13.44	0.285386	13.94	0.815037
12.95	0.000216	13.45	0.308206	13.95	0.818320
12.96	0.000953	13.46	0.334879	13.96	0.817801
12.97	0.001998	13.47	0.366793	13.97	0.809081
12.98	0.002836	13.48	0.401383	13.98	0.797298
12.99	0.002972	13.49	0.435008	13.99	0.791785
13.00	0.002545	13.50	0.467787	14.00	0.795648
13.01	0.002387	13.51	0.503205	14.01	0.802283
13.02	0.002790	13.52	0.542570	14.02	0.802683
13.03	0.003333	13.53	0.582033	14.03	0.795893
13.04	0.003784	13.54	0.616869	14.04	0.790909
13.05	0.004286	13.55	0.646134	14.05	0.795067
13.06	0.004793	13.56	0.675141	14.06	0.806166
13.07	0.005073	13.57	0.707403	14.07	0.814990
13.08	0.005321	13.58	0.739074	14.08	0.815311
13.09	0.005952	13.59	0.761811	14.09	0.810644
13.10	0.006981	13.60	0.774509	14.10	0.810415
13.11	0.007912	13.61	0.784140	14.11	0.819688
13.12	0.008632	13.62	0.797612	14.12	0.833470
13.13	0.009349	13.63	0.813650	14.13	0.842518
13.14	0.010259	13.64	0.824717	14.14	0.843014

Table A-5 (continued)

Wavelength (µm)	D	Wavelength (µm)	D	Wavelength (µm)	D
14.15	0.840858	14.65	0.937680	15.15	0.969708
14.16	0.845173	14.66	0.938662	15.16	0.969819
14.17	0.858356	14.67	0.934909	15.17	0.963125
14.18	0.873133	14.68	0.931777	15.18	0.955141
14.19	0.880467	14.69	0.934054	15.19	0.954374
14.20	0.879333	14.70	0.941420	15.20	0.961968
14.21	0.877475	14.71	0.948868	15.21	0.971870
14.22	0.882795	14.72	0.951639	15.22	0.977426
14.23	0.894376	14.73	0.949521	15.23	0.976115
14.24	0.903479	14.74	0.946595	15.24	0.970820
14.25	0.903336	14.75	0.947398	15.25	0.967411
14.26	0.896563	14.76	0.951775	15.26	0.970624
14.27	0.892826	14.77	0.955043	15.27	0.980717
14.28	0.898410	14.78	0.952860	15.28	0.991269
14.29	0.909069	14.79	0.945805	15.29	0.994139
14.30	0.914676	14.80	0.940134	15.30	0.989389
14.31	0.909611	14.81	0.940703	15.31	0.982754
14.32	0.899118	14.82	0.946059	15.32	0.980384
14.33	0.893522	14.83	0.949952	15.33	0.984758
14.34	0.897704	14.84	0.947324	15.34	0.993273
14.35	0.906330	14.85	0.938893	15.35	0.999845
14.36	0.909839	14.86	0.930284	15.36	0.998665
14.37	0.904806	14.87	0.927194	15.37	0.988891
14.38	0.896674	14.88	0.930470	15.38	0.978465
14.39	0.893786	14.89	0.935635	15.39	0.973257
14.40	0.898466	14.90	0.937213	15.40	0.973919
14.41	0.904924	14.91	0.933157	15.41	0.976870
14.42	0.906427	14.92	0.925829	15.42	0.977188
14.43	0.901816	14.93	0.921065	15.43	0.971668
14.44	0.896659	14.94	0.922655	15.44	0.961046
14.45	0.897554	14.95	0.928787	15.45	0.951551
14.46	0.905123	14.96	0.933239	15.46	0.947489
14.47	0.913402	14.97	0.932568	15.47	0.947112
14.48	0.915933	14.98	0.929792	15.48	0.946256
14.49	0.912415	14.99	0.930448	15.49	0.941508
14.50	0.908764	15.00	0.937548	15.50	0.932049
14.51	0.910846	15.01	0.948587	15.51	0.920434
14.52	0.918287	15.02	0.957504	15.52	0.912142
14.53	0.924783	15.03	0.959384	15.53	0.909890
14.54	0.924692	15.04	0.954193	15.54	0.910279
14.55	0.918753	15.05	0.947151	15.55	0.909222
14.56	0.913452	15.06	0.944931	15.56	0.904386
14.57	0.914610	15.07	0.950209	15.57	0.896062
14.58	0.921527	15.08	0.959500	15.58	0.887147
14.59	0.928042	15.09	0.964024	15.59	0.882306
14.60	0.928879	15.10	0.961187	15.60	0.883108
14.61	0.924707	15.11	0.955007	15.61	0.885847
14.62	0.921409	15.12	0.951874	15.62	0.887209
14.63	0.923881	15.13	0.955241	15.63	0.885888
14.64	0.931169	15.14	0.963108	15.64	0.882809

Table A-5 (continued)

Wavelength (μm)	D	Wavelength (μm)	D	Wavelength (μm)	D
15.65	0.880832	16.15	0.023951	16.65	0.000380
15.66	0.884037	16.16	0.021302	16.66	0.000000
15.67	0.891459	16.17	0.018922		
15.68	0.899507	16.18	0.016516		
15.69	0.905404	16.19	0.013988		
15.70	0.908133	16.20	0.011334		
15.71	0.908775	16.21	0.009027		
15.72	0.910769	16.22	0.007571		
15.73	0.917233	16.23	0.006927		
15.74	0.925953	16.24	0.006904		
15.75	0.933744	16.25	0.007103		
15.76	0.937747	16.26	0.006717		
15.77	0.936421	16.27	0.005788		
15.78	0.930376	16.28	0.004565		
15.79	0.922821	16.29	0.003321		
15.80	0.915099	16.30	0.002509		
15.81	0.905498	16.31	0.002094		
15.82	0.891282	16.32	0.001752		
15.83	0.869708	16.33	0.001326		
15.84	0.838428	16.34	0.000689		
15.85	0.799751	16.35	-0.000035		
15.86	0.758458	16.36	-0.000545		
15.87	0.716497	16.37	-0.000772		
15.88	0.674211	16.38	-0.000678		
15.89	0.630478	16.39	-0.000254		
15.90	0.583535	16.40	0.000418		
15.91	0.533313	16.41	0.001288		
15.92	0.482413	16.42	0.002296		
15.93	0.432748	16.43	0.003342		
15.94	0.386144	16.44	0.003928		
15.95	0.344633	16.45	0.003904		
15.96	0.307903	16.46	0.003293		
15.97	0.274377	16.47	0.002186		
15.98	0.243387	16.48	0.001143		
15.99	0.214772	16.49	0.000617		
16.00	0.188799	16.50	0.000547		
16.01	0.166443	16.51	0.000823		
16.02	0.147306	16.52	0.000898		
16.03	0.130566	16.53	0.000367		
16.04	0.115567	16.54	-0.000561		
16.05	0.101705	16.55	-0.001688		
16.06	0.088683	16.56	-0.002371		
16.07	0.076368	16.57	-0.002137		
16.08	0.065196	16.58	-0.001276		
16.09	0.055430	16.59	0.000003		
16.10	0.047219	16.60	0.001212		
16.11	0.040794	16.61	0.001796		
16.12	0.035547	16.62	0.001877		
16.13	0.031062	16.63	0.001532		
16.14	0.027221	16.64	0.000940		

Table A-6. Band E RSR

Wavelength (µm)	E	Wavelength (µm)	E	Wavelength (µm)	E
17.05	0.000000	17.55	0.005731	18.05	0.183946
17.06	0.001952	17.56	0.006073	18.06	0.204906
17.07	0.002120	17.57	0.006415	18.07	0.225867
17.08	0.002288	17.58	0.006758	18.08	0.246827
17.09	0.002455	17.59	0.007100	18.09	0.267788
17.10	0.002623	17.60	0.007442	18.10	0.288749
17.11	0.002791	17.61	0.007785	18.11	0.309709
17.12	0.002959	17.62	0.008127	18.12	0.330670
17.13	0.003126	17.63	0.008469	18.13	0.352437
17.14	0.003294	17.64	0.008278	18.14	0.375198
17.15	0.003462	17.65	0.007928	18.15	0.397958
17.16	0.003629	17.66	0.007578	18.16	0.420719
17.17	0.003711	17.67	0.007228	18.17	0.443479
17.18	0.003699	17.68	0.006877	18.18	0.466240
17.19	0.003687	17.69	0.006527	18.19	0.489000
17.20	0.003675	17.70	0.006177	18.20	0.511761
17.21	0.003662	17.71	0.005827	18.21	0.534521
17.22	0.003650	17.72	0.005476	18.22	0.557282
17.23	0.003638	17.73	0.005126	18.23	0.580042
17.24	0.003626	17.74	0.004776	18.24	0.602803
17.25	0.003614	17.75	0.004425	18.25	0.625563
17.26	0.003601	17.76	0.005355	18.26	0.629681
17.27	0.003589	17.77	0.006852	18.27	0.625185
17.28	0.003570	17.78	0.008349	18.28	0.620689
17.29	0.003349	17.79	0.009846	18.29	0.616193
17.30	0.003127	17.80	0.011343	18.30	0.611697
17.31	0.002906	17.81	0.012840	18.31	0.607201
17.32	0.002685	17.82	0.014338	18.32	0.602705
17.33	0.002464	17.83	0.015835	18.33	0.598209
17.34	0.002242	17.84	0.017332	18.34	0.593714
17.35	0.002021	17.85	0.018829	18.35	0.589218
17.36	0.001800	17.86	0.020326	18.36	0.584722
17.37	0.001579	17.87	0.021823	18.37	0.580226
17.38	0.001357	17.88	0.024665	18.38	0.575730
17.39	0.001136	17.89	0.029156	18.39	0.577537
17.40	0.001140	17.90	0.033647	18.40	0.581577
17.41	0.001434	17.91	0.038138	18.41	0.585617
17.42	0.001729	17.92	0.042629	18.42	0.589656
17.43	0.002023	17.93	0.047120	18.43	0.593696
17.44	0.002317	17.94	0.051611	18.44	0.597735
17.45	0.002611	17.95	0.056102	18.45	0.601775
17.46	0.002906	17.96	0.060593	18.46	0.605814
17.47	0.003200	17.97	0.065084	18.47	0.609854
17.48	0.003494	17.98	0.069575	18.48	0.613893
17.49	0.003788	17.99	0.074067	18.49	0.617933
17.50	0.004083	18.00	0.079143	18.50	0.621972
17.51	0.004377	18.01	0.100104	18.51	0.626012
17.52	0.004704	18.02	0.121064	18.52	0.632841
17.53	0.005046	18.03	0.142025	18.53	0.641469
17.54	0.005388	18.04	0.162985	18.54	0.650097

Table A-6 (continued)

Wavelength (μm)	E	Wavelength (μm)	E	Wavelength (μm)	E
18.55	0.658725	19.05	0.804012	19.55	0.902691
18.56	0.667353	19.06	0.801512	19.56	0.904980
18.57	0.675981	19.07	0.801528	19.57	0.907269
18.58	0.684609	19.08	0.801545	19.58	0.909558
18.59	0.693237	19.09	0.801561	19.59	0.911847
18.60	0.701865	19.10	0.801578	19.60	0.914137
18.61	0.710493	19.11	0.801594	19.61	0.916426
18.62	0.719121	19.12	0.801611	19.62	0.918715
18.63	0.727749	19.13	0.801627	19.63	0.921004
18.64	0.736376	19.14	0.801644	19.64	0.922906
18.65	0.744552	19.15	0.801660	19.65	0.924235
18.66	0.751613	19.16	0.801677	19.66	0.925564
18.67	0.758675	19.17	0.801693	19.67	0.926893
18.68	0.765736	19.18	0.801710	19.68	0.928222
18.69	0.772798	19.19	0.801726	19.69	0.929551
18.70	0.779859	19.20	0.801850	19.70	0.930880
18.71	0.786921	19.21	0.804696	19.71	0.932209
18.72	0.793982	19.22	0.807542	19.72	0.933537
18.73	0.801044	19.23	0.810388	19.73	0.934866
18.74	0.808105	19.24	0.813234	19.74	0.936195
18.75	0.815167	19.25	0.816080	19.75	0.937524
18.76	0.822228	19.26	0.818926	19.76	0.938853
18.77	0.829290	19.27	0.821772	19.77	0.940182
18.78	0.836351	19.28	0.824618	19.78	0.941511
18.79	0.838203	19.29	0.827464	19.79	0.942322
18.80	0.838553	19.30	0.830310	19.80	0.942399
18.81	0.838903	19.31	0.833155	19.81	0.942475
18.82	0.839253	19.32	0.836001	19.82	0.942551
18.83	0.839603	19.33	0.838847	19.83	0.942628
18.84	0.839953	19.34	0.841693	19.84	0.942704
18.85	0.840303	19.35	0.844767	19.85	0.942780
18.86	0.840653	19.36	0.847934	19.86	0.942856
18.87	0.841003	19.37	0.851101	19.87	0.942933
18.88	0.841353	19.38	0.854268	19.88	0.943009
18.89	0.841703	19.39	0.857435	19.89	0.943085
18.90	0.842053	19.40	0.860601	19.90	0.943162
18.91	0.842403	19.41	0.863768	19.91	0.943238
18.92	0.842532	19.42	0.866935	19.92	0.943314
18.93	0.839569	19.43	0.870102	19.93	0.943390
18.94	0.836606	19.44	0.873269	19.94	0.943569
18.95	0.833643	19.45	0.876436	19.95	0.944174
18.96	0.830680	19.46	0.879603	19.96	0.944779
18.97	0.827717	19.47	0.882770	19.97	0.945384
18.98	0.824754	19.48	0.885936	19.98	0.945989
18.99	0.821791	19.49	0.888957	19.99	0.946594
19.00	0.818828	19.50	0.891246	20.00	0.947199
19.01	0.815865	19.51	0.893535	20.01	0.947804
19.02	0.812902	19.52	0.895824	20.02	0.948409
19.03	0.809938	19.53	0.898113	20.03	0.949014
19.04	0.806975	19.54	0.900402	20.04	0.949619

Table A-6 (continued)

Wavelength (μm)	E	Wavelength (μm)	E	Wavelength (μm)	E
20.05	0.950224	20.55	0.883762	21.05	0.853976
20.06	0.950829	20.56	0.881296	21.06	0.856254
20.07	0.951434	20.57	0.878831	21.07	0.858532
20.08	0.952039	20.58	0.877089	21.08	0.861315
20.09	0.952644	20.59	0.875430	21.09	0.864290
20.10	0.952395	20.60	0.873771	21.10	0.867264
20.11	0.951841	20.61	0.872112	21.11	0.870239
20.12	0.951288	20.62	0.870453	21.12	0.873214
20.13	0.950734	20.63	0.868793	21.13	0.876189
20.14	0.950181	20.64	0.867134	21.14	0.879163
20.15	0.949628	20.65	0.865475	21.15	0.882138
20.16	0.949075	20.66	0.863816	21.16	0.885113
20.17	0.948521	20.67	0.862157	21.17	0.888088
20.18	0.947968	20.68	0.860497	21.18	0.891062
20.19	0.947415	20.69	0.858838	21.19	0.894037
20.20	0.946861	20.70	0.857179	21.20	0.897012
20.21	0.946308	20.71	0.855520	21.21	0.899987
20.22	0.945754	20.72	0.853861	21.22	0.902961
20.23	0.945201	20.73	0.852202	21.23	0.905936
20.24	0.944648	20.74	0.850461	21.24	0.908911
20.25	0.944052	20.75	0.848618	21.25	0.911413
20.26	0.942446	20.76	0.846775	21.26	0.913341
20.27	0.940841	20.77	0.844931	21.27	0.915270
20.28	0.939235	20.78	0.843088	21.28	0.917198
20.29	0.937629	20.79	0.841244	21.29	0.919126
20.30	0.936023	20.80	0.839401	21.30	0.921055
20.31	0.934417	20.81	0.837558	21.31	0.922983
20.32	0.932812	20.82	0.835714	21.32	0.924911
20.33	0.931206	20.83	0.833871	21.33	0.926840
20.34	0.929600	20.84	0.832027	21.34	0.928768
20.35	0.927994	20.85	0.830184	21.35	0.930697
20.36	0.926388	20.86	0.828341	21.36	0.932625
20.37	0.924783	20.87	0.826497	21.37	0.934553
20.38	0.923177	20.88	0.824654	21.38	0.936482
20.39	0.921571	20.89	0.822811	21.39	0.938410
20.40	0.919965	20.90	0.820967	21.40	0.940338
20.41	0.918277	20.91	0.822086	21.41	0.942267
20.42	0.915812	20.92	0.824364	21.42	0.944195
20.43	0.913346	20.93	0.826642	21.43	0.946077
20.44	0.910881	20.94	0.828919	21.44	0.947952
20.45	0.908416	20.95	0.831197	21.45	0.949828
20.46	0.905950	20.96	0.833475	21.46	0.951703
20.47	0.903485	20.97	0.835753	21.47	0.953579
20.48	0.901019	20.98	0.838031	21.48	0.955455
20.49	0.898554	20.99	0.840309	21.49	0.957330
20.50	0.896089	21.00	0.842587	21.50	0.959206
20.51	0.893623	21.01	0.844865	21.51	0.961081
20.52	0.891158	21.02	0.847143	21.52	0.962957
20.53	0.888692	21.03	0.849420	21.53	0.964833
20.54	0.886227	21.04	0.851698	21.54	0.966708

Table A-6 (continued)

Wavelength (µm)	E	Wavelength (µm)	E	Wavelength (µm)	E
21.55	0.968584	22.05	0.985593	22.55	0.898875
21.56	0.970459	22.06	0.983885	22.56	0.897496
21.57	0.972335	22.07	0.982177	22.57	0.896117
21.58	0.974211	22.08	0.980468	22.58	0.894738
21.59	0.976086	22.09	0.978760	22.59	0.893359
21.60	0.977932	22.10	0.977052	22.60	0.891980
21.61	0.979105	22.11	0.975343	22.61	0.890601
21.62	0.980278	22.12	0.973635	22.62	0.889222
21.63	0.981451	22.13	0.971927	22.63	0.887843
21.64	0.982624	22.14	0.970218	22.64	0.886464
21.65	0.983796	22.15	0.968510	22.65	0.885085
21.66	0.984969	22.16	0.966447	22.66	0.883705
21.67	0.986142	22.17	0.964201	22.67	0.882326
21.68	0.987315	22.18	0.961955	22.68	0.880947
21.69	0.988488	22.19	0.959709	22.69	0.879568
21.70	0.989661	22.20	0.957463	22.70	0.878189
21.71	0.990834	22.21	0.955217	22.71	0.876810
21.72	0.992007	22.22	0.952971	22.72	0.875431
21.73	0.993180	22.23	0.950724	22.73	0.874052
21.74	0.994353	22.24	0.948478	22.74	0.872929
21.75	0.995526	22.25	0.946232	22.75	0.872260
21.76	0.996699	22.26	0.943986	22.76	0.871591
21.77	0.997872	22.27	0.941740	22.77	0.870921
21.78	0.999044	22.28	0.939494	22.78	0.870252
21.79	0.999211	22.29	0.937248	22.79	0.869583
21.80	0.999256	22.30	0.935002	22.80	0.868914
21.81	0.999301	22.31	0.932755	22.81	0.868245
21.82	0.999346	22.32	0.930509	22.82	0.867576
21.83	0.999391	22.33	0.928263	22.83	0.866906
21.84	0.999436	22.34	0.926017	22.84	0.866237
21.85	0.999481	22.35	0.924321	22.85	0.865568
21.86	0.999526	22.36	0.923055	22.86	0.864899
21.87	0.999571	22.37	0.921790	22.87	0.864230
21.88	0.999615	22.38	0.920524	22.88	0.863560
21.89	0.999660	22.39	0.919258	22.89	0.862891
21.90	0.999705	22.40	0.917992	22.90	0.862222
21.91	0.999750	22.41	0.916726	22.91	0.861553
21.92	0.999795	22.42	0.915460	22.92	0.860884
21.93	0.999840	22.43	0.914194	22.93	0.860215
21.94	0.999885	22.44	0.912928	22.94	0.859680
21.95	0.999930	22.45	0.911662	22.95	0.859569
21.96	0.999975	22.46	0.910396	22.96	0.859458
21.97	0.999260	22.47	0.909131	22.97	0.859348
21.98	0.997552	22.48	0.907865	22.98	0.859237
21.99	0.995843	22.49	0.906599	22.99	0.859126
22.00	0.994135	22.50	0.905333	23.00	0.859016
22.01	0.992427	22.51	0.904067	23.01	0.858905
22.02	0.990718	22.52	0.902801	23.02	0.858794
22.03	0.989010	22.53	0.901535	23.03	0.858684
22.04	0.987302	22.54	0.900254	23.04	0.858573

Table A-6 (continued)

Wavelength (μm)	E	Wavelength (μm)	E	Wavelength (μm)	E
23.05	0.858462	23.55	0.797595	24.05	0.734370
23.06	0.858352	23.56	0.796239	24.06	0.732508
23.07	0.858241	23.57	0.795427	24.07	0.730646
23.08	0.858130	23.58	0.794867	24.08	0.728784
23.09	0.858020	23.59	0.794307	24.09	0.726922
23.10	0.857909	23.60	0.793747	24.10	0.725060
23.11	0.857798	23.61	0.793188	24.11	0.723198
23.12	0.857688	23.62	0.792628	24.12	0.721336
23.13	0.857577	23.63	0.792068	24.13	0.719474
23.14	0.857466	23.64	0.791508	24.14	0.717612
23.15	0.856242	23.65	0.790949	24.15	0.715750
23.16	0.854666	23.66	0.790389	24.16	0.713888
23.17	0.853091	23.67	0.789829	24.17	0.712026
23.18	0.851515	23.68	0.789269	24.18	0.710164
23.19	0.849939	23.69	0.788709	24.19	0.708302
23.20	0.848363	23.70	0.788149	24.20	0.706440
23.21	0.846787	23.71	0.787590	24.21	0.704578
23.22	0.845212	23.72	0.787030	24.22	0.702716
23.23	0.843636	23.73	0.786470	24.23	0.702476
23.24	0.842060	23.74	0.785910	24.24	0.703240
23.25	0.840484	23.75	0.785351	24.25	0.704004
23.26	0.838908	23.76	0.784791	24.26	0.704767
23.27	0.837333	23.77	0.784231	24.27	0.705531
23.28	0.835757	23.78	0.783589	24.28	0.706294
23.29	0.834181	23.79	0.781775	24.29	0.707058
23.30	0.832605	23.80	0.779961	24.30	0.707822
23.31	0.831030	23.81	0.778147	24.31	0.708586
23.32	0.829454	23.82	0.776333	24.32	0.709349
23.33	0.827878	23.83	0.774519	24.33	0.710113
23.34	0.826302	23.84	0.772705	24.34	0.710876
23.35	0.824726	23.85	0.770891	24.35	0.711640
23.36	0.823351	23.86	0.769077	24.36	0.712404
23.37	0.821996	23.87	0.767263	24.37	0.713167
23.38	0.820640	23.88	0.765450	24.38	0.713931
23.39	0.819284	23.89	0.763636	24.39	0.714695
23.40	0.817929	23.90	0.761822	24.40	0.715458
23.41	0.816573	23.91	0.760008	24.41	0.716222
23.42	0.815217	23.92	0.758194	24.42	0.716986
23.43	0.813862	23.93	0.756380	24.43	0.717749
23.44	0.812506	23.94	0.754566	24.44	0.718513
23.45	0.811151	23.95	0.752752	24.45	0.719277
23.46	0.809795	23.96	0.750938	24.46	0.717883
23.47	0.808439	23.97	0.749124	24.47	0.715827
23.48	0.807084	23.98	0.747310	24.48	0.713771
23.49	0.805728	23.99	0.745496	24.49	0.711716
23.50	0.804373	24.00	0.743680	24.50	0.709660
23.51	0.803017	24.01	0.741818	24.51	0.707604
23.52	0.801661	24.02	0.739956	24.52	0.705549
23.53	0.800306	24.03	0.738094	24.53	0.703493
23.54	0.798950	24.04	0.736232	24.54	0.701437

Table A-6 (continued)

Wavelength (μm)	E	Wavelength (μm)	E	Wavelength (μm)	E
24.55	0.699382	25.05	0.553530	25.55	0.360988
24.56	0.697326	25.06	0.549378	25.56	0.356841
24.57	0.695270	25.07	0.545225	25.57	0.352694
24.58	0.693215	25.08	0.541073	25.58	0.348547
24.59	0.691159	25.09	0.536920	25.59	0.344400
24.60	0.689103	25.10	0.532768	25.60	0.340253
24.61	0.687048	25.11	0.528615	25.61	0.336106
24.62	0.684992	25.12	0.524463	25.62	0.331959
24.63	0.682936	25.13	0.520310	25.63	0.327812
24.64	0.680881	25.14	0.516158	25.64	0.323665
24.65	0.678825	25.15	0.512005	25.65	0.319518
24.66	0.676769	25.16	0.507852	25.66	0.315371
24.67	0.674714	25.17	0.504031	25.67	0.311047
24.68	0.672658	25.18	0.500487	25.68	0.306652
24.69	0.670273	25.19	0.496943	25.69	0.302257
24.70	0.667529	25.20	0.493399	25.70	0.297862
24.71	0.664784	25.21	0.489855	25.71	0.293468
24.72	0.662040	25.22	0.486310	25.72	0.289073
24.73	0.659295	25.23	0.482766	25.73	0.284678
24.74	0.656551	25.24	0.479222	25.74	0.280283
24.75	0.653806	25.25	0.475678	25.75	0.275889
24.76	0.651062	25.26	0.472133	25.76	0.271494
24.77	0.648317	25.27	0.468589	25.77	0.267099
24.78	0.645573	25.28	0.465045	25.78	0.262704
24.79	0.642828	25.29	0.461501	25.79	0.258310
24.80	0.640084	25.30	0.457956	25.80	0.253915
24.81	0.637339	25.31	0.454412	25.81	0.249520
24.82	0.634595	25.32	0.450868	25.82	0.245126
24.83	0.631850	25.33	0.447324	25.83	0.240731
24.84	0.629106	25.34	0.443780	25.84	0.236336
24.85	0.626361	25.35	0.440235	25.85	0.231941
24.86	0.623616	25.36	0.436691	25.86	0.227547
24.87	0.620872	25.37	0.433147	25.87	0.223152
24.88	0.618127	25.38	0.429603	25.88	0.218757
24.89	0.615383	25.39	0.426059	25.89	0.214362
24.90	0.612638	25.40	0.422514	25.90	0.209968
24.91	0.609894	25.41	0.418970	25.91	0.205573
24.92	0.607149	25.42	0.414899	25.92	0.201279
24.93	0.603361	25.43	0.410752	25.93	0.198848
24.94	0.599208	25.44	0.406605	25.94	0.196416
24.95	0.595056	25.45	0.402458	25.95	0.193985
24.96	0.590903	25.46	0.398311	25.96	0.191554
24.97	0.586751	25.47	0.394164	25.97	0.189123
24.98	0.582598	25.48	0.390017	25.98	0.186691
24.99	0.578445	25.49	0.385870	25.99	0.184260
25.00	0.574293	25.50	0.381723	26.00	0.181829
25.01	0.570140	25.51	0.377576	26.01	0.179398
25.02	0.565988	25.52	0.373429	26.02	0.176967
25.03	0.561835	25.53	0.369282	26.03	0.174535
25.04	0.557683	25.54	0.365135	26.04	0.172104

Table A-6 (continued)

Wavelength (μm)	E	Wavelength (μm)	E	Wavelength (μm)	E
26.05	0.169673	26.55	0.049128	27.05	-0.001291
26.06	0.167242	26.56	0.046849	27.06	-0.000595
26.07	0.164811	26.57	0.044570	27.07	0.000102
26.08	0.162379	26.58	0.042291	27.08	0.000798
26.09	0.159948	26.59	0.040012	27.09	0.001494
26.10	0.157517	26.60	0.037732	27.10	0.002190
26.11	0.155086	26.61	0.035453	27.11	0.002887
26.12	0.152655	26.62	0.033174	27.12	0.003583
26.13	0.150223	26.63	0.030895	27.13	0.004279
26.14	0.147792	26.64	0.028616	27.14	0.004975
26.15	0.145361	26.65	0.026337	27.15	0.005672
26.16	0.142930	26.66	0.024058	27.16	0.006368
26.17	0.140499	26.67	0.021779	27.17	0.007064
26.18	0.138067	26.68	0.019500	27.18	0.007760
26.19	0.135619	26.69	0.017221	27.19	0.008456
26.20	0.133168	26.70	0.014942	27.20	0.009153
26.21	0.130717	26.71	0.012663	27.21	0.009849
26.22	0.128266	26.72	0.010384	27.22	0.010545
26.23	0.125815	26.73	0.009652	27.23	0.011241
26.24	0.123364	26.74	0.009115	27.24	0.011938
26.25	0.120913	26.75	0.008579	27.25	0.012634
26.26	0.118461	26.76	0.008042	27.26	0.013330
26.27	0.116011	26.77	0.007505	27.27	0.014026
26.28	0.113559	26.78	0.006969	27.28	0.014723
26.29	0.111108	26.79	0.006432	27.29	0.014813
26.30	0.108657	26.80	0.005895	27.30	0.014552
26.31	0.106206	26.81	0.005359	27.31	0.014291
26.32	0.103755	26.82	0.004822	27.32	0.014030
26.33	0.101304	26.83	0.004286	27.33	0.013769
26.34	0.098853	26.84	0.003749	27.34	0.013509
26.35	0.096402	26.85	0.003212	27.35	0.013248
26.36	0.093951	26.86	0.002676	27.36	0.012987
26.37	0.091500	26.87	0.002139	27.37	0.012726
26.38	0.089049	26.88	0.001602	27.38	0.012465
26.39	0.086598	26.89	0.001066	27.39	0.012204
26.40	0.084147	26.90	0.000529	27.40	0.011943
26.41	0.081696	26.91	-0.000008	27.41	0.011682
26.42	0.079245	26.92	-0.000544	27.42	0.011421
26.43	0.076794	26.93	-0.001081	27.43	0.011161
26.44	0.074343	26.94	-0.001618	27.44	0.010900
26.45	0.071918	26.95	-0.002154	27.45	0.010639
26.46	0.069639	26.96	-0.002691	27.46	0.010378
26.47	0.067360	26.97	-0.003228	27.47	0.010117
26.48	0.065081	26.98	-0.003764	27.48	0.009856
26.49	0.062802	26.99	-0.004301	27.49	0.009595
26.50	0.060523	27.00	-0.004772	27.50	0.009334
26.51	0.058244	27.01	-0.004076	27.51	0.009073
26.52	0.055965	27.02	-0.003380	27.52	0.008813
26.53	0.053686	27.03	-0.002683	27.53	0.008552
26.54	0.051407	27.04	-0.001987	27.54	0.008291

Table A-6 (continued)

Wavelength (μm)	E
27.55	0.008030
27.56	0.007769
27.57	0.007508
27.58	0.007071
27.59	0.006520
27.60	0.005969
27.61	0.005418
27.62	0.004868
27.63	0.004317
27.64	0.003766
27.65	0.003215
27.66	0.002664
27.67	0.002113
27.68	0.001563
27.69	0.001012
27.70	0.000461
27.71	-0.000090
27.72	-0.000641
27.73	-0.001192
27.74	-0.001742
27.75	-0.002293
27.76	-0.002844
27.77	-0.003395
27.78	-0.003946
27.79	-0.004497
27.80	-0.005047
27.81	-0.005598
27.82	-0.006149
27.83	-0.006700
27.84	-0.007251
27.85	-0.007802
27.86	-0.008352
27.87	-0.008903
27.88	-0.008784
27.89	-0.008636
27.90	-0.008488
27.91	-0.008340
27.92	-0.008191
27.93	-0.008043
27.94	-0.007895
27.95	-0.007747
27.96	-0.007599
27.97	-0.007451
27.98	-0.007302
27.99	-0.007154
28.00	0.000000

Reference:
"*SPIRIT III Integrated Ground and On-Orbit Calibration Report in Support of CONVERT 5.2*" (SDL/97-056) March 1998 , Space Dynamics Laboratory, Logan, UT.

APPENDIX B
SPIRIT III EFFECTIVE WAVELENGTH TABLES

The SPIRIT III RSRs shown in Appendix A can be used to derive effective wavelengths and effective bandpasses for each band as a function of source spectral shape. As an example, we model the source as a blackbody and use blackbody temperature as the main parameter. The effective wavelength and bandpass are defined as the equivalent square band with the same integrated power over a given source spectrum:

$$\lambda_e = \frac{\int_0^\infty R(\lambda)\, S(\lambda)\, \lambda \, d\lambda}{\int_0^\infty R(\lambda)\, S(\lambda)\, d\lambda} \tag{B.1}$$

$$d\lambda_e = \frac{\int_0^\infty R(\lambda)\, S(\lambda)\, d\lambda}{\max[R(\lambda)\, S(\lambda)]} \tag{B.2}$$

where $R(\lambda)$ is the relative spectral response
$S(\lambda)$ is the source spectrum

Figures B-1 and B-2 illustrate the relative weighting of the six SPIRIT III bands for source blackbody temperatures of 250K and 6000K, respectively. These two sample temperatures were chosen to be representative of typical hardbody targets and of typical stars. Table B-1 gives the effective wavelengths and bandpasses for the six SPIRIT III bands for source blackbody temperatures from 100 K to 10,000 K. The source temperatures for the table were incremented by 0.02 dex, providing 100 values on a logarithmic scale between 100 K and 10,000 K. Notice that the peak of the blackbody curve at a given temperature relative to the nominal RSR bandpass weights the effective wavelength toward the blackbody peak wavelength.

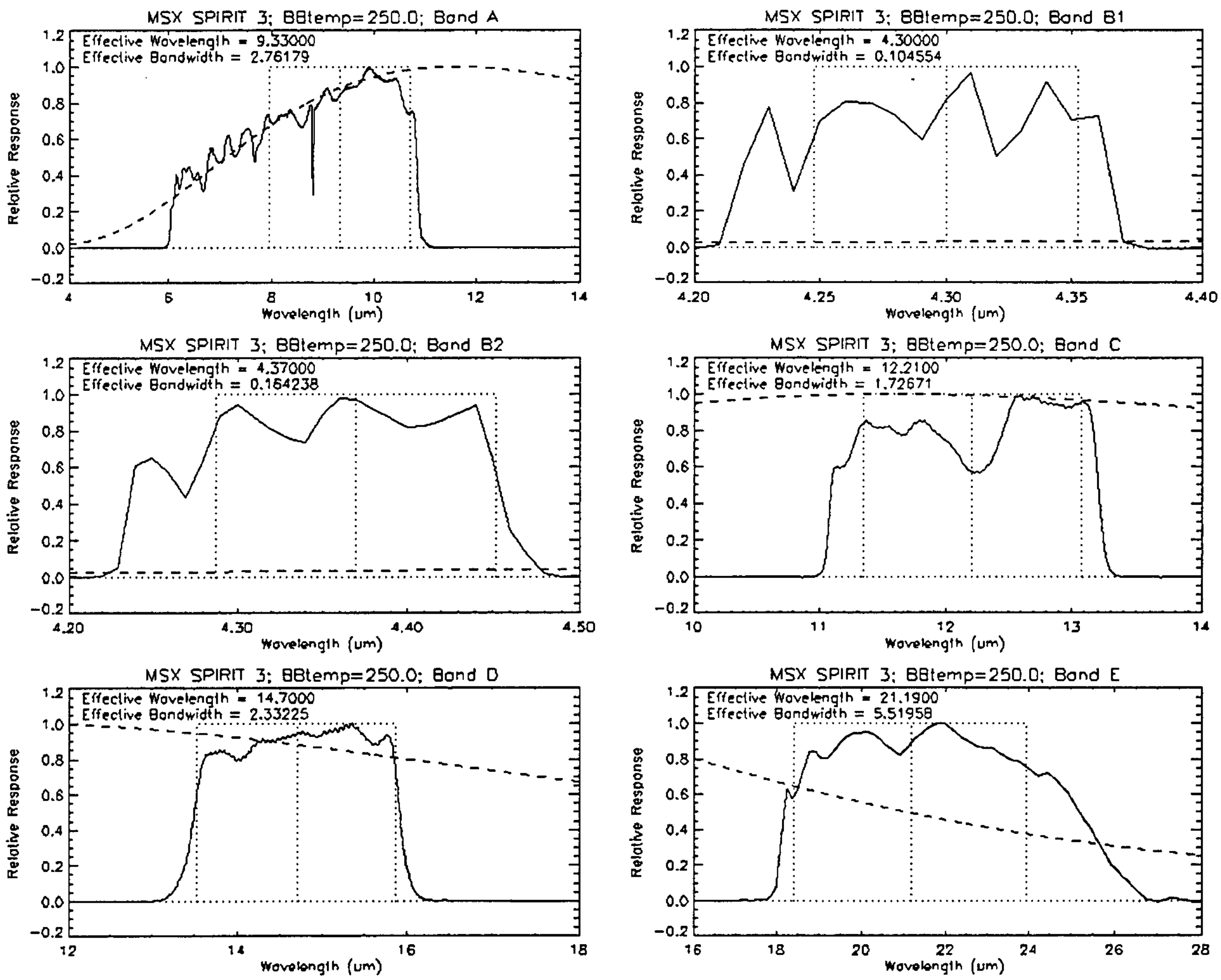

Figure B-1. Effective Response for 250K

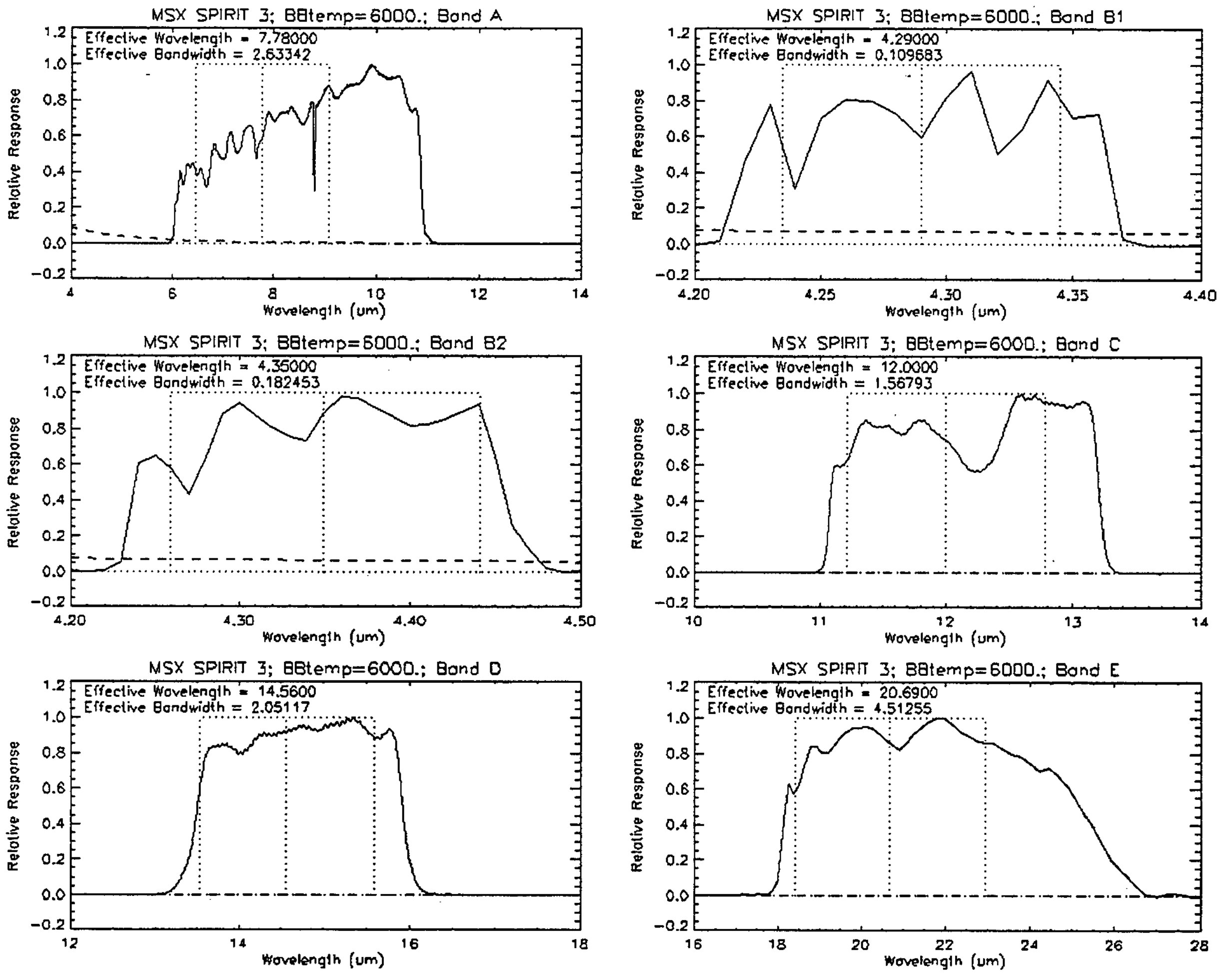

Figure B-2. Effective Response for 6000K

Table B-1. Effective Bandpasses as Function of Source Temperature

Blackbody Temp.	Effective Wavelength (λ_e) / Effective Bandwidth ($d\lambda_e$) by SPIRIT III Band						
		A	**B1**	**B2**	**C**	**D**	**E**
100.000	λ_e	10.180	4.310	4.390	12.560	14.980	22.150
	$d\lambda_e$	1.272	0.087	0.119	1.189	1.779	5.987
104.713	λ_e	10.150	4.310	4.380	12.540	14.960	22.080
	$d\lambda_e$	1.336	0.088	0.122	1.223	1.825	5.992
109.648	λ_e	10.120	4.310	4.380	12.520	14.940	22.010
	$d\lambda_e$	1.404	0.089	0.124	1.258	1.871	6.001
114.815	λ_e	10.090	4.310	4.380	12.510	14.920	21.940
	$d\lambda_e$	1.455	0.090	0.127	1.293	1.916	6.014
120.226	λ_e	10.050	4.310	4.380	12.490	14.900	21.880
	$d\lambda_e$	1.509	0.091	0.129	1.328	1.961	6.031
125.893	λ_e	10.020	4.310	4.380	12.470	14.880	21.820
	$d\lambda_e$	1.565	0.092	0.132	1.363	2.000	6.049

131.826	λ_e $d\lambda_e$	9.980 1.623	4.310 0.093	4.380 0.134	12.450 1.397	14.870 2.026	21.770 6.071
138.038	λ_e $d\lambda_e$	9.950 1.684	4.310 0.094	4.380 0.137	12.440 1.432	14.850 2.052	21.710 6.089
144.544	λ_e $d\lambda_e$	9.910 1.749	4.310 0.095	4.380 0.139	12.420 1.466	14.840 2.077	21.660 6.104
151.356	λ_e $d\lambda_e$	9.870 1.818	4.300 0.096	4.370 0.142	12.400 1.499	14.820 2.101	21.610 6.119
158.489	λ_e $d\lambda_e$	9.830 1.891	4.300 0.097	4.370 0.144	12.380 1.533	14.810 2.125	21.560 6.130
165.959	λ_e $d\lambda_e$	9.790 1.969	4.300 0.098	4.370 0.146	12.360 1.566	14.800 2.149	21.520 6.057
173.780	λ_e $d\lambda_e$	9.740 2.050	4.300 0.099	4.370 0.148	12.340 1.598	14.780 2.172	21.470 5.984
181.970	λ_e $d\lambda_e$	9.690 2.136	4.300 0.100	4.370 0.151	12.330 1.629	14.770 2.194	21.430 5.907
190.546	λ_e $d\lambda_e$	9.640 2.226	4.300 0.100	4.370 0.153	12.310 1.646	14.760 2.216	21.390 5.836
199.526	λ_e $d\lambda_e$	9.590 2.321	4.300 0.101	4.370 0.155	12.290 1.661	14.750 2.237	21.350 5.771
208.930	λ_e $d\lambda_e$	9.540 2.419	4.300 0.102	4.370 0.157	12.270 1.675	14.740 2.258	21.320 5.712
218.776	λ_e $d\lambda_e$	9.490 2.521	4.300 0.103	4.370 0.159	12.260 1.689	14.730 2.278	21.280 5.656
229.087	λ_e $d\lambda_e$	9.440 2.616	4.300 0.103	4.370 0.161	12.240 1.702	14.720 2.297	21.250 5.606
239.883	λ_e $d\lambda_e$	9.380 2.691	4.300 0.104	4.370 0.163	12.220 1.715	14.710 2.316	21.220 5.559
251.189	λ_e $d\lambda_e$	9.320 2.770	4.300 0.105	4.370 0.164	12.210 1.728	14.700 2.334	21.190 5.515
263.027	λ_e $d\lambda_e$	9.270 2.851	4.300 0.105	4.360 0.166	12.200 1.740	14.690 2.343	21.160 5.475
275.423	λ_e $d\lambda_e$	9.210 2.934	4.300 0.105	4.360 0.168	12.180 1.753	14.690 2.345	21.130 5.438
288.403	λ_e $d\lambda_e$	9.150 3.020	4.300 0.106	4.360 0.170	12.170 1.764	14.680 2.341	21.110 5.404
301.995	λ_e $d\lambda_e$	9.100 3.109	4.300 0.106	4.360 0.171	12.160 1.776	14.670 2.334	21.080 5.362
316.228	λ_e $d\lambda_e$	9.040 3.200	4.300 0.106	4.360 0.173	12.150 1.787	14.660 2.327	21.060 5.307
331.131	λ_e $d\lambda_e$	8.990 3.293	4.300 0.106	4.360 0.174	12.140 1.797	14.660 2.320	21.040 5.256

346.737	λ_e	8.940	4.300	4.360	12.130	14.650	21.020
	$d\lambda_e$	3.388	0.106	0.176	1.807	2.314	5.209
363.078	λ_e	8.880	4.300	4.360	12.120	14.650	21.000
	$d\lambda_e$	3.485	0.106	0.177	1.815	2.308	5.165
380.189	λ_e	8.830	4.300	4.360	12.110	14.640	20.980
	$d\lambda_e$	3.584	0.107	0.179	1.799	2.296	5.124
398.107	λ_e	8.760	4.300	4.360	12.110	14.640	20.970
	$d\lambda_e$	3.683	0.107	0.180	1.784	2.282	5.086
416.869	λ_e	8.710	4.300	4.360	12.100	14.630	20.950
	$d\lambda_e$	3.783	0.107	0.181	1.770	2.269	5.050
436.516	λ_e	8.660	4.300	4.360	12.090	14.630	20.930
	$d\lambda_e$	3.883	0.107	0.183	1.758	2.256	5.017
457.088	λ_e	8.610	4.300	4.360	12.090	14.620	20.920
	$d\lambda_e$	3.941	0.107	0.183	1.745	2.243	4.986
478.630	λ_e	8.560	4.300	4.360	12.080	14.620	20.910
	$d\lambda_e$	3.975	0.107	0.183	1.734	2.231	4.957
501.187	λ_e	8.510	4.300	4.360	12.080	14.620	20.890
	$d\lambda_e$	3.945	0.107	0.183	1.724	2.220	4.930
524.807	λ_e	8.460	4.300	4.360	12.070	14.610	20.880
	$d\lambda_e$	3.920	0.107	0.183	1.714	2.210	4.905
549.541	λ_e	8.420	4.300	4.360	12.070	14.610	20.870
	$d\lambda_e$	3.898	0.108	0.183	1.705	2.200	4.881
575.440	λ_e	8.390	4.300	4.360	12.060	14.610	20.860
	$d\lambda_e$	3.879	0.108	0.183	1.696	2.191	4.859
602.560	λ_e	8.350	4.300	4.360	12.060	14.600	20.850
	$d\lambda_e$	3.828	0.108	0.183	1.688	2.183	4.839
630.957	λ_e	8.320	4.300	4.360	12.050	14.600	20.840
	$d\lambda_e$	3.764	0.108	0.183	1.681	2.175	4.819
660.693	λ_e	8.290	4.300	4.360	12.050	14.600	20.830
	$d\lambda_e$	3.706	0.108	0.183	1.674	2.168	4.801
691.831	λ_e	8.260	4.300	4.360	12.050	14.600	20.820
	$d\lambda_e$	3.654	0.108	0.183	1.667	2.161	4.784
724.436	λ_e	8.230	4.300	4.360	12.040	14.590	20.820
	$d\lambda_e$	3.606	0.108	0.183	1.661	2.154	4.768
758.578	λ_e	8.200	4.300	4.360	12.040	14.590	20.810
	$d\lambda_e$	3.562	0.108	0.183	1.655	2.148	4.753
794.328	λ_e	8.170	4.300	4.360	12.040	14.590	20.800
	$d\lambda_e$	3.522	0.108	0.183	1.650	2.142	4.738
831.764	λ_e	8.150	4.300	4.360	12.040	14.590	20.790
	$d\lambda_e$	3.486	0.108	0.184	1.645	2.137	4.725
870.964	λ_e	8.130	4.300	4.360	12.030	14.590	20.790
	$d\lambda_e$	3.452	0.109	0.184	1.640	2.132	4.712

912.011	λ_e	8.110	4.300	4.350	12.030	14.580	20.780
	$d\lambda_e$	3.421	0.109	0.184	1.636	2.127	4.701
954.993	λ_e	8.090	4.300	4.350	12.030	14.580	20.780
	$d\lambda_e$	3.393	0.109	0.184	1.631	2.122	4.689
1000.00	λ_e	8.070	4.300	4.350	12.030	14.580	20.770
	$d\lambda_e$	3.367	0.109	0.184	1.627	2.118	4.679
1047.13	λ_e	8.050	4.290	4.350	12.030	14.580	20.770
	$d\lambda_e$	3.342	0.109	0.184	1.624	2.114	4.669
1096.48	λ_e	8.030	4.290	4.350	12.020	14.580	20.760
	$d\lambda_e$	3.309	0.109	0.184	1.620	2.110	4.659
1148.15	λ_e	8.010	4.290	4.350	12.020	14.580	20.760
	$d\lambda_e$	3.260	0.109	0.184	1.617	2.107	4.651
1202.26	λ_e	8.000	4.290	4.350	12.020	14.570	20.750
	$d\lambda_e$	3.214	0.109	0.184	1.614	2.104	4.642
1258.93	λ_e	7.980	4.290	4.350	12.020	14.570	20.750
	$d\lambda_e$	3.172	0.109	0.184	1.611	2.100	4.634
1318.26	λ_e	7.970	4.290	4.350	12.020	14.570	20.750
	$d\lambda_e$	3.133	0.109	0.184	1.608	2.097	4.627
1380.38	λ_e	7.960	4.290	4.350	12.020	14.570	20.740
	$d\lambda_e$	3.097	0.109	0.184	1.606	2.095	4.620
1445.44	λ_e	7.950	4.290	4.350	12.010	14.570	20.740
	$d\lambda_e$	3.063	0.109	0.184	1.603	2.092	4.613
1513.56	λ_e	7.940	4.290	4.350	12.010	14.570	20.740
	$d\lambda_e$	3.032	0.109	0.184	1.601	2.089	4.606
1584.89	λ_e	7.930	4.290	4.350	12.010	14.570	20.730
	$d\lambda_e$	3.002	0.109	0.184	1.599	2.087	4.600
1659.59	λ_e	7.920	4.290	4.350	12.010	14.570	20.730
	$d\lambda_e$	2.975	0.109	0.184	1.597	2.085	4.595
1737.80	λ_e	7.910	4.290	4.350	12.010	14.570	20.730
	$d\lambda_e$	2.950	0.109	0.184	1.595	2.083	4.589
1819.70	λ_e	7.900	4.290	4.350	12.010	14.570	20.720
	$d\lambda_e$	2.926	0.109	0.184	1.593	2.081	4.584
1905.46	λ_e	7.890	4.290	4.350	12.010	14.570	20.720
	$d\lambda_e$	2.904	0.109	0.184	1.591	2.079	4.579
1995.26	λ_e	7.880	4.290	4.350	12.010	14.560	20.720
	$d\lambda_e$	2.884	0.109	0.184	1.590	2.077	4.575
2089.30	λ_e	7.880	4.290	4.350	12.010	14.560	20.720
	$d\lambda_e$	2.864	0.109	0.184	1.588	2.075	4.570
2187.76	λ_e	7.870	4.290	4.350	12.010	14.560	20.720
	$d\lambda_e$	2.846	0.109	0.184	1.587	2.073	4.566
2290.87	λ_e	7.860	4.290	4.350	12.000	14.560	20.710
	$d\lambda_e$	2.829	0.109	0.184	1.585	2.072	4.562

2398.83	λ_e	7.860	4.290	4.350	12.000	14.560	20.710
	$d\lambda_e$	2.813	0.109	0.184	1.584	2.070	4.558
2511.89	λ_e	7.850	4.290	4.350	12.000	14.560	20.710
	$d\lambda_e$	2.798	0.109	0.183	1.583	2.069	4.555
2630.27	λ_e	7.850	4.290	4.350	12.000	14.560	20.710
	$d\lambda_e$	2.784	0.109	0.183	1.581	2.067	4.552
2754.23	λ_e	7.840	4.290	4.350	12.000	14.560	20.710
	$d\lambda_e$	2.771	0.109	0.183	1.580	2.066	4.548
2884.03	λ_e	7.840	4.290	4.350	12.000	14.560	20.710
	$d\lambda_e$	2.759	0.110	0.183	1.579	2.065	4.545
3019.95	λ_e	7.830	4.290	4.350	12.000	14.560	20.700
	$d\lambda_e$	2.747	0.110	0.183	1.578	2.063	4.542
3162.28	λ_e	7.830	4.290	4.350	12.000	14.560	20.700
	$d\lambda_e$	2.736	0.110	0.183	1.577	2.062	4.540
3311.31	λ_e	7.820	4.290	4.350	12.000	14.560	20.700
	$d\lambda_e$	2.726	0.110	0.183	1.576	2.061	4.537
3467.37	λ_e	7.820	4.290	4.350	12.000	14.560	20.700
	$d\lambda_e$	2.716	0.110	0.183	1.575	2.060	4.534
3630.78	λ_e	7.810	4.290	4.350	12.000	14.560	20.700
	$d\lambda_e$	2.707	0.110	0.183	1.575	2.059	4.532
3801.89	λ_e	7.810	4.290	4.350	12.000	14.560	20.700
	$d\lambda_e$	2.698	0.110	0.183	1.574	2.058	4.530
3981.07	λ_e	7.810	4.290	4.350	12.000	14.560	20.700
	$d\lambda_e$	2.690	0.110	0.183	1.573	2.057	4.528
4168.69	λ_e	7.800	4.290	4.350	12.000	14.560	20.700
	$d\lambda_e$	2.682	0.110	0.183	1.572	2.057	4.526
4365.16	λ_e	7.800	4.290	4.350	12.000	14.560	20.690
	$d\lambda_e$	2.675	0.110	0.183	1.572	2.056	4.524
4570.88	λ_e	7.800	4.290	4.350	12.000	14.560	20.690
	$d\lambda_e$	2.668	0.110	0.183	1.571	2.055	4.522
4786.30	λ_e	7.790	4.290	4.350	12.000	14.560	20.690
	$d\lambda_e$	2.661	0.110	0.183	1.570	2.054	4.520
5011.87	λ_e	7.790	4.290	4.350	12.000	14.560	20.690
	$d\lambda_e$	2.655	0.110	0.183	1.570	2.054	4.518
5248.07	λ_e	7.790	4.290	4.350	12.000	14.560	20.690
	$d\lambda_e$	2.649	0.110	0.183	1.569	2.053	4.517
5495.41	λ_e	7.780	4.290	4.350	12.000	14.560	20.690
	$d\lambda_e$	2.643	0.110	0.183	1.569	2.052	4.515
5754.40	λ_e	7.780	4.290	4.350	12.000	14.560	20.690
	$d\lambda_e$	2.638	0.110	0.182	1.568	2.052	4.514
6025.60	λ_e	7.780	4.290	4.350	12.000	14.560	20.690
	$d\lambda_e$	2.633	0.110	0.182	1.568	2.051	4.512

6309.57	λ_e $d\lambda_e$	7.780 2.628	4.290 0.110	4.350 0.182	12.000 1.567	14.560 2.051	20.690 4.511
6606.94	λ_e $d\lambda_e$	7.770 2.624	4.290 0.110	4.350 0.182	12.000 1.567	14.560 2.050	20.690 4.510
6918.31	λ_e $d\lambda_e$	7.770 2.619	4.290 0.110	4.350 0.182	12.000 1.567	14.560 2.050	20.690 4.509
7244.36	λ_e $d\lambda_e$	7.770 2.615	4.290 0.110	4.350 0.182	12.000 1.566	14.550 2.049	20.690 4.508
7585.78	λ_e $d\lambda_e$	7.770 2.612	4.290 0.110	4.350 0.182	11.990 1.566	14.550 2.049	20.690 4.506
7943.28	λ_e $d\lambda_e$	7.770 2.608	4.290 0.110	4.350 0.182	11.990 1.566	14.550 2.048	20.680 4.505
8317.64	λ_e $d\lambda_e$	7.760 2.604	4.290 0.110	4.350 0.182	11.990 1.565	14.550 2.048	20.680 4.504
8709.64	λ_e $d\lambda_e$	7.760 2.601	4.290 0.110	4.350 0.182	11.990 1.565	14.550 2.047	20.680 4.503
9120.11	λ_e $d\lambda_e$	7.760 2.598	4.290 0.110	4.350 0.182	11.990 1.565	14.550 2.047	20.680 4.503
9549.93	λ_e $d\lambda_e$	7.760 2.595	4.290 0.110	4.350 0.182	11.990 1.564	14.550 2.047	20.680 4.502
10000.0	λ_e $d\lambda_e$	7.760 2.592	4.290 0.110	4.350 0.182	11.990 1.564	14.550 2.046	20.680 4.501

APPENDIX C
SPIRIT III PHOTOMETRIC CONVERSIONS

The SPIRIT III RSRs shown in Appendix A can be used to derive inband photometric conversion factors to other IR experiments of interest as a function of source spectral shape. As an example, we again model the source as a blackbody, and use blackbody temperature as a typical source model parameter. The conversion factor is defined as the ratio of the **inband flux** of a given source in the "other" system to the reported SPIRIT III **inband flux**:

$$k_{m\rightarrow x} = \frac{\int_0^\infty R_x(\lambda)S(\lambda)\,d\lambda}{\int_0^\infty R_m(\lambda)S(\lambda)\,d\lambda} \qquad \text{(C.1)}$$

where $R(\lambda)$ is the relative spectral response
$S(\lambda)$ is the source spectrum (typically a black body)
The index *m* stands for a band in MSX/SPIRIT III.
And *x* is a band in the other system, such as DIRBE, IRAS, or AFGL 4-Color.

The inband flux in another photometric system is then calculated from the reported SPIRIT III inband flux:

$$F_x = k_{m\rightarrow x}\, F_m \qquad \text{(C.2)}$$

The usage is to multiply the SPIRIT III-reported inband flux by the conversion factor to get equivalent inband flux for the other instrument. Note that the units can be either inband radiance or inband irradiance. In the following sections, we describe the derivation of inband photometric transformation factors to convert MSX inband flux to appropriate bands in the IRAS, DIRBE, and the AFGL 4-Color survey experiments for a variety of source blackbody temperatures.

C.1 SPIRIT III To IRAS

The RSRs for the four IRAS bands, as provided in the IRAS Explanatory Supplement [ref] are shown in Figure C-1. The overlapping bands of interest are the IRAS 12 and 25 micron bands. Table C-1 provides tabulated RSRs for the IRAS 12 and 25 micron bands. Table C-2 provides conversion factors for the four overlapping MSX bands to the 12 and 25 micron IRAS bands.

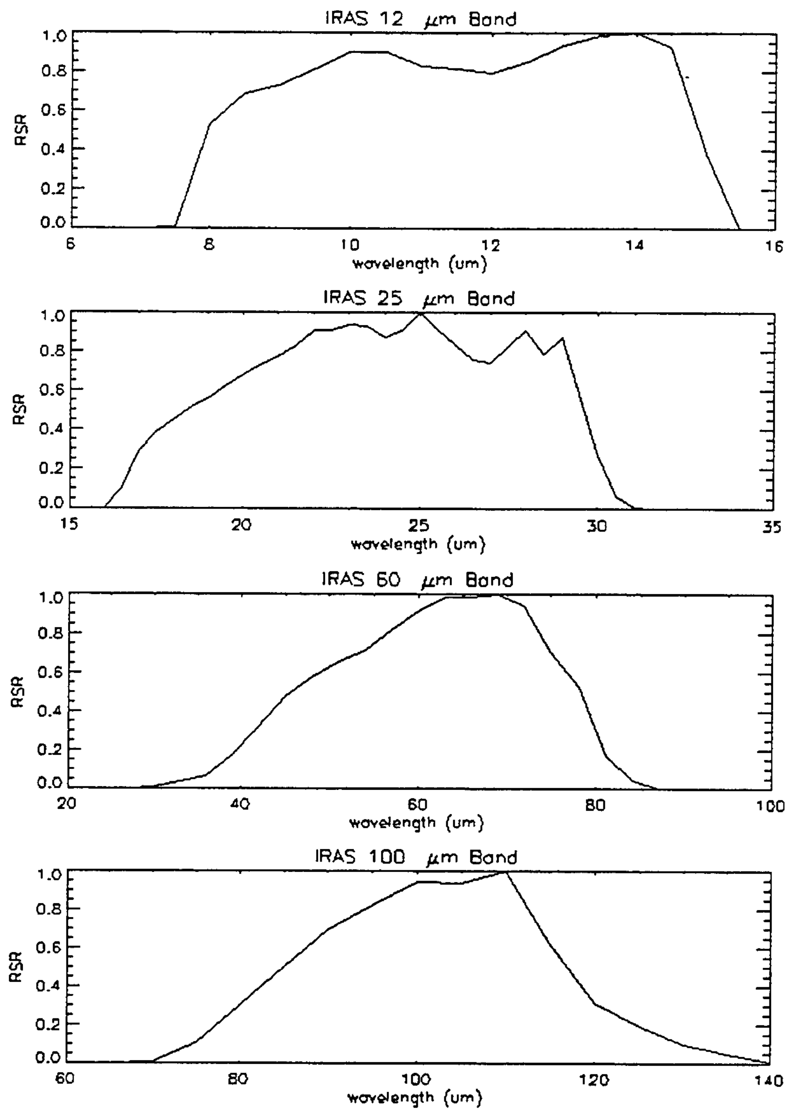

Figure C-1 IRAS Wavebands

Table C-1. IRAS RSRs

Band	λ (μm)	Total RSR
12 μm Band	7.0	0.000
	7.5	0.008
	8.0	0.535
	8.5	0.689
	9.0	0.735
	9.5	0.815
	10.0	0.900
	10.5	0.904
	11.0	0.834
	11.5	0.816
	12.0	0.793
	12.5	0.854
	13.0	0.938

	13.5	0.991
	14.0	1.000
	14.5	0.934
	15.0	0.388
	15.5	0.000
25 µm Band	16.0	0.007
	16.5	0.101
	17.0	0.288
	17.5	0.388
	18.0	0.452
	18.5	0.521
	19.0	0.562
	19.5	0.626
	20.0	0.683
	20.5	0.729
	21.0	0.778
	21.5	0.832
	22.0	0.912
	22.5	0.914
	23.0	0.938
	23.5	0.933
	24.0	0.875
	24.5	0.910
	25.0	1.000
	25.5	0.911
	26.0	0.840
	26.5	0.763
	27.0	0.749
	27.5	0.829
	28.0	0.914
	28.5	0.790
	29.0	0.877
	29.5	0.558
	30.0	0.274
	30.5	0.069
	31.0	0.012
	31.5	0.000

Table C-2 Conversion Factors: SPIRIT III to IRAS

Blackbody Temperature (K)	$k_{m_A \to l_{12\mu m}}$	$k_{m_C \to l_{12\mu m}}$	$k_{m_D \to l_{12\mu m}}$	$k_{m_E \to l_{25\mu m}}$
100.00000	16.96809	3.54922	0.94848	1.75356
104.71285	14.46175	3.43565	1.00196	1.71056
109.64781	12.42179	3.33894	1.05870	1.67177
114.81535	10.74919	3.25744	1.11896	1.63675
120.22643	9.36811	3.18974	1.18296	1.60513
125.89252	8.22001	3.13461	1.25096	1.57657
131.82564	7.25940	3.09101	1.32319	1.55076
138.03847	6.45065	3.05798	1.39990	1.52743
144.54401	5.76568	3.03473	1.48131	1.50634
151.35616	5.18221	3.02051	1.56762	1.48727
158.48933	4.68246	3.01468	1.65903	1.47002

165.95869	4.25215	3.01664	1.75570	1.45441
173.78009	3.87975	3.02585	1.85775	1.44028
181.97008	3.55589	3.04179	1.96528	1.42749
190.54607	3.27293	3.06398	2.07833	1.41591
199.52621	3.02461	3.09199	2.19692	1.40542
208.92958	2.80576	3.12535	2.32098	1.39591
218.77612	2.61210	3.16366	2.45042	1.38728
229.08684	2.44006	3.20650	2.58509	1.37946
239.88336	2.28669	3.25345	2.72477	1.37235
251.18871	2.14948	3.30413	2.86921	1.36590
263.02686	2.02633	3.35812	3.01807	1.36003
275.42291	1.91548	3.41503	3.17101	1.35469
288.40317	1.81540	3.47450	3.32761	1.34983
301.99518	1.72480	3.53612	3.48742	1.34539
316.22775	1.64260	3.59954	3.64997	1.34135
331.13110	1.56784	3.66439	3.81475	1.33765
346.73682	1.49971	3.73033	3.98124	1.33428
363.07800	1.43749	3.79703	4.14891	1.33119
380.18933	1.38058	3.86416	4.31724	1.32835
398.10709	1.32843	3.93144	4.48570	1.32575
416.86926	1.28057	3.99860	4.65377	1.32337
436.51569	1.23660	4.06536	4.82098	1.32117
457.08829	1.19613	4.13150	4.98685	1.31915
478.63016	1.15885	4.19682	5.15094	1.31729
501.18729	1.12447	4.26111	5.31285	1.31557
524.80750	1.09273	4.32422	5.47221	1.31398
549.54089	1.06339	4.38601	5.62870	1.31251
575.43994	1.03626	4.44634	5.78203	1.31115
602.55957	1.01115	4.50513	5.93193	1.30990
630.95728	0.98787	4.56229	6.07821	1.30873
660.69336	0.96630	4.61776	6.22067	1.30764
691.83081	0.94628	4.67149	6.35918	1.30663
724.43616	0.92768	4.72344	6.49362	1.30569
758.57776	0.91041	4.77360	6.62392	1.30481
794.32843	0.89434	4.82198	6.75004	1.30399
831.76392	0.87939	4.86856	6.87194	1.30323
870.96368	0.86547	4.91336	6.98962	1.30252
912.01093	0.85249	4.95641	7.10311	1.30185
954.99261	0.84040	4.99774	7.21244	1.30122
1000.00000	0.82911	5.03737	7.31766	1.30064
1047.12854	0.81857	5.07535	7.41885	1.30009
1096.47815	0.80872	5.11173	7.51608	1.29958
1148.15344	0.79952	5.14654	7.60943	1.29909
1202.26428	0.79091	5.17984	7.69901	1.29864
1258.92517	0.78285	5.21167	7.78492	1.29821
1318.25635	0.77530	5.24209	7.86725	1.29781
1380.38379	0.76823	5.27115	7.94614	1.29743
1445.43921	0.76160	5.29889	8.02166	1.29707
1513.56067	0.75537	5.32538	8.09396	1.29673
1584.89331	0.74953	5.35066	8.16313	1.29641
1659.58704	0.74404	5.37477	8.22931	1.29612
1737.80090	0.73888	5.39778	8.29258	1.29583
1819.70081	0.73403	5.41971	8.35308	1.29556

1905.46057	0.72946	5.44064	8.41089	1.29531
1995.26208	0.72517	5.46059	8.46614	1.29507
2089.29688	0.72112	5.47960	8.51892	1.29484
2187.76245	0.71731	5.49774	8.56935	1.29463
2290.86841	0.71371	5.51502	8.61752	1.29443
2398.83350	0.71032	5.53149	8.66351	1.29423
2511.88696	0.70712	5.54719	8.70743	1.29405
2630.26855	0.70410	5.56216	8.74936	1.29388
2754.22900	0.70124	5.57642	8.78940	1.29372
2884.03174	0.69854	5.59002	8.82761	1.29356
3019.95190	0.69599	5.60297	8.86410	1.29341
3162.27759	0.69358	5.61532	8.89892	1.29327
3311.31104	0.69130	5.62709	8.93217	1.29314
3467.36816	0.68914	5.63831	8.96389	1.29301
3630.78003	0.68710	5.64901	8.99418	1.29289
3801.89331	0.68516	5.65920	9.02308	1.29278
3981.07080	0.68333	5.66892	9.05066	1.29267
4168.69287	0.68159	5.67818	9.07699	1.29257
4365.15674	0.67994	5.68702	9.10211	1.29247
4570.88037	0.67838	5.69544	9.12609	1.29238
4786.29883	0.67690	5.70346	9.14898	1.29229
5011.87305	0.67549	5.71111	9.17082	1.29221
5248.07471	0.67416	5.71841	9.19166	1.29213
5495.40869	0.67289	5.72537	9.21156	1.29205
5754.39941	0.67169	5.73200	9.23054	1.29198
6025.59570	0.67055	5.73833	9.24866	1.29191
6309.57275	0.66946	5.74436	9.26596	1.29184
6606.93701	0.66843	5.75011	9.28246	1.29178
6918.31201	0.66745	5.75561	9.29822	1.29172
7244.36182	0.66652	5.76084	9.31325	1.29166
7585.77783	0.66563	5.76583	9.32760	1.29161
7943.28418	0.66479	5.77060	9.34130	1.29156
8317.63965	0.66398	5.77514	9.35437	1.29151
8709.63672	0.66322	5.77947	9.36684	1.29146
9120.10938	0.66250	5.78360	9.37876	1.29142
9549.92676	0.66181	5.78755	9.39013	1.29137
10000.00000	0.66115	5.79131	9.40098	1.29134

C.2 SPIRIT III To DIRBE

The RSRs for the ten COBE/DIRBE bands, as provided in the DIRBE Explanatory Supplement [http://www.gsfc.nasa.gov/astro/cobe/dirbe_exsup.html], are shown in Figure C-2. The overlapping bands of interest are DIRBE Bands 3-6.

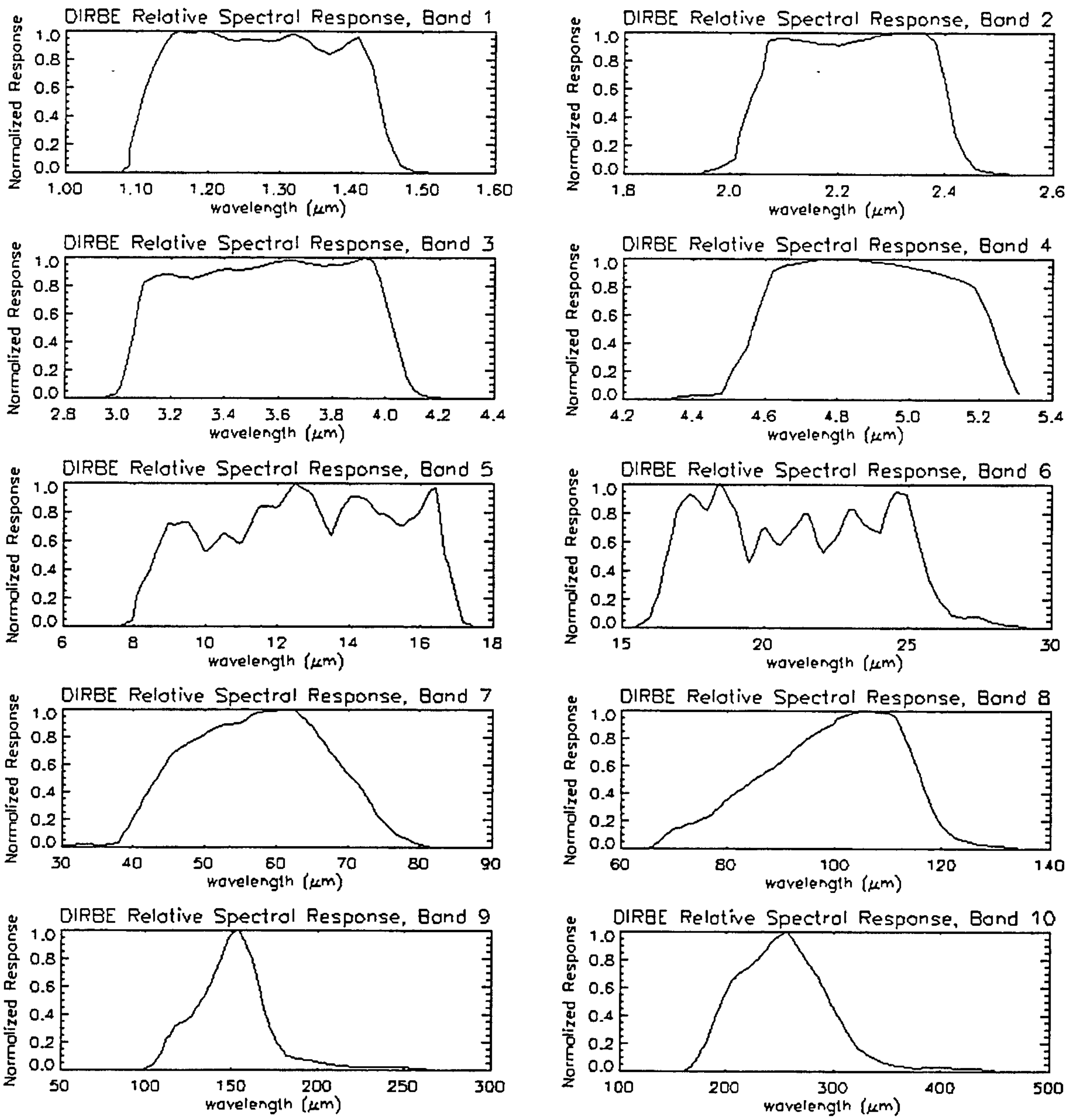

Figure C-2 DIRBE Wavebands

Table C-3 DIRBE RSRs

Wavelength (μm)	Band 3	Band 4	Band 5	Band 6
2.94	0.00	0.00	0.00	0.00
2.96	0.01	0.00	0.00	0.00
2.99	0.02	0.00	0.00	0.00
3.01	0.07	0.00	0.00	0.00
3.03	0.21	0.00	0.00	0.00
3.06	0.47	0.00	0.00	0.00
3.08	0.71	0.00	0.00	0.00
3.10	0.82	0.00	0.00	0.00
3.13	0.85	0.00	0.00	0.00

3.15	0.87	0.00	0.00	0.00
3.18	0.88	0.00	0.00	0.00
3.20	0.88	0.00	0.00	0.00
3.23	0.86	0.00	0.00	0.00
3.25	0.86	0.00	0.00	0.00
3.28	0.85	0.00	0.00	0.00
3.30	0.86	0.00	0.00	0.00
3.33	0.88	0.00	0.00	0.00
3.36	0.90	0.00	0.00	0.00
3.38	0.91	0.00	0.00	0.00
3.41	0.92	0.00	0.00	0.00
3.44	0.91	0.00	0.00	0.00
3.46	0.91	0.00	0.00	0.00
3.49	0.92	0.00	0.00	0.00
3.52	0.93	0.00	0.00	0.00
3.54	0.94	0.00	0.00	0.00
3.57	0.96	0.00	0.00	0.00
3.60	0.97	0.00	0.00	0.00
3.63	0.98	0.00	0.00	0.00
3.66	0.98	0.00	0.00	0.00
3.68	0.97	0.00	0.00	0.00
3.71	0.96	0.00	0.00	0.00
3.74	0.95	0.00	0.00	0.00
3.77	0.94	0.00	0.00	0.00
3.80	0.95	0.00	0.00	0.00
3.83	0.95	0.00	0.00	0.00
3.86	0.96	0.00	0.00	0.00
3.89	0.98	0.00	0.00	0.00
3.92	1.00	0.00	0.00	0.00
3.95	0.98	0.00	0.00	0.00
3.98	0.85	0.00	0.00	0.00
4.01	0.63	0.00	0.00	0.00
4.05	0.35	0.00	0.00	0.00
4.08	0.14	0.00	0.00	0.00
4.11	0.06	0.00	0.00	0.00
4.14	0.02	0.00	0.00	0.00
4.17	0.01	0.00	0.00	0.00
4.21	0.01	0.00	0.00	0.00
4.24	0.00	0.00	0.00	0.00
4.27	0.00	0.00	0.00	0.00
4.30	0.00	0.00	0.00	0.00
4.34	0.00	0.01	0.00	0.00
4.37	0.00	0.02	0.00	0.00
4.41	0.00	0.03	0.00	0.00
4.44	0.00	0.03	0.00	0.00
4.48	0.00	0.04	0.00	0.00
4.51	0.00	0.20	0.00	0.00
4.55	0.00	0.37	0.00	0.00
4.58	0.00	0.61	0.00	0.00
4.62	0.00	0.91	0.00	0.00
4.65	0.00	0.95	0.00	0.00
4.69	0.00	0.97	0.00	0.00
4.73	0.00	0.99	0.00	0.00

4.76	0.00	1.00	0.00	0.00
4.80	0.00	1.00	0.00	0.00
4.84	0.00	1.00	0.00	0.00
4.88	0.00	0.99	0.00	0.00
4.91	0.00	0.98	0.00	0.00
4.95	0.00	0.97	0.00	0.00
4.99	0.00	0.95	0.00	0.00
5.03	0.00	0.93	0.00	0.00
5.07	0.00	0.91	0.00	0.00
5.11	0.00	0.88	0.00	0.00
5.15	0.00	0.85	0.00	0.00
5.19	0.00	0.80	0.00	0.00
5.23	0.00	0.57	0.00	0.00
5.27	0.00	0.27	0.00	0.00
5.31	0.00	0.04	0.00	0.00
5.35	0.00	0.00	0.00	0.00
7.60	0.00	0.00	0.00	0.00
7.66	0.00	0.00	0.01	0.00
7.72	0.00	0.00	0.01	0.00
7.78	0.00	0.00	0.02	0.00
7.84	0.00	0.00	0.03	0.00
7.90	0.00	0.00	0.03	0.00
7.96	0.00	0.00	0.04	0.00
8.02	0.00	0.00	0.15	0.00
8.09	0.00	0.00	0.21	0.00
8.15	0.00	0.00	0.25	0.00
8.21	0.00	0.00	0.29	0.00
8.28	0.00	0.00	0.32	0.00
8.34	0.00	0.00	0.35	0.00
8.41	0.00	0.00	0.38	0.00
8.47	0.00	0.00	0.41	0.00
8.54	0.00	0.00	0.45	0.00
8.60	0.00	0.00	0.50	0.00
8.67	0.00	0.00	0.54	0.00
8.74	0.00	0.00	0.59	0.00
8.81	0.00	0.00	0.63	0.00
8.88	0.00	0.00	0.68	0.00
8.95	0.00	0.00	0.71	0.00
9.02	0.00	0.00	0.72	0.00
9.09	0.00	0.00	0.71	0.00
9.16	0.00	0.00	0.71	0.00
9.23	0.00	0.00	0.72	0.00
9.30	0.00	0.00	0.72	0.00
9.37	0.00	0.00	0.73	0.00
9.45	0.00	0.00	0.73	0.00
9.52	0.00	0.00	0.73	0.00
9.59	0.00	0.00	0.70	0.00
9.67	0.00	0.00	0.67	0.00
9.75	0.00	0.00	0.65	0.00
9.82	0.00	0.00	0.61	0.00
9.90	0.00	0.00	0.57	0.00
9.98	0.00	0.00	0.53	0.00
10.05	0.00	0.00	0.53	0.00

10.13	0.00	0.00	0.55	0.00
10.21	0.00	0.00	0.57	0.00
10.29	0.00	0.00	0.59	0.00
10.37	0.00	0.00	0.61	0.00
10.45	0.00	0.00	0.64	0.00
10.53	0.00	0.00	0.65	0.00
10.62	0.00	0.00	0.64	0.00
10.70	0.00	0.00	0.62	0.00
10.78	0.00	0.00	0.61	0.00
10.87	0.00	0.00	0.59	0.00
10.95	0.00	0.00	0.58	0.00
11.04	0.00	0.00	0.59	0.00
11.12	0.00	0.00	0.64	0.00
11.21	0.00	0.00	0.69	0.00
11.30	0.00	0.00	0.74	0.00
11.39	0.00	0.00	0.78	0.00
11.47	0.00	0.00	0.83	0.00
11.56	0.00	0.00	0.84	0.00
11.65	0.00	0.00	0.84	0.00
11.75	0.00	0.00	0.84	0.00
11.84	0.00	0.00	0.84	0.00
11.93	0.00	0.00	0.83	0.00
12.02	0.00	0.00	0.84	0.00
12.12	0.00	0.00	0.87	0.00
12.21	0.00	0.00	0.90	0.00
12.31	0.00	0.00	0.94	0.00
12.40	0.00	0.00	0.97	0.00
12.50	0.00	0.00	1.00	0.00
12.60	0.00	0.00	0.98	0.00
12.70	0.00	0.00	0.97	0.00
12.80	0.00	0.00	0.95	0.00
12.90	0.00	0.00	0.94	0.00
13.00	0.00	0.00	0.91	0.00
13.10	0.00	0.00	0.86	0.00
13.20	0.00	0.00	0.80	0.00
13.30	0.00	0.00	0.75	0.00
13.41	0.00	0.00	0.69	0.00
13.51	0.00	0.00	0.64	0.00
13.62	0.00	0.00	0.72	0.00
13.72	0.00	0.00	0.78	0.00
13.83	0.00	0.00	0.83	0.00
13.94	0.00	0.00	0.87	0.00
14.05	0.00	0.00	0.91	0.00
14.16	0.00	0.00	0.91	0.00
14.27	0.00	0.00	0.91	0.00
14.38	0.00	0.00	0.90	0.00
14.49	0.00	0.00	0.89	0.00
14.61	0.00	0.00	0.86	0.00
14.72	0.00	0.00	0.82	0.00
14.83	0.00	0.00	0.79	0.00
14.95	0.00	0.00	0.79	0.00
15.07	0.00	0.00	0.78	0.00
15.18	0.00	0.00	0.76	0.00

15.30	0.00	0.00	0.73	0.00
15.42	0.00	0.00	0.71	0.00
15.54	0.00	0.00	0.71	0.01
15.66	0.00	0.00	0.74	0.02
15.79	0.00	0.00	0.76	0.04
15.91	0.00	0.00	0.79	0.05
16.03	0.00	0.00	0.83	0.08
16.16	0.00	0.00	0.90	0.16
16.29	0.00	0.00	0.95	0.21
16.41	0.00	0.00	0.97	0.34
16.54	0.00	0.00	0.77	0.45
16.67	0.00	0.00	0.52	0.55
16.80	0.00	0.00	0.41	0.67
16.93	0.00	0.00	0.29	0.79
17.06	0.00	0.00	0.16	0.85
17.20	0.00	0.00	0.03	0.89
17.33	0.00	0.00	0.02	0.92
17.47	0.00	0.00	0.01	0.93
17.60	0.00	0.00	0.00	0.91
17.74	0.00	0.00	0.00	0.88
17.88	0.00	0.00	0.00	0.84
18.02	0.00	0.00	0.00	0.82
18.16	0.00	0.00	0.00	0.88
18.30	0.00	0.00	0.00	0.94
18.44	0.00	0.00	0.00	1.00
18.59	0.00	0.00	0.00	0.99
18.73	0.00	0.00	0.00	0.93
18.88	0.00	0.00	0.00	0.87
19.03	0.00	0.00	0.00	0.81
19.18	0.00	0.00	0.00	0.68
19.33	0.00	0.00	0.00	0.56
19.48	0.00	0.00	0.00	0.46
19.63	0.00	0.00	0.00	0.51
19.78	0.00	0.00	0.00	0.60
19.94	0.00	0.00	0.00	0.69
20.09	0.00	0.00	0.00	0.70
20.25	0.00	0.00	0.00	0.64
20.41	0.00	0.00	0.00	0.60
20.57	0.00	0.00	0.00	0.58
20.73	0.00	0.00	0.00	0.63
20.89	0.00	0.00	0.00	0.66
21.05	0.00	0.00	0.00	0.70
21.22	0.00	0.00	0.00	0.75
21.38	0.00	0.00	0.00	0.80
21.55	0.00	0.00	0.00	0.80
21.72	0.00	0.00	0.00	0.69
21.89	0.00	0.00	0.00	0.59
22.06	0.00	0.00	0.00	0.53
22.23	0.00	0.00	0.00	0.57
22.41	0.00	0.00	0.00	0.61
22.58	0.00	0.00	0.00	0.66
22.76	0.00	0.00	0.00	0.74
22.93	0.00	0.00	0.00	0.83

23.11	0.00	0.00	0.00	0.83
23.29	0.00	0.00	0.00	0.78
23.48	0.00	0.00	0.00	0.73
23.66	0.00	0.00	0.00	0.70
23.84	0.00	0.00	0.00	0.68
24.03	0.00	0.00	0.00	0.67
24.22	0.00	0.00	0.00	0.79
24.41	0.00	0.00	0.00	0.90
24.60	0.00	0.00	0.00	0.95
24.79	0.00	0.00	0.00	0.94
24.98	0.00	0.00	0.00	0.93
25.18	0.00	0.00	0.00	0.77
25.38	0.00	0.00	0.00	0.62
25.57	0.00	0.00	0.00	0.48
25.77	0.00	0.00	0.00	0.35
25.98	0.00	0.00	0.00	0.24
26.18	0.00	0.00	0.00	0.18
26.38	0.00	0.00	0.00	0.14
26.59	0.00	0.00	0.00	0.09
26.80	0.00	0.00	0.00	0.08
27.01	0.00	0.00	0.00	0.07
27.22	0.00	0.00	0.00	0.08
27.43	0.00	0.00	0.00	0.08
27.64	0.00	0.00	0.00	0.07
27.86	0.00	0.00	0.00	0.05
28.08	0.00	0.00	0.00	0.04
28.30	0.00	0.00	0.00	0.03
28.52	0.00	0.00	0.00	0.02
28.74	0.00	0.00	0.00	0.02
28.97	0.00	0.00	0.00	0.01
29.19	0.00	0.00	0.00	0.01
29.42	0.00	0.00	0.00	0.00

Table C-4 Inband Conversion Factors: SPIRIT III to DIRBE

Blackbody Temperature (K)	$k_{m_A \to D_5}$	$k_{m_{B1} \to D_4}$	$k_{m_{B2} \to D_4}$	$k_{m_C \to D_5}$	$k_{m_D \to D_5}$	$k_{m_E \to D_6}$
100.00000	32.20831	282.13565	108.12963	6.73702	1.80037	1.08917
104.71285	26.25741	225.87505	88.68529	6.23792	1.81920	1.09539
109.64781	21.61920	182.92891	73.48759	5.81117	1.84260	1.10226
114.81535	17.96944	149.77699	61.49035	5.44546	1.87056	1.10970
120.22643	15.07114	123.91182	51.92960	5.13156	1.90311	1.11763
125.89252	12.74945	103.52688	44.24175	4.86186	1.94027	1.12600
131.82564	10.87411	87.30568	38.00680	4.63012	1.98205	1.13471
138.03847	9.34722	74.27937	32.90886	4.43113	2.02850	1.14371
144.54401	8.09458	63.72793	28.70840	4.26054	2.07965	1.15293
151.35616	7.05946	55.11032	25.22184	4.11470	2.13549	1.16232
158.48933	6.19814	48.01700	22.30765	3.99052	2.19605	1.17181
165.95869	5.47670	42.13487	19.85568	3.88538	2.26131	1.18135
173.78009	4.86858	37.22271	17.77962	3.79705	2.33124	1.19090
181.97008	4.35291	33.09306	16.01131	3.72358	2.40578	1.20042
190.54607	3.91311	29.59924	14.49658	3.66329	2.48485	1.20985
199.52621	3.53597	26.62555	13.19209	3.61473	2.56834	1.21917
208.92958	3.21087	24.08007	12.06291	3.57660	2.65609	1.22834

218.77612	2.92924	21.88933	11.08072	3.54777	2.74793	1.23734
229.08684	2.68412	19.99419	10.22247	3.52722	2.84366	1.24615
239.88336	2.46984	18.34679	9.46924	3.51403	2.94301	1.25473
251.18871	2.28171	16.90813	8.80545	3.50739	3.04572	1.26309
263.02686	2.11590	15.64623	8.21818	3.50654	3.15147	1.27119
275.42291	1.96919	14.53480	7.69666	3.51081	3.25994	1.27904
288.40317	1.83894	13.55203	7.23192	3.51957	3.37078	1.28662
301.99518	1.72292	12.67980	6.81638	3.53225	3.48360	1.29394
316.22775	1.61923	11.90294	6.44366	3.54832	3.59804	1.30098
331.13110	1.52631	11.20871	6.10836	3.56732	3.71369	1.30775
346.73682	1.44280	10.58639	5.80586	3.58879	3.83017	1.31425
363.07800	1.36757	10.02687	5.53224	3.61232	3.94709	1.32049
380.18933	1.29962	9.52240	5.28413	3.63756	4.06407	1.32645
398.10709	1.23811	9.06639	5.05861	3.66415	4.18073	1.33216
416.86926	1.18232	8.65317	4.85320	3.69181	4.29672	1.33762
436.51569	1.13162	8.27786	4.66571	3.72025	4.41172	1.34283
457.08829	1.08545	7.93626	4.49427	3.74922	4.52542	1.34781
478.63016	1.04334	7.62474	4.33722	3.77850	4.63752	1.35255
501.18729	1.00487	7.34012	4.19312	3.80791	4.74778	1.35707
524.80750	0.96967	7.07963	4.06073	3.83726	4.85597	1.36138
549.54089	0.93742	6.84087	3.93891	3.86641	4.96189	1.36548
575.43994	0.90782	6.62171	3.82669	3.89523	5.06536	1.36938
602.55957	0.88063	6.42028	3.72319	3.92361	5.16624	1.37310
630.95728	0.85561	6.23492	3.62765	3.95146	5.26441	1.37663
660.69336	0.83257	6.06416	3.53936	3.97870	5.35978	1.37999
691.83081	0.81133	5.90670	3.45771	4.00528	5.45229	1.38319
724.43616	0.79172	5.76136	3.38214	4.03113	5.54186	1.38622
758.57776	0.77359	5.62710	3.31216	4.05623	5.62848	1.38911
794.32843	0.75683	5.50297	3.24729	4.08055	5.71215	1.39186
831.76392	0.74130	5.38813	3.18715	4.10406	5.79286	1.39447
870.96368	0.72691	5.28182	3.13134	4.12677	5.87064	1.39695
912.01093	0.71356	5.18332	3.07953	4.14866	5.94550	1.39931
954.99261	0.70116	5.09201	3.03141	4.16973	6.01751	1.40154
1000.00000	0.68964	5.00732	2.98669	4.18999	6.08669	1.40367
1047.12854	0.67892	4.92871	2.94511	4.20946	6.15314	1.40570
1096.47815	0.66893	4.85572	2.90644	4.22814	6.21688	1.40762
1148.15344	0.65963	4.78789	2.87045	4.24605	6.27801	1.40945
1202.26428	0.65095	4.72484	2.83694	4.26322	6.33660	1.41119
1258.92517	0.64285	4.66618	2.80573	4.27965	6.39272	1.41285
1318.25635	0.63528	4.61159	2.77664	4.29538	6.44644	1.41442
1380.38379	0.62821	4.56075	2.74951	4.31042	6.49786	1.41591
1445.43921	0.62159	4.51338	2.72421	4.32480	6.54704	1.41734
1513.56067	0.61540	4.46921	2.70059	4.33855	6.59409	1.41869
1584.89331	0.60959	4.42801	2.67854	4.35167	6.63905	1.41998
1659.58704	0.60415	4.38956	2.65793	4.36421	6.68204	1.42120
1737.80090	0.59904	4.35365	2.63867	4.37618	6.72311	1.42237
1819.70081	0.59424	4.32009	2.62066	4.38760	6.76234	1.42347
1905.46057	0.58974	4.28872	2.60380	4.39850	6.79981	1.42453
1995.26208	0.58550	4.25937	2.58802	4.40890	6.83560	1.42553
2089.29688	0.58152	4.23189	2.57323	4.41882	6.86977	1.42649
2187.76245	0.57777	4.20615	2.55937	4.42829	6.90240	1.42740
2290.86841	0.57424	4.18204	2.54637	4.43731	6.93355	1.42827
2398.83350	0.57092	4.15942	2.53418	4.44592	6.96327	1.42909

2511.88696	0.56778	4.13821	2.52273	4.45413	6.99164	1.42988
2630.26855	0.56482	4.11829	2.51198	4.46195	7.01873	1.43062
2754.22900	0.56203	4.09959	2.50187	4.46942	7.04457	1.43134
2884.03174	0.55940	4.08201	2.49237	4.47653	7.06923	1.43201
3019.95190	0.55691	4.06548	2.48343	4.48331	7.09276	1.43266
3162.27759	0.55456	4.04993	2.47502	4.48978	7.11521	1.43327
3311.31104	0.55234	4.03530	2.46710	4.49595	7.13664	1.43386
3467.36816	0.55024	4.02152	2.45963	4.50183	7.15709	1.43442
3630.78003	0.54825	4.00854	2.45260	4.50743	7.17659	1.43495
3801.89331	0.54636	3.99629	2.44596	4.51277	7.19521	1.43547
3981.07080	0.54458	3.98475	2.43971	4.51787	7.21296	1.43595
4168.69287	0.54289	3.97386	2.43380	4.52273	7.22991	1.43641
4365.15674	0.54129	3.96358	2.42822	4.52736	7.24607	1.43685
4570.88037	0.53978	3.95388	2.42295	4.53178	7.26151	1.43727
4786.29883	0.53834	3.94471	2.41798	4.53599	7.27622	1.43767
5011.87305	0.53698	3.93604	2.41327	4.54001	7.29027	1.43805
5248.07471	0.53568	3.92785	2.40882	4.54384	7.30367	1.43841
5495.40869	0.53446	3.92010	2.40461	4.54749	7.31646	1.43876
5754.39941	0.53329	3.91276	2.40062	4.55097	7.32867	1.43909
6025.59570	0.53219	3.90582	2.39685	4.55429	7.34031	1.43940
6309.57275	0.53114	3.89925	2.39327	4.55746	7.35143	1.43970
6606.93701	0.53014	3.89302	2.38989	4.56048	7.36203	1.43999
6918.31201	0.52919	3.88713	2.38668	4.56337	7.37215	1.44026
7244.36182	0.52829	3.88153	2.38364	4.56612	7.38180	1.44053
7585.77783	0.52743	3.87623	2.38075	4.56874	7.39103	1.44078
7943.28418	0.52662	3.87120	2.37801	4.57124	7.39982	1.44101
8317.63965	0.52584	3.86644	2.37542	4.57363	7.40821	1.44124
8709.63672	0.52511	3.86191	2.37295	4.57591	7.41622	1.44145
9120.10938	0.52441	3.85761	2.37062	4.57808	7.42387	1.44166
9549.92676	0.52374	3.85354	2.36839	4.58016	7.43117	1.44186
10000.00000	0.52311	3.84967	2.36628	4.58213	7.43813	1.44205

C.3 SPIRIT III To AFGL Survey

The detailed spectral shapes of the AFGL 4-Color survey bands are not available. Table C-5 shows the AFGL 4 Color survey effective wavelengths and bandwidths for an equal intensity ("flat") source (ref: Price & Walker 1976).

Figure C-5. AFGL 4 Color Survey Effective Flat Source Squarebands

Band	λ_{eff} (μm)	$d\lambda_{eff}$ (μm)
1	4.2	1.5
2	11.0	5.1
3	19.8	5.6
4	27.4	3.4

Table C-6. Inband Conversion Factors: SPIRIT III to AFGL 4-Color

Blackbody Temperature (K)	$k_{m_A \to A_{11\mu m}}$	$k_{m_{B1} \to A_{4\mu m}}$	$k_{m_{B2} \to A_{4\mu m}}$	$k_{m_C \to A_{11\mu m}}$	$k_{m_D \to A_{11\mu m}}$	$k_{m_E \to A_{20\mu m}}$
100.00000	8.71734	71.70344	27.48063	1.82341	0.48728	0.75607
104.71285	7.77539	62.05991	24.36657	1.84718	0.53870	0.77812

109.64781	6.97280	54.18996	21.76960	1.87427	0.59429	0.79967
114.81535	6.28509	47.72063	19.59151	1.90464	0.65426	0.82068
120.22643	5.69261	42.36662	17.75522	1.93827	0.71884	0.84114
125.89252	5.17947	37.90768	16.19968	1.97513	0.78823	0.86104
131.82564	4.73276	34.17260	14.87636	2.01518	0.86265	0.88035
138.03847	4.34195	31.02717	13.74633	2.05834	0.94228	0.89907
144.54401	3.99840	28.36561	12.77825	2.10454	1.02726	0.91720
151.35616	3.69501	26.10370	11.94664	2.15368	1.11774	0.93471
158.48933	3.42589	24.17411	11.23077	2.20567	1.21382	0.95161
165.95869	3.18615	22.52265	10.61360	2.26038	1.31555	0.96790
173.78009	2.97173	21.10541	10.08111	2.31768	1.42296	0.98357
181.97008	2.77921	19.88654	9.62164	2.37740	1.53602	0.99864
190.54607	2.60573	18.83669	9.22549	2.43938	1.65466	1.01310
199.52621	2.44889	17.93165	8.88455	2.50344	1.77874	1.02696
208.92958	2.30663	17.15129	8.59194	2.56937	1.90809	1.04024
218.77612	2.17724	16.47884	8.34185	2.63699	2.04248	1.05293
229.08684	2.05924	15.90024	8.12934	2.70605	2.18163	1.06506
239.88336	1.95136	15.40360	7.95019	2.77635	2.32520	1.07663
251.18871	1.85252	14.97885	7.80072	2.84765	2.47282	1.08767
263.02686	1.76179	14.61737	7.67777	2.91970	2.62405	1.09818
275.42291	1.67835	14.31179	7.57857	2.99227	2.77846	1.10819
288.40317	1.60151	14.05574	7.50071	3.06513	2.93555	1.11770
301.99518	1.53063	13.84367	7.44205	3.13804	3.09482	1.12675
316.22775	1.46519	13.67077	7.40068	3.21076	3.25575	1.13534
331.13110	1.40470	13.53282	7.37491	3.28309	3.41780	1.14349
346.73682	1.34874	13.42606	7.36321	3.35481	3.58045	1.15123
363.07800	1.29692	13.34721	7.36421	3.42571	3.74319	1.15857
380.18933	1.24891	13.29330	7.37666	3.49563	3.90549	1.16553
398.10709	1.20440	13.26171	7.39940	3.56438	4.06688	1.17213
416.86926	1.16311	13.25005	7.43140	3.63182	4.22690	1.17838
436.51569	1.12480	13.25618	7.47168	3.69781	4.38512	1.18429
457.08829	1.08922	13.27815	7.51935	3.76224	4.54114	1.18990
478.63016	1.05618	13.31417	7.57357	3.82501	4.69460	1.19521
501.18729	1.02549	13.36264	7.63356	3.88602	4.84518	1.20024
524.80750	0.99695	13.42205	7.69860	3.94523	4.99261	1.20500
549.54089	0.97043	13.49100	7.76799	4.00257	5.13663	1.20951
575.43994	0.94576	13.56826	7.84109	4.05802	5.27705	1.21378
602.55957	0.92281	13.65263	7.91731	4.11154	5.41369	1.21782
630.95728	0.90145	13.74300	7.99606	4.16314	5.54642	1.22165
660.69336	0.88156	13.83838	8.07680	4.21280	5.67514	1.22527
691.83081	0.86304	13.93783	8.15904	4.26056	5.79979	1.22871
724.43616	0.84578	14.04046	8.24230	4.30641	5.92030	1.23196
758.57776	0.82970	14.14548	8.32614	4.35040	6.03668	1.23504
794.32843	0.81470	14.25213	8.41015	4.39257	6.14894	1.23796
831.76392	0.80071	14.35976	8.49397	4.43295	6.25708	1.24072
870.96368	0.78765	14.46774	8.57723	4.47159	6.36116	1.24335
912.01093	0.77546	14.57551	8.65964	4.50853	6.46124	1.24583
954.99261	0.76407	14.68258	8.74092	4.54383	6.55739	1.24819
1000.00000	0.75342	14.78849	8.82081	4.57755	6.64969	1.25042
1047.12854	0.74347	14.89286	8.89911	4.60973	6.73822	1.25254
1096.47815	0.73416	14.99536	8.97562	4.64044	6.82311	1.25455
1148.15344	0.72545	15.09569	9.05021	4.66972	6.90443	1.25646
1202.26428	0.71728	15.19359	9.12272	4.69765	6.98231	1.25827

1258.92517	0.70964	15.28889	9.19306	4.72427	7.05685	1.25999
1318.25635	0.70247	15.38142	9.26116	4.74962	7.12816	1.26162
1380.38379	0.69574	15.47105	9.32695	4.77379	7.19637	1.26317
1445.43921	0.68943	15.55771	9.39041	4.79680	7.26156	1.26464
1513.56067	0.68351	15.64131	9.45151	4.81872	7.32390	1.26604
1584.89331	0.67794	15.72183	9.51026	4.83959	7.38344	1.26737
1659.58704	0.67271	15.79927	9.56665	4.85947	7.44033	1.26863
1737.80090	0.66778	15.87364	9.62074	4.87839	7.49466	1.26983
1819.70081	0.66315	15.94496	9.67254	4.89640	7.54653	1.27097
1905.46057	0.65880	16.01330	9.72212	4.91356	7.59606	1.27206
1995.26208	0.65469	16.07868	9.76950	4.92988	7.64333	1.27309
2089.29688	0.65082	16.14120	9.81477	4.94543	7.68847	1.27407
2187.76245	0.64718	16.20093	9.85797	4.96023	7.73154	1.27500
2290.86841	0.64374	16.25794	9.89919	4.97432	7.77264	1.27589
2398.83350	0.64049	16.31232	9.93847	4.98773	7.81186	1.27673
2511.88696	0.63743	16.36419	9.97591	5.00050	7.84928	1.27754
2630.26855	0.63454	16.41359	10.01156	5.01266	7.88499	1.27830
2754.22900	0.63180	16.46066	10.04550	5.02423	7.91905	1.27903
2884.03174	0.62922	16.50546	10.07780	5.03526	7.95155	1.27972
3019.95190	0.62678	16.54812	10.10854	5.04575	7.98256	1.28038
3162.27759	0.62447	16.58872	10.13779	5.05575	8.01213	1.28101
3311.31104	0.62228	16.62734	10.16560	5.06527	8.04035	1.28161
3467.36816	0.62021	16.66407	10.19204	5.07433	8.06727	1.28217
3630.78003	0.61825	16.69900	10.21718	5.08298	8.09296	1.28272
3801.89331	0.61639	16.73224	10.24110	5.09120	8.11745	1.28324
3981.07080	0.61464	16.76383	10.26383	5.09904	8.14082	1.28373
4168.69287	0.61297	16.79387	10.28544	5.10650	8.16312	1.28419
4365.15674	0.61139	16.82242	10.30597	5.11362	8.18439	1.28464
4570.88037	0.60989	16.84959	10.32550	5.12040	8.20468	1.28507
4786.29883	0.60847	16.87539	10.34406	5.12686	8.22405	1.28548
5011.87305	0.60712	16.89995	10.36172	5.13302	8.24251	1.28586
5248.07471	0.60584	16.92330	10.37850	5.13888	8.26013	1.28623
5495.40869	0.60462	16.94549	10.39445	5.14447	8.27695	1.28658
5754.39941	0.60346	16.96659	10.40961	5.14980	8.29300	1.28692
6025.59570	0.60237	16.98665	10.42403	5.15488	8.30830	1.28724
6309.57275	0.60133	17.00574	10.43775	5.15973	8.32291	1.28754
6606.93701	0.60033	17.02391	10.45080	5.16434	8.33684	1.28784
6918.31201	0.59939	17.04117	10.46321	5.16875	8.35016	1.28811
7244.36182	0.59850	17.05762	10.47502	5.17295	8.36284	1.28838
7585.77783	0.59765	17.07324	10.48625	5.17695	8.37495	1.28863
7943.28418	0.59684	17.08812	10.49693	5.18077	8.38650	1.28887
8317.63965	0.59607	17.10226	10.50710	5.18441	8.39753	1.28910
8709.63672	0.59534	17.11574	10.51678	5.18788	8.40805	1.28932
9120.10938	0.59464	17.12856	10.52599	5.19119	8.41810	1.28953
9549.92676	0.59398	17.14076	10.53475	5.19435	8.42769	1.28972
10000.00000	0.59334	17.15237	10.54310	5.19737	8.43683	1.28992

APPENDIX D
SPIRIT III COLOR CORRECTION FACTORS

The flux densities (Jy) quoted in the MSX Point Source Catalog Version 1.2 are isophotal flux densities at the isophotal wavelengths shown in Table 1 of the Explanatory Guide. The zero magnitude flux has been defined by integrating the α Lyr (Vega) Kurucz model spectrum of Cohen et al. (1999, see reference in main text) over with the MSX Relative Spectral Response to find the in-band irradiance. The in-band irradiance is divided by the isophotal bandwidth to determine a flux density (the isophotal F_λ or F_ν). This value is the zero magnitude flux for the band.

The output of the MSX point source extractor is in-band irradiance, or

$$E = \int_0^\infty R_\nu \, S_\nu \, d\nu$$

where R_ν is the Relative Spectral Response of the band, and S_ν is the source function of the object. We convert the in-band irradiance (W cm^{-2}) to flux density (in W cm^{-2} Hz^{-1}) at the isophotal wavelength by the equation:

$$F_\nu(iso) = \frac{\int_0^\infty R_\nu \, S_\nu \, d\nu}{\Delta\nu_{iso}}$$

where $\Delta\nu_{iso}$ is the isophotal bandwidth (expressed in frequency).

For other source functions, one must **DIVIDE** by the numbers in the table to recover the true flux density at the isophotal wavelength for each band.

Table D-1: MSX Color Correction Factors for Blackbodies
(DIVIDE by these numbers)

TEMP.	B1	B2	A	C	D	E
10000	1.001	1.004	1.040	1.006	1.005	1.015
5000	1.001	1.003	1.033	1.006	1.004	1.014
4000	1.001	1.003	1.030	1.005	1.004	1.014
3000	1.001	1.003	1.024	1.005	1.004	1.013
2000	1.001	1.002	1.013	1.004	1.003	1.012
1000	1.000	1.000	0.982	1.002	1.002	1.008
900	1.000	1.000	0.976	1.001	1.001	1.007
800	1.000	0.999	0.969	1.001	1.001	1.005
700	1.000	0.999	0.962	1.000	1.001	1.004
600	0.999	0.998	0.955	0.999	0.999	1.002
500	0.999	0.997	0.952	0.997	0.998	0.999
400	0.999	0.997	0.960	0.996	0.997	0.995
300	1.000	0.997	1.013	0.995	0.996	0.989
290	1.000	0.997	1.024	0.995	0.996	0.988
280	1.000	0.997	1.037	0.995	0.996	0.988
270	1.000	0.998	1.052	0.995	0.996	0.987
260	1.001	0.998	1.070	0.996	0.996	0.986
250	1.001	0.998	1.091	0.996	0.996	0.986
240	1.001	0.999	1.116	0.997	0.996	0.985

230	1.002	0.999	1.146	0.997	0.996	0.984
220	1.002	1.000	1.181	0.998	0.996	0.984
210	1.003	1.001	1.224	0.999	0.997	0.983
200	1.004	1.002	1.276	1.001	0.997	0.983
190	1.004	1.003	1.339	1.003	0.998	0.983
180	1.005	1.005	1.418	1.005	0.999	0.983
170	1.007	1.007	1.517	1.008	1.001	0.983
160	1.008	1.010	1.643	1.012	1.002	0.984
150	1.010	1.013	1.807	1.017	1.005	0.986
140	1.013	1.017	2.027	1.023	1.008	0.989
130	1.016	1.023	2.329	1.032	1.013	0.993
120	1.020	1.030	2.761	1.044	1.019	1.000
110	1.026	1.041	3.406	1.059	1.028	1.010
100	1.035	1.055	4.432	1.081	1.040	1.026
95	1.042	1.065	5.186	1.096	1.048	1.037
90	1.051	1.078	6.198	1.113	1.058	1.050
85	1.066	1.096	7.595	1.134	1.069	1.067
80	1.094	1.123	9.589	1.159	1.084	1.089
75	1.157	1.173	12.553	1.192	1.102	1.117
70	1.329	1.285	17.179	1.232	1.125	1.153
65	1.910	1.612	24.838	1.285	1.154	1.202
60	4.387	2.865	38.492	1.355	1.193	1.267
55	18.157	9.250	65.208	1.449	1.245	1.359
50	125.140	54.667	124.153	1.582	1.316	1.493
45	1417.190	549.761	276.612	1.773	1.420	1.700
40	---	---	766.547	2.072	1.576	2.028

Table D-2: MSX Color Correction Factors for Modified Blackbodies

$F_\nu = \nu B_\nu(TEMP)$; $F_\lambda = B_\lambda(TEMP)/\lambda$;

DIVIDE by these numbers

TEMP.	B1	B2	A	C	D	E
10000	1.002	1.006	1.110	1.014	1.011	1.039
5000	1.002	1.005	1.100	1.013	1.010	1.038
4000	1.002	1.005	1.095	1.013	1.010	1.037
3000	1.001	1.004	1.087	1.012	1.010	1.036
2000	1.001	1.004	1.070	1.011	1.009	1.034
1000	1.000	1.002	1.019	1.007	1.007	1.028
900	1.000	1.001	1.009	1.007	1.006	1.027
800	1.000	1.000	0.997	1.006	1.005	1.025
700	1.000	1.000	0.983	1.004	1.004	1.023
600	1.000	0.999	0.966	1.003	1.003	1.019
500	0.999	0.998	0.949	1.001	1.002	1.015
400	0.999	0.997	0.938	0.998	0.999	1.009
300	1.000	0.997	0.958	0.995	0.996	0.999
290	1.000	0.997	0.964	0.994	0.996	0.998
280	1.000	0.997	0.972	0.994	0.996	0.996
270	1.000	0.997	0.982	0.994	0.995	0.995
260	1.000	0.997	0.994	0.994	0.995	0.993
250	1.000	0.997	1.008	0.994	0.995	0.992

240	1.001	0.998	1.026	0.994	0.995	0.990
230	1.001	0.998	1.047	0.994	0.994	0.989
220	1.001	0.999	1.073	0.994	0.994	0.987
210	1.002	1.000	1.105	0.994	0.994	0.985
200	1.003	1.000	1.144	0.995	0.994	0.984
190	1.003	1.002	1.193	0.996	0.994	0.982
180	1.004	1.003	1.254	0.998	0.995	0.980
170	1.005	1.005	1.332	1.000	0.996	0.979
160	1.007	1.007	1.432	1.002	0.997	0.978
150	1.009	1.010	1.563	1.006	0.998	0.977
140	1.011	1.014	1.739	1.011	1.001	0.977
130	1.014	1.020	1.982	1.018	1.004	0.979
120	1.018	1.027	2.330	1.027	1.009	0.981
110	1.024	1.036	2.851	1.041	1.015	0.987
100	1.032	1.050	3.678	1.059	1.025	0.997
95	1.038	1.059	4.286	1.072	1.032	1.004
90	1.046	1.071	5.101	1.087	1.040	1.014
85	1.058	1.087	6.223	1.105	1.050	1.026
80	1.079	1.110	7.824	1.128	1.063	1.042
75	1.125	1.149	10.198	1.157	1.079	1.064
70	1.245	1.233	13.895	1.194	1.099	1.093
65	1.643	1.466	20.002	1.242	1.125	1.132
60	3.321	2.336	30.860	1.306	1.160	1.185
55	12.614	6.719	52.046	1.393	1.207	1.261
50	84.649	37.756	98.644	1.514	1.273	1.373
45	953.175	375.320	218.764	1.693	1.368	1.544
40	---	---	603.370	1.971	1.513	1.824

Table D-3: MSX Color Correction Factors for Modified Blackbodies

$F_\nu = \nu^2 B_\nu(TEMP)$; $F_\lambda = B_\lambda(TEMP)/\lambda^2$;

DIVIDE by these numbers

TEMP.	B1	B2	A	C	D	E
10000	1.002	1.007	1.216	1.024	1.020	1.072
5000	1.002	1.007	1.202	1.023	1.019	1.071
4000	1.002	1.007	1.195	1.023	1.019	1.070
3000	1.002	1.006	1.183	1.022	1.018	1.069
2000	1.002	1.005	1.159	1.020	1.017	1.066
1000	1.001	1.003	1.086	1.015	1.014	1.058
900	1.001	1.002	1.071	1.015	1.013	1.056
800	1.000	1.002	1.052	1.014	1.012	1.054
700	1.000	1.001	1.030	1.012	1.011	1.051
600	1.000	1.000	1.003	1.010	1.010	1.046
500	1.000	0.999	0.972	1.007	1.007	1.041
400	0.999	0.997	0.940	1.002	1.004	1.032
300	0.999	0.996	0.926	0.997	0.999	1.017
290	0.999	0.996	0.929	0.996	0.999	1.016
280	0.999	0.996	0.931	0.995	0.998	1.014
270	1.000	0.997	0.936	0.995	0.998	1.012
260	1.000	0.997	0.942	0.994	0.997	1.010
250	1.000	0.997	0.950	0.994	0.996	1.007

240	1.000	0.997	0.961	0.993	0.996	1.005
230	1.000	0.997	0.975	0.993	0.995	1.002
220	1.001	0.998	0.992	0.992	0.995	1.000
210	1.001	0.998	1.015	0.992	0.994	0.997
200	1.002	0.999	1.043	0.992	0.994	0.994
190	1.002	1.000	1.080	0.992	0.993	0.991
180	1.003	1.001	1.126	0.993	0.993	0.987
170	1.004	1.003	1.185	0.994	0.993	0.984
160	1.006	1.005	1.264	0.995	0.993	0.981
150	1.007	1.008	1.368	0.998	0.994	0.978
140	1.009	1.012	1.508	1.001	0.995	0.975
130	1.012	1.017	1.703	1.006	0.997	0.973
120	1.016	1.023	1.983	1.013	1.000	0.972
110	1.021	1.032	2.403	1.025	1.005	0.973
100	1.029	1.045	3.071	1.040	1.013	0.978
95	1.033	1.053	3.561	1.051	1.018	0.982
90	1.041	1.064	4.218	1.064	1.025	0.987
85	1.051	1.079	5.122	1.080	1.034	0.996
80	1.067	1.099	6.408	1.101	1.044	1.007
75	1.102	1.131	8.313	1.127	1.058	1.023
70	1.186	1.195	11.272	1.160	1.076	1.044
65	1.461	1.364	16.150	1.203	1.099	1.075
60	2.601	1.971	24.798	1.261	1.131	1.118
55	8.877	4.986	41.621	1.341	1.173	1.180
50	57.400	26.210	78.505	1.453	1.233	1.272
45	641.398	256.443	173.251	1.618	1.321	1.415
40	---	---	475.463	1.876	1.454	1.652

Table D-4: MSX Color Correction Factors for Power Law Spectra
of the form
ν^{α} or, equivalently, λ^{β} (where $\beta = -\alpha - 2$)
DIVIDE by these numbers

alpha	A	B1	B2	C	D	E	beta
-4.0	1.199	1.000	0.998	1.018	1.017	1.071	2.0
-3.5	1.147	1.000	0.998	1.013	1.012	1.053	1.5
-3.0	1.103	1.000	0.998	1.009	1.009	1.037	1.0
-2.5	1.067	1.000	0.999	1.006	1.006	1.024	0.5
-2.0	1.038	1.000	0.999	1.003	1.003	1.014	0.0
-1.5	1.016	1.000	1.000	1.001	1.001	1.006	-0.5
-1.0	1.000	1.000	1.000	1.000	1.000	1.000	-1.0
-0.5	0.991	1.000	1.001	0.999	0.999	0.997	-1.5
0.0	0.988	1.000	1.001	1.000	0.999	0.996	-2.0
0.5	0.993	1.001	1.002	1.000	1.000	0.998	-2.5
1.0	1.003	1.001	1.002	1.002	1.001	1.001	-3.0
1.5	1.021	1.001	1.003	1.004	1.003	1.008	-3.5
2.0	1.046	1.001	1.004	1.007	1.005	1.016	-4.0
2.5	1.079	1.002	1.005	1.010	1.008	1.027	-4.5
3.0	1.120	1.002	1.006	1.014	1.011	1.040	-5.0
3.5	1.170	1.002	1.007	1.019	1.015	1.056	-5.5